

**EXPERIMENTAL INVESTIGATION AND
NUMERICAL MODELLING OF HYDROGEN
EXPOSED PIEZOELECTRIC ACTUATORS FOR
FUEL INJECTOR APPLICATIONS**

by

Yadvinder Singh

B.Tech. (Mechanical), Jamia Millia Islamia University, 2007

Thesis Submitted in Partial Fulfillment
of the Requirements for the Degree of
Master of Applied Science

in the
School of Engineering Science
Faculty of Applied Sciences

© Yadvinder Singh 2013

SIMON FRASER UNIVERSITY

Spring 2013

All rights reserved.

However, in accordance with the *Copyright Act of Canada*, this work may be reproduced, without authorization, under the conditions for "Fair Dealing." Therefore, limited reproduction of this work for the purposes of private study, research, criticism, review and news reporting is likely to be in accordance with the law, particularly if cited appropriately.

Approval

Name: Yadvinder Singh
Degree: Master of Applied Science (Engineering Science)
Title of Thesis: *Experimental investigation and numerical modelling of hydrogen exposed piezoelectric actuators for fuel injector applications*

Examining Committee:

Chair: Gary Wang, Professor

Nimal Rajapakse
Senior Supervisor
Professor

Erik Kjeang
Supervisor
Assistant Professor

Siamak Arzanpour
Internal Examiner
Assistant Professor

Date Defended/Approved: March 27, 2013

Partial Copyright Licence



The author, whose copyright is declared on the title page of this work, has granted to Simon Fraser University the right to lend this thesis, project or extended essay to users of the Simon Fraser University Library, and to make partial or single copies only for such users or in response to a request from the library of any other university, or other educational institution, on its own behalf or for one of its users.

The author has further granted permission to Simon Fraser University to keep or make a digital copy for use in its circulating collection (currently available to the public at the "Institutional Repository" link of the SFU Library website (www.lib.sfu.ca) at <http://summit/sfu.ca> and, without changing the content, to translate the thesis/project or extended essays, if technically possible, to any medium or format for the purpose of preservation of the digital work.

The author has further agreed that permission for multiple copying of this work for scholarly purposes may be granted by either the author or the Dean of Graduate Studies.

It is understood that copying or publication of this work for financial gain shall not be allowed without the author's written permission.

Permission for public performance, or limited permission for private scholarly use, of any multimedia materials forming part of this work, may have been granted by the author. This information may be found on the separately catalogued multimedia material and in the signed Partial Copyright Licence.

While licensing SFU to permit the above uses, the author retains copyright in the thesis, project or extended essays, including the right to change the work for subsequent purposes, including editing and publishing the work in whole or in part, and licensing other parties, as the author may desire.

The original Partial Copyright Licence attesting to these terms, and signed by this author, may be found in the original bound copy of this work, retained in the Simon Fraser University Archive.

Simon Fraser University Library
Burnaby, British Columbia, Canada

revised Fall 2011

Abstract

Piezoelectric actuators are increasingly used for the electronic control of fuel injector opening valves. Hydrogen is considered an attractive clean alternative fuel for automobile and power generation applications. Current understanding of the performance of piezoelectric actuators in a hydrogen environment is very limited. This work is aimed at experimentally investigating the performance of hydrogen-exposed piezoelectric actuators under conditions directly relevant to a hydrogen-based fuel injector. The performance is assessed with both quasi-static and dynamic electric loads. It is found that up to 12 weeks of continuous exposure to hydrogen at 100°C and 10 MPa has a negligible effect on the actuator stroke when testing is conducted at temperatures of 5-80°C. Cyclic exposure and exposure done on fatigue cycled actuators also yields similar results. Microstructure and dielectric investigations confirm this behavior. The reason for a negligible effect of hydrogen is attributed to the presence of a protective ceramic insulation around the lateral surface of actuators which deactivates the hydrogen diffusion mechanism. A fully-coupled 3-D FEM-based numerical model of a Thermo-Electro-Mechanical continuum in hydrogen environment is developed using the 'Equation Based Modeling' feature of COMSOL Multiphysics. The model provides a useful tool for understanding the localized responses of the actuators in hydrogen environment and to predict their durability and applicability under different conditions.

Keywords: Piezoelectricity; actuator stroke; fuel injector; hydrogen; diffusion in solids; finite element method

This work is dedicated to my family which was always a pillar of support and a source of strength for me in my good and bad times. I also wish to dedicate this work to the family of Mr. Mohinder Nijjar who supported me when I needed it the most and without whom this degree would never have been possible. Last but not the least, this work is dedicated to my friends, Abhimanyu, Tarun, Santosh, Kapil, Partha and Tanumay, who were a guiding light and an encouraging force behind my decision to pursue a master's degree

Acknowledgements

First and foremost, I would like to acknowledge my thesis supervisors, Dr. Nimal Rajapakse and Dr. Erik Kjeang, for giving me this opportunity in the first place and providing me with invaluable guidance and support during the course of my thesis work. I am also thankful to Dr. Rajapakse for providing me with financial assistance through his NSERC research grant.

I am grateful to Westport Innovations Inc. for providing an in-kind support to my project. The guidance and assistance given by David Mumford, Muhammed Tahir, Johnny Veliath and Bradley Takaki is particularly acknowledged.

I am also thankful to my colleagues, Ali Shafiei, Carmen Oprea, Mohamed Senousy, Mohammad Nouroz Islam at the University of British Columbia, Yasothorn Sapsathiarn at the Simon Fraser University and Dr. Santosh Kapuria at IIT Delhi for taking time out of their busy schedules to address my demands for guidance and support.

And finally, I am thankful to all my friends at the University for helping me with research problems. The discussions, in particular with my roommate Abhishek Nanjundappa during the stressful times, were always comforting and meaningful.

Yadvinder Singh

Table of Contents

Approval.....	ii
Partial Copyright Licence	iii
Abstract.....	iv
Dedication.....	v
Acknowledgements.....	vi
Table of Contents.....	vii
List of Tables.....	ix
List of Figures.....	x
List of Symbols.....	xiii
List of Acronyms.....	xv
1. Introduction	1
1.1. Piezoelectric Materials.....	2
1.2. PZT Ceramics	6
1.3. Piezoelectric Stack Actuators	8
1.4. Piezoelectric Stack Actuators in Fuel Injectors	11
1.5. Self-Heat Generation in Piezoelectric Stack Actuators	14
1.6. Hydrogen in IC Engines.....	15
1.7. Literature Review	17
1.7.1. Experimental Investigation	17
1.7.2. Numerical Modelling.....	20
1.8. Scope of the Present Work.....	21
2. Experimental Investigation	23
2.1. Experimental Procedure	23
2.1.1. Hydrogen Exposure	24
2.1.2. Testing.....	25
2.1.3. Experimental Challenges	30
2.2. Experimental Results and Discussion.....	33
2.2.1. Performance of Unexposed Actuators.....	33
2.2.2. Self-heating in Unexposed Actuators	39
2.2.3. Comparison of PI and KCI Actuators.....	43
2.2.4. Performance of Actuators after Continuous and Cyclic Hydrogen Exposure	44
2.2.5. Explanation for Negligible Hydrogen Effects on Actuator Performance	46
2.2.6. Performance of Fatigue Cycled - Hydrogen Exposed Actuators.....	48
2.2.7. Microstructure and Dielectric Investigation	50
2.3. Summary of Experimental Results.....	51
3. Numerical Modelling.....	53
3.1. Linear Thermo-Electro-Mechanical Material Behaviour	53
3.2. Hydrogen Diffusion in PZT.....	56
3.3. Effect of Hydrogen on PZT Material Properties.....	57
3.4. Numerical Solution using 'Equation Based Modelling' in COMSOL	59

3.5. Model Description.....	60
3.6. Numerical Results and Discussion	63
3.6.1. Case Study I – Unexposed Actuators.....	63
3.6.2. Case Study II – Hydrogen Exposed Actuators.....	65
3.7. COMSOL Model Validation with In-house Thermo-Electro-Mechanical FE Model	69
3.8. Summary of Numerical Results	70
4. Conclusions.....	72
4.1. Summary and Conclusions.....	72
4.2. Recommendations for Future Work	74
References.....	76
Appendices.....	80
Appendix A. Material Properties of PI 885.91 actuators.....	81
Appendix B. FE Formulation of the In-house Thermo-Electro- Mechanical Model	83

List of Tables

Table 2.1. Characteristics of PI-885.91 actuators	24
---	----

List of Figures

Figure 1.1 Direct and Converse piezoelectric effects along with their coupling variables	2
Figure 1.2 Experimental demonstration of: (a) Direct piezoelectric effect; and (b) Converse piezoelectric effect.....	3
Figure 1.3 PZT perovskite structure in: (a) Cubic phase at $T > T_c$; and (b) Tetragonal phase at $T < T_c$	8
Figure 1.4 Typical distribution of forces and displacements generated by a piezoelectric actuator at different applied electrical inputs and mechanical boundary conditions.....	9
Figure 1.5 (a) Bimorph cantilevered piezoelectric actuator; and (b) Piezoelectric disk undergoing expansion due to applied electric voltage.....	10
Figure 1.6 Cross-section of a piezoelectric stack actuator.	11
Figure 1.7 Schematic of a piezoelectric actuator based fuel injector.	12
Figure 2.1 Image of PI-885.91 actuator depicting its external features.....	23
Figure 2.2 (a) Continuous and (b) Cyclic exposure approaches.....	24
Figure 2.3 Schematic of test rig	25
Figure 2.4 Typical quasi-static driving signal.....	26
Figure 2.5 Dynamic driving signal with DC offset	27
Figure 2.6 Sinusoidal driving signal with duty cycle.....	28
Figure 2.7 Half-trapezoidal driving signal with 25 % duty cycle	28
Figure 2.8 Spring-mass model of test system	31
Figure 2.9 Quasi-static stroke-voltage relationship of unexposed actuator for different ambient temperatures	33
Figure 2.10 Quasi-static stroke-temperature relationship of unexposed actuator for different applied voltages.....	34
Figure 2.11 Variation of d_{33} with applied quasi-static voltage at different ambient temperatures for an unexposed actuator.	35
Figure 2.12 Variation of d_{33} with ambient temperature at different applied quasi-static voltages for an unexposed actuator.....	35

Figure 2.13 Quasi-static piezoelectric hysteresis of unexposed actuator at 20°C	36
Figure 2.14 Effect of sinusoidal driving signal frequency on dynamic stroke of unexposed actuator for different driving voltages at 20°C	37
Figure 2.15 Effect of positive DC offset on dynamic stroke of unexposed actuator for different applied voltages at 20°C	37
Figure 2.16 Effect of duty cycle percentage on dynamic stroke of unexposed actuator for different applied voltages at 20°C	38
Figure 2.17 Effect of rise time percentage on dynamic stroke of unexposed actuator for different applied voltages at 20°C	39
Figure 2.18 Temperature rise and dynamic stroke during continuous sinusoidal electric loading under different applied voltages at frequencies; a) 100 Hz; b) 150 Hz; and c) 200 Hz.....	40
Figure 2.19 Variation of steady-state temperature with; a) applied voltage; and b) frequency.....	41
Figure 2.20 Comparison of experimental and theoretical steady-state temperature rise for a continuous 120 V _{pp} sinusoidal signal at 20°C	43
Figure 2.21 Comparative thermal performance of PI and KCl actuators; (a) temperature dependence of quasi-static stroke at 1.8 kV/mm applied electric field; and (b) temperature increase due to self-heating under 200 Hz sinusoidal dynamic excitation	43
Figure 2.22 Effect of continuous hydrogen exposure on actuator stroke at 20°C under; a) quasi-static; and b) 100 Hz sinusoidal dynamic electrical loading.....	44
Figure 2.23 Effect of cyclic hydrogen exposure on quasi-static stroke at 20°C	45
Figure 2.24 a) Cross-section of a typical bulk study sample under hydrogen exposure; and b) mechanism governing diffusion of hydrogen into PZT sample	47
Figure 2.25 Comparison of hydrogen diffusion mechanism in bulk sample and PI actuator.....	48
Figure 2.26 Hydrogen exposure effects on the quasi-static performance of cycled actuator at 20°C.....	48
Figure 2.27 Normalized dynamic stroke of PI actuators during fatigue cycling.....	49
Figure 2.28 Micrographs of lateral surface of; (a) new PI actuators; and (b) after their 12 week hydrogen (100°C, 10 MPa) exposure.....	50

Figure 3.1 Hydrogen exposure conditions for a single PZT stack actuator layer	57
Figure 3.2 Simplified relation for the dependence of d_{33} on H-atoms concentration approximated from the results of Wu et al [5].....	58
Figure 3.3 3-D model of a single PZT layer depicting its dimensions, polarization and prescribed boundary conditions	60
Figure 3.4 Mesh independence analysis: (a) Variation of overall actuator stroke with mesh size when $C_0=0$ ppm, $T_0=20^\circ\text{C}$ and $V_0=120$ Volts; and (b) z-displacement profiles after 10 min. along the x-axis on the top surface of PZT layer for different mesh sizes when $C_0=2$ ppm, $T_0=20^\circ\text{C}$ and $V_0=100$ Volts.....	62
Figure 3.6 Comparison of experimentally measured and numerically evaluated quasi-static stroke-temperature relationship at 100 Volts for an unexposed actuator	64
Figure 3.7 (a) Location of analysis points on the top surface of the model; and (b) Concentration time-history at the analysis points when $T_0=80^\circ\text{C}$ and $C_0=2$ ppm	65
Figure 3.9 Displacement time-history at the analysis points for $T_0=20^\circ\text{C}$ and 80°C , $C_0=2$ ppm and $V_0=100$ Volts	67
Figure 3.10 (a) Concentration profiles; and (b) Displacement profiles; along x-axis on the top surface of PZT layer at different times when $C_0=2$ ppm, $T_0=20^\circ\text{C}$ and $V_0=100$ Volts.....	68
Figure 3.11 (a) Displacement time-history at the analysis points; and (b) Displacement profiles along x-axis on the top surface of PZT layer at different times; when $C_0=1$ ppm, $T_0=20^\circ\text{C}$ and $V_0=100$ Volts	69
Figure 3.12 Stroke-voltage relationship at 20°C under static electric loading obtained from COMSOL model and in-house MATLAB program	70

List of Symbols

σ	Mechanical stress
E	Electric field
T	Temperature, temperature rise from stress-free state
ϵ	Mechanical strain
D	Electric displacement, Diffusion coefficient of H-atoms in PZT
S	Entropy density
s	Elastic compliance coefficient
d	Piezoelectric strain coefficient
α	Thermal strain coefficient
ϵ	Absolute dielectric coefficient
ρ	Pyroelectric coefficient
ρ	Mass density
C_v	Specific heat at constant volume
T_{ref}	Reference temperature
α_v	A material constant dependent on ρ , C_v and T_{ref}
m_{dip}	Electric dipole moment
q_{dip}	Magnitude of each dipole charge
d_{dip}	Distance of separation between dipole charges
P	Electric polarization
P^S	Spontaneous electric polarization
T_c	Curie temperature
V	Electric potential at a point in continuum, applied voltage on actuator
t	Thickness of a single layer of a stack actuator, time
E_c	Coercive electric field
$\delta T, \Delta T$	Actuator temperature rise at time t during a dynamic operation
$\delta T_\infty, \Delta T_\infty$	Actuator temperature rise at steady state during a dynamic operation
τ	Time constant
V_e	Total active volume of actuator
A	Total surface area of actuator
P_r	Remnant polarization
V_{pp}	Peak-to-peak driving voltage

T_p	Time period of periodic signal
T_d	Time period of driving signal
d_t	Duty cycle
V_r	Voltage amplitude in a trapezoidal signal
T_r	Time taken to reach V_r
D_f	Displacement hysteresis
C	Capacitance of the actuator, H-atoms concentration
f	Applied voltage frequency
\bar{h}	Overall heat convection coefficient
A_1	Actuator's surface area exposed to the ambient air
b	Mechanical body force
u, v, w	Mechanical displacement
φ_e	Electric body charge density
q	Heat flux
φ_t	Heat source density
c	Elastic stiffness
e	Piezoelectric stress coefficient
λ	Thermal stress coefficient
κ	Thermal conductivity coefficient
Π	Boundary surface of the continuum
n	Outward unit normal to the boundary Π
\bar{t}	Prescribed surface traction
\bar{Q}	Prescribed Surface charge
\bar{q}	Prescribed surface flux out
h_v	Convection heat transfer coefficient at the surface
T_f	Ambient fluid temperature w.r.t. the stress-free state temperature
J	H-atoms diffusion flux
Δt	Time interval

List of Acronyms

MEMS	Microelectromechanical Systems
ICE	Internal Combustion Engine
PZT	Lead Zirconate Titanate
HPDI	High-Pressure Direct Injection
HCNG	Hydrogen-enriched Compressed Natural Gas
GHG	Greenhouse Gases
KCI	Kinetic Ceramics Inc.
AC	Alternating Current
DC	Direct Current
FE	Finite Element
FD	Finite Difference
UBC	University of British Columbia
CERC	Clean Energy Research Center
DVRT	Differential Variable Reluctance Transducer
RTD	Resistance Temperature Detector
DAQ	Data Acquisition Card
SEM	Scanning Electron Microscope
EDS	Electron Dispersive X-ray Spectroscopy
PDE	Partial Differential Equation
FEM	Finite Element Method

1. Introduction

Smart materials, also known as *intelligent* or *adaptive* materials, are a special class of engineering materials which exhibit coupling between multiple physical domains. Due to this coupling, a stimulus provided in one physical domain can produce a response in another physical domain. The coupled domains may be mechanical, electrical, thermal, magnetic, chemical, and so on. *Piezoelectric materials*, *shape memory alloys*, *electroactive polymers*, *fiber optics*, *magnetostrictive materials* and *electrochromic materials* are a few example materials that exhibit such coupling and therefore, fall under the category of *smart materials*. An engineering system that utilizes the coupling properties of smart materials to provide functionality is called a *smart material system* [16]. Past 2-3 decades have witnessed an increased utilization of the *smart material systems* in diverse engineering applications. From the aircrafts to the microelectromechanical systems (MEMS), from the automobiles to the computers and from the health monitoring of machines to the treatment of cardiovascular diseases in humans, there is an expansive list of disciplines which have benefitted from the distinct functionalities offered by the *smart material systems*.

This chapter discusses one such type of *smart material system* - a stack actuator based on the piezoelectric material. The application of interest is fuel injectors for Direct-Ignition Internal Combustion Engines (ICEs) running on a hydrogen fuel. An overview of the fundamental nature of material and coupling along with the various physical processes involved during the use of piezoelectric actuator in a hydrogen-based fuel injector are presented. The advantages and challenges arising due to the use of such systems in this particular application are outlined. Scope for the current project is defined keeping in mind the project objectives and previous research done in this area.

1.1. Piezoelectric Materials

Certain materials when subjected to an applied mechanical stress, experience the development of an electric charge within them. This mechanical-to-electrical coupling was discovered by Pierre and Jacques Curie in 1880 when they were studying the effect of pressure on natural single-crystal structures like quartz, topaz and Rochelle salt [17]. It was later termed as *direct piezoelectricity* due to the fact that it had been discovered before the discovery, in 1881 by Lippmann, of an electrical-to-mechanical coupling termed as *converse piezoelectricity* and exhibited by the same materials. Both these phenomena along with their respective coupling variables are illustrated in Fig. 1.1. Experiments have revealed that, for a particular material, the value of the coefficient relating the coupling variables in both direct and converse piezoelectricity is, quite remarkably, the same. This coefficient is called the *piezoelectric strain coefficient*. The physical origin of piezoelectricity lies in the unit cell of the materials which exhibit this phenomenon. The unit cells of such materials have been shown to possess a *polar axis* in which there is a separation of positive charges and their associated negative charges. This charge separation produces an *electric dipole* within each unit cell. Interaction of these dipoles with the externally applied stress and/or the externally applied electric field is responsible for the observed piezoelectric behaviour.

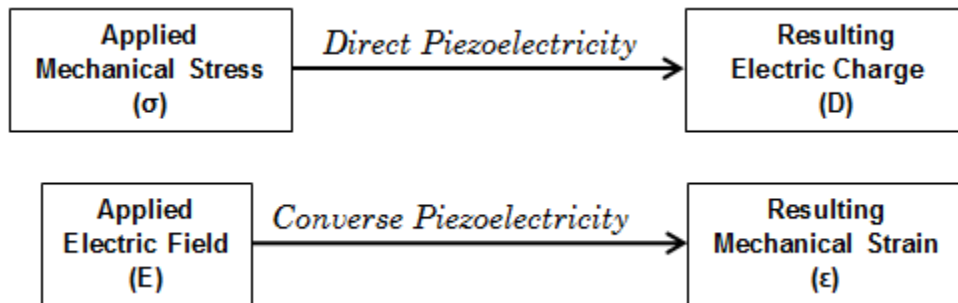


Figure 1.1 Direct and Converse piezoelectric effects along with their coupling variables

Fig. 1.2(a) shows a piezoelectric material specimen having electrodes placed at its two ends and subjected to an applied mechanical stress. The application of stress causes the electric dipoles present within the material to rotate creating an apparent charge flow. This charge flow can be measured at the two electrodes. The charge produced divided by the area of the electrodes is termed as *electric displacement*,

denoted by symbol D and having units of C/m^2 . The generation of this electric displacement due to the application of mechanical stress is the *direct piezoelectric effect*. The most extensive commercial application of the direct effect has been in the development of motion and force sensors. The piezoelectric materials serve as transducer elements for a variety of sensors, viz., accelerometers, activators, dynamic pressure sensors and load cells. Their advantages for these applications are high mechanical stiffness and low mass, which leads to a fast sensing response [16].

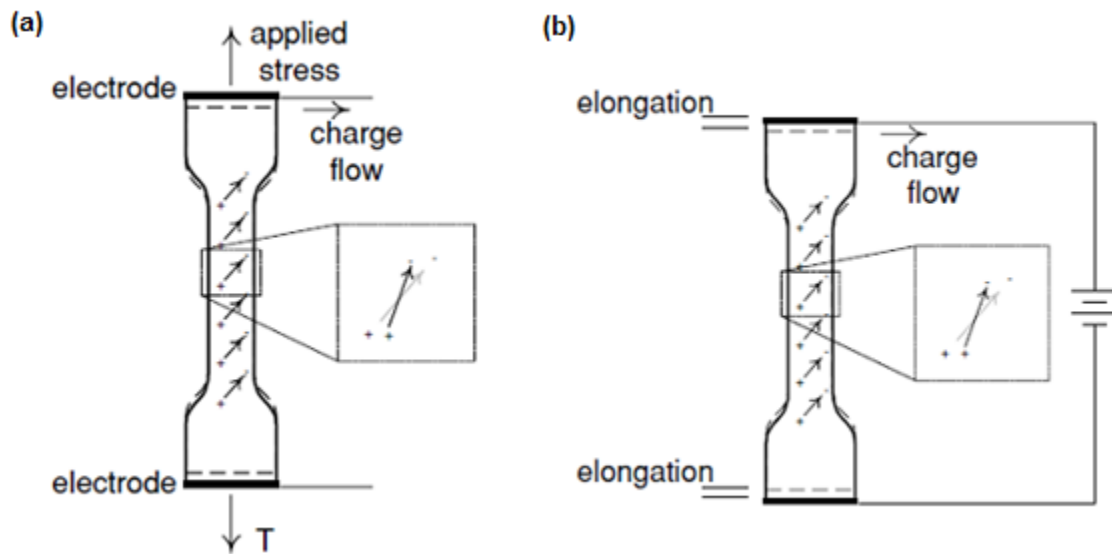


Figure 1.2 Experimental demonstration of: (a) Direct piezoelectric effect; and (b) Converse piezoelectric effect

If instead of the mechanical stress, an electric voltage is applied across the electrodes, there will be an electric field developed within the piezoelectric specimen [Fig. 1.2(b)]. When placed inside an electric field, the electric dipoles present in the unit cells of the specimen will experience a moment resulting in their rotations. These dipole rotations inside each unit cell add up to produce a mechanical strain in the bulk material. The generation of this mechanical strain due to the application of electric field is the *converse piezoelectric effect*. The converse effect exhibited by the piezoelectric materials has been utilized to develop actuators for micro-positioning and force generation applications such as fuel injectors, microelectromechanical systems (MEMS), miniature pumps, micro-fabrication, inchworm motors, and acoustic and vibration control. Modern methods have been developed to utilize the same wafer of piezoelectric material

simultaneously, as both a sensor and an actuator, thus simplifying the design of vibration control systems [16].

In fuel injector applications, a piezoelectric actuator is subjected to simultaneous mechanical, electrical and thermal loading conditions. Under such conditions, the continuum of the piezoelectric material experiences coupling between mechanical, electrical and thermal domains. This means, in addition to the *piezoelectricity* (mechanical \leftrightarrow electrical), *pyroelectricity* (electrical \leftrightarrow thermal) and *thermoelasticity* (mechanical \leftrightarrow thermal) phenomena are also exhibited by the actuator material. Mathematically, this thermo-electro-mechanical coupling can be expressed in the simplest form using *linear constitutive relations* [Eq. 1.1]. These relations are obtained from the first and the second laws of thermodynamics [18]. The state variables within each of the involved domains (mechanical, electrical and thermal) are related to each other. Based on this, while writing the constitutive relations, one of the variables in a particular domain can be viewed as the stimulus given to the material and the other as the response of the material. Depending upon the variables chosen to represent the stimulus and the response, the constitutive relations can be expressed in a number of combinations. For example, if mechanical stress vector (σ), electric field vector (E) and temperature change (T) are chosen as the stimuli and mechanical strain vector (ϵ), electric displacement vector (D) and entropy density (S) are chosen as the responses, the constitutive relations are expressed as follows:

$$\epsilon = s\sigma + d^T E + \alpha T \quad (1.1a)$$

$$D = d\sigma + \epsilon E + pT \quad (1.1b)$$

$$S = \alpha^T \sigma + p^T E + \alpha_v T \quad (1.1c)$$

Where,

s = Elastic compliance coefficient matrix

d = Piezoelectric strain coefficient matrix

α = Thermal strain coefficient matrix

ϵ = Absolute dielectric coefficient matrix

p = Pyroelectric coefficient matrix

$\alpha_v = A$ material constant dependent on density (ρ), specific heat at constant volume (C_v) and reference temperature (T_{ref}) of the material

Superscripted symbols (d^T , α^T and p^T) in Eq. 1.1 represent the transposes of the coefficient matrices. It is important to note that the variable T in the above equation is not the absolute temperature of a point in the continuum. Rather, it represents the temperature relative to the reference temperature (T_{ref}) at which all the material properties are defined. It should also be noted that, due to the electromechanical coupling, the material properties of piezoelectric materials are a function of the mechanical and electrical boundary conditions. This means that for the elastic compliance coefficient (s), the values will be different under open and closed circuit electrical boundary conditions and for the dielectric coefficient (ϵ), the values will be different under stress-free and strain-free mechanical boundary conditions. In Eq. 1.1, short-circuit ($E=0$) and stress-free ($\sigma=0$) values, measured at temperature T_{ref} , are used for s and ϵ respectively.

For a material to exhibit piezoelectricity, a center of symmetry should not be present in its crystal structure, i.e., the crystal structure should be *non-centrosymmetric*. Of the 32 crystal point groups known, 21 are *non-centrosymmetric* and 20 of them exhibit piezoelectricity [19]. Apart from the center of symmetry, other types of symmetries may be present within the crystal structure of the piezoelectric materials. The number of non-zero independent constants within the material coefficient matrices depends upon the presence of these symmetries. For example, the widely used tetragonal *Lead Zirconate Titanate (PZT)* ceramic exhibits hexagonal symmetry resulting in a transversely isotropic material [20] whose coefficient matrices are expressed as,

$$s = \begin{bmatrix} s_{11} & s_{12} & s_{13} & 0 & 0 & 0 \\ s_{12} & s_{11} & s_{13} & 0 & 0 & 0 \\ s_{13} & s_{13} & s_{33} & 0 & 0 & 0 \\ 0 & 0 & 0 & s_{44} & 0 & 0 \\ 0 & 0 & 0 & 0 & s_{44} & 0 \\ 0 & 0 & 0 & 0 & 0 & 2(s_{11} - s_{12}) \end{bmatrix} \quad (5 \text{ independent constants})$$

$$d = \begin{bmatrix} 0 & 0 & 0 & 0 & d_{15} & 0 \\ 0 & 0 & 0 & d_{15} & 0 & 0 \\ d_{13} & d_{13} & d_{33} & 0 & 0 & 0 \end{bmatrix} \quad (3 \text{ independent constants})$$

$$\varepsilon = \begin{bmatrix} \varepsilon_{11} & 0 & 0 \\ 0 & \varepsilon_{11} & 0 \\ 0 & 0 & \varepsilon_{33} \end{bmatrix} \quad (2 \text{ independent constants})$$

1.2. PZT Ceramics

As mentioned in the previous section, the unit cells of certain materials possess electric dipoles. An *electric dipole moment* (m_{dip}) vector is associated with each dipole as follows:

$$m_{dip} = q_{dip} d_{dip} \quad (1.2)$$

Where,

q_{dip} = Magnitude of each dipole charge

d_{dip} = Distance of separation between charges

m_{dip} is directed from the negative to the positive charge within the dipole. In the presence of an external electric field, these dipoles tend to align themselves with the direction of the electric field. The process of dipole alignment is termed as *polarization*. The vector sum of all the dipole moments per unit volume of the material is a physical quantity known as *polarization* (P). Polarization represents the bulk effect of the dipoles present within the unit cells. Normally, in the absence of an external electric field, the dipoles are oriented randomly within the material and the net polarization (*a vector sum*) of the material is zero. There are, however, certain exceptions and there exists a class of materials which have a permanent, non-zero polarization even in the absence of an electric field. Such materials are termed as *Ferroelectrics* and are said to possess a *spontaneous polarization* (P^S) [11]. The ferroelectrics have extremely high dielectric constants and are, therefore, an ideal material for making capacitors. When heated above a certain critical temperature, known as *Curie temperature*, the electric dipoles within the unit cells cease to exist and the ferroelectrics lose their spontaneous polarization.

All ferroelectric materials, having spontaneous polarizations, are also known to exhibit piezoelectricity [22]. *Lead Zirconate Titanate* (*PZT*) ceramics belong to this class

of materials. Since their discovery in 1954, the PZT ceramics have become the most widely used ceramic material for the applications based on piezoelectric phenomenon [23]. For the actuator applications, in particular, the PZT ceramics are desirable due to their fast, reliable and precise performance [24,25,26]. Compared to the other ferroelectric ceramics, these ceramics possess, (a) *higher electromechanical coupling*; (b) *higher Curie temperature*, permitting a higher temperature range during operation; and (c) *wider range of dielectric constants*. Moreover, their manufacturing process is simpler as they can be easily poled by applying an external electric field. [20,27].

The manufacture of synthetic piezoelectric materials typically begins with a mixture of the constituent materials in powdered form. For PZT, this mixture consists of lead (Pb), zirconium (Zr) and titanium (Ti). The processing of piezoelectric ceramic typically begins by heating the powders to temperatures in the range 1200-1500°C. The heated materials are then formed and dimensioned with conventional methods resulting in the ceramic wafers of thickness 50-300 µm. After cooling, the wafers of an unpoled piezoelectric ceramic are obtained. The wafer material does not exhibit any piezoelectric coupling due to the fact that the electric dipoles are pointing in random directions within the material. The dipoles are oriented in a particular direction by a process called *Poling*. During poling, the piezoelectric material is heated above its Curie temperature and then placed in a strong electric field. Heating of the materials allows the dipoles to rotate freely and the electric field produces an alignment of the dipoles along the direction of the electric field. Quickly reducing the temperature and removing the electric field produces a material whose electric dipoles are oriented in the same direction referred to as the *Poling Direction* of the piezoelectric material. Electrodes are placed by painting a thin metallic paint onto the surface on the wafers. The wafers can be cut further using a diamond saw and joined with other layers to produce a multilayer stack actuator [16].

PZT ceramics are binary solid solutions of Lead Zirconate (PbZrO₃) and Lead Titanate (PbTiO₃). They have a perovskite structure with each unit cell consisting of Pb²⁺ ions at the corners, O²⁻ ions at the face centers and a Zr⁴⁺/Ti⁴⁺ ion at the centroid [Fig. 1.3]. Above the Curie temperature (T_c), the PZT perovskite structures are cubic. At lower temperatures, they may be tetragonal or rhombohedral depending upon their composition. Of our interest in the present study are the tetragonal PZT perovskites. In the tetragonal phase, the central Zr⁴⁺/Ti⁴⁺ ion is slightly displaced relative to the plane of

the O^{2-} ions present on the four side faces. This displacement between the positive and negative ions creates a permanent electric dipole within the unit cell resulting in a spontaneous electric polarization (P^S) in the bulk material. This displacement is also responsible for the tetragonal shape produced due to the expansion of the unit in the direction of spontaneous polarization (*poling axis*) and contraction in the other two directions.

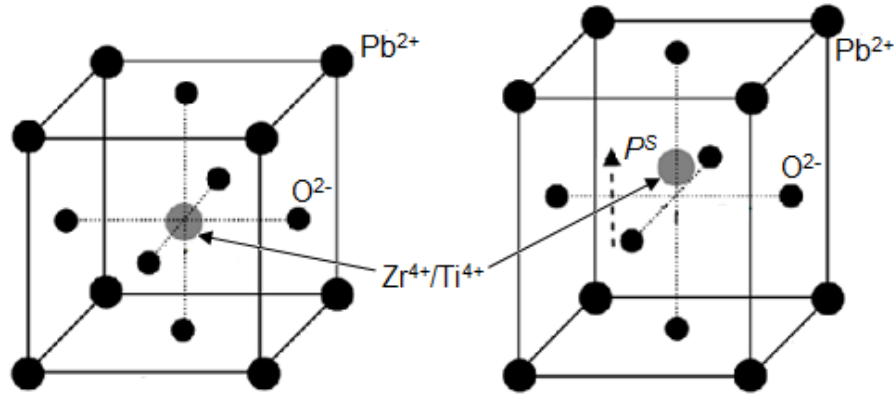


Figure 1.3 PZT perovskite structure in: (a) Cubic phase at $T > T_c$; and (b) Tetragonal phase at $T < T_c$

The properties of PZT ceramics can be controlled by doping the crystals with impurities [28]. *Soft PZT ceramics* are obtained by doping the PZT crystals with donor elements such as Nb^{5+} (to replace Zr^{4+}/Ti^{4+}) or La^{3+} (to replace Pb^{2+}). *Hard PZT ceramics* are obtained by doping the PZT crystals with acceptor elements such as Fe^{3+} (to replace Zr^{4+}/Ti^{4+}). Soft PZT ceramics, being investigated during the present study, have higher piezoelectric coefficients, electromechanical coupling factors and mechanical compliance than the hard PZT ceramics [20].

1.3. Piezoelectric Stack Actuators

The converse piezoelectric phenomenon exhibited by the piezoelectric materials has been utilized to develop actuators. Depending upon the mechanical boundary conditions, the actuators can be used to generate displacements, forces or a combination of them. Fig. 1.4 shows a typical distribution of the forces and displacements generated by a piezoelectric actuator at different applied voltages ($V_1 < V_2 < V_3$). A fully constrained actuator generates only forces and no displacement,

whereas a mechanically free or unconstrained actuator generates only displacements and no forces. The choice of boundary conditions depends upon the application where the actuator is being utilized and the desired force/displacement outputs. The piezoelectric actuators have advantages over conventional actuators because of their light weight, compact design, high speed, easily controllable stroke and resistance to harsh environmental conditions.

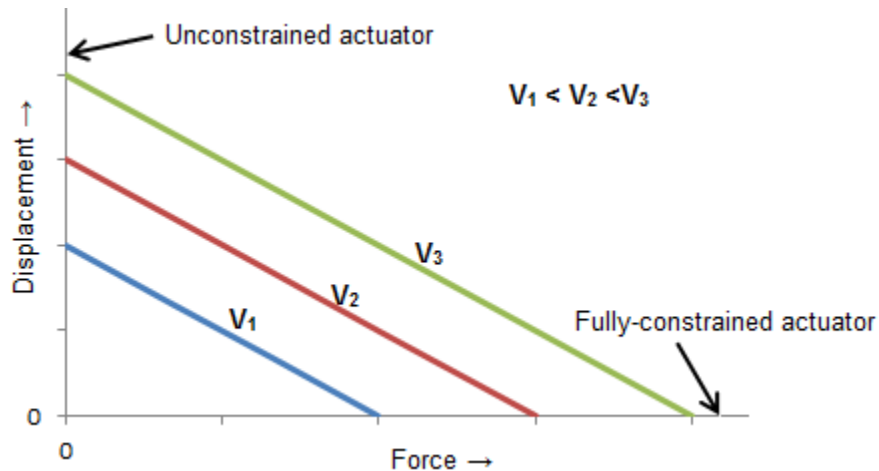


Figure 1.4 Typical distribution of forces and displacements generated by a piezoelectric actuator at different applied electrical inputs and mechanical boundary conditions.

There are mainly two types of piezoelectric actuators as follows:

1. *Flexural piezoelectric actuators*: These actuators are used to produce a bending effect in the structures. They typically cover applications where large displacements but relatively low forces are required to be generated. Fig. 1.5(a) shows a *bimorph* cantilevered piezoelectric actuator. In a bimorph actuator, both the strips are activated upon application of an electrical voltage. The arrangement is such that one of the strips undergoes expansion and the other undergoes compression along the x-axis. Since the two strips are glued to each other, the overall structure experiences bending in the x-y plane. Shape control of helicopter wings, acoustic and vibration control, printing technologies, pneumatic valves, textile machinery etc. are some of the applications where the flexural piezoelectric actuators have found an advantageous use.

2. *Extensional piezoelectric actuators*: These actuators are used to produce expansion or contraction effects in the structures. Due to their high mechanical stiffness, they are typically employed in applications where large forces are required to be generated. These actuators, however, generate very small displacements and therefore, require adoption of displacement amplification schemes to find any utility in positioning applications. Fig. 1.5(b) shows a piezoelectric disk undergoing expansion (ΔL) along its polar axis upon application of an external electrical voltage. Simultaneously, the disk also experiences contraction (ΔD) in the radial direction. The application areas where the extensional piezoelectric actuators have been found to be useful include fuel injection, micro-positioning in general, drum brake actuation, vibration and suspension control etc. [51]

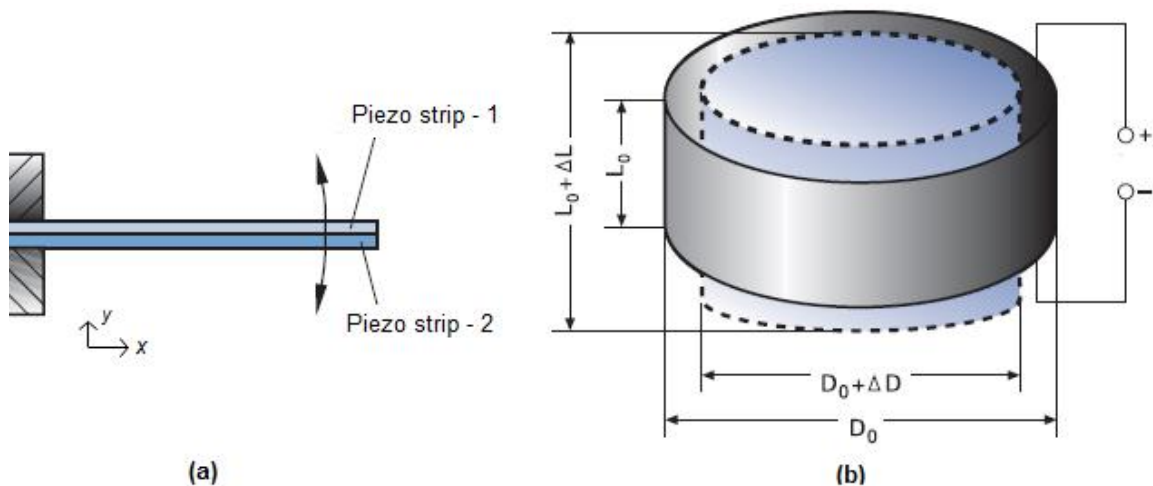


Figure 1.5 (a) Bimorph cantilevered piezoelectric actuator; and (b) Piezoelectric disk undergoing expansion due to applied electric voltage

The disadvantage of small displacements observed in extensional piezoelectric actuators was overcome through an inventive idea that led to the development of *multilayer piezoelectric stack actuators*. These are ‘smart’ structures consisting of hundreds of thin disks of piezoelectric material that are sandwiched between alternate positive and negative electrodes. The disks are mechanically connected in series and electrically connected in parallel. The thickness of each disc is as small as 50 μm and the thickness of electrode is in the order of 5 μm . Fig. 1.6 shows an actuator with the

piezoelectric disks that are polarized in the longitudinal direction. Application of an electric potential V across the electrodes creates an electric field E within each disk in the longitudinal direction ($E = V/t$; t =disc thickness). Due to the converse piezoelectric effect, this electric field results in the development of a mechanical strain within each disk. If the electric field and the polarization directions are same inside the disk, a tensile strain is produced. If they are opposite, a compressive strain is produced. Since the direction of electric field produced in the adjacent disks would be opposite (*due to the alternate positive and negative electrodes*), the direction of polarization of the adjacent disks is also kept opposite to ensure that all the disks within the stack produce a strain in the same direction when an electric potential is applied across the electrodes. Sum of these strains across all the disks translates into the overall stroke of the actuator. Since the electric field is inversely proportional to the disc thickness ($E = V/t$), the desired magnitudes of the electric field can be obtained at relatively lower applied voltages by reducing the disc thickness. This is a notable advantage of piezoelectric stack actuators over the conventional actuators.

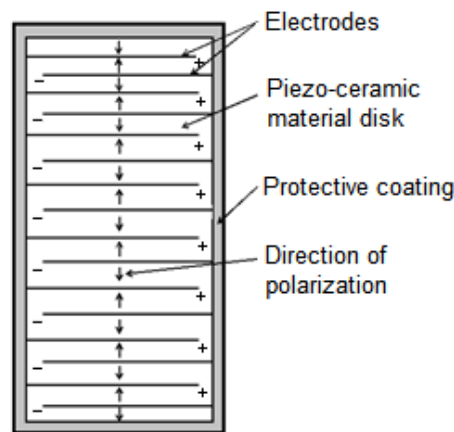


Figure 1.6 Cross-section of a piezoelectric stack actuator.

1.4. Piezoelectric Stack Actuators in Fuel Injectors

In a fuel injector, the fuel supply into the engine cylinder is controlled by the actuation of a valve needle. Pressurized fuel is allowed to enter the cylinder during this actuation period. In the conventional fuel injectors, electromagnetic solenoid technology was employed to control the actuation of the needle. Modern advanced fuel injectors

were later developed that utilized piezoelectric actuators (*instead of solenoids*) to electronically control the needle actuation. A schematic of one such type of Piezo-technology based injector is shown in Fig. 1.7.

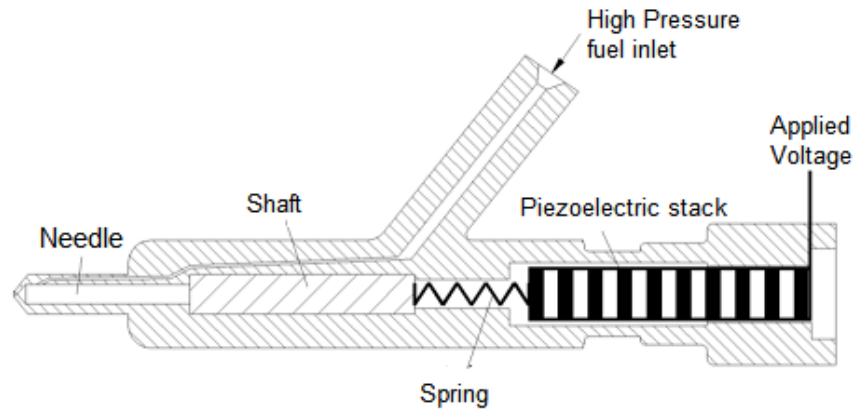


Figure 1.7 Schematic of a piezoelectric actuator based fuel injector.

Investigations had begun in the early 1990s to ascertain the feasibility of using a potentially advantageous PZT stack actuator in the fuel injectors [29]. Many patents came up in the late 1990s which demonstrated that a better fuel metering capability can be attained through the use of piezoelectric actuators in the fuel injectors [30,31]. DENSO Corporation and Toyota Motor Corporation, Japan claimed to have achieved the world's highest fuel injection pressure with the shortest injection interval by the use of piezoelectric injectors [32]. Westport Innovations Inc. based in Vancouver, Canada has developed an innovative High-Pressure Direct Injection (HPDI) system which significantly reduces the emissions from the transportation diesel engines. Advanced fuel injectors, controlled by PZT stack actuators, are a key component in this injection system [20]. Further exploration is in progress to extend this innovative HPDI technology in the systems based on alternative fuels such as natural gas, bio-gas and hydrogen.

The most significant advantage which a PZT stack actuator offers to the fuel injection system is its extremely quick response to an applied electric field. When actuated using a PZT stack, the valve needle [Fig 1.4] can typically respond in less than 0.1 milliseconds allowing the possibility of multiple short-period injections during an injection stroke. This reduces the fuel delivery rate and the energy required from the high-pressure fuel pump [20]. Also, since the valve is actuated more quickly, very precise injection intervals are possible between pre- and main injection resulting in the

reduction of fuel consumption and emissions by up to 15 % [1]. Unlike the fixed valve needle stroke in a conventional solenoid-based electromagnetic injection system, the needle stroke can be varied in the injectors where piezoelectric actuators are used by varying the applied voltage. This enables a better control over the valve opening and provides flexibility in choosing the optimal injection profiles. Experiments conducted by Siemens VDO and Volkswagen have revealed that a better fuel efficiency in the diesel engines can be achieved by increasing the injection pressure of the fuel pump [1]. But as the injection pressure increases, the diesel engine becomes louder due to knocking. This can be avoided by the use of piezoelectric actuators thereby making the engine not only quieter but also more economical. Another advantage which the piezoelectric actuators bring to the fuel injectors is the reduction of applied electrical voltage to a range of below 200 Volts. This is possible because the piezoelectric stack actuator is made up of thin ceramic layers in which the desired electric field can be achieved by applying a relatively smaller voltage [1]. Overall, the advantages of using piezoelectric actuators over the conventional electromagnetic solenoid technology are that they provide an optimized injection system which is quieter, more powerful, more economical and less polluting.

In order to obtain a substantial amount of stroke from the stack actuators, they have to be subjected to relatively high electric field magnitudes (~ 2.4 kV/mm) which are much greater than the typical coercive electric field E_c values. This means going into the region of non-linear response of the actuators to the applied electric field. This is not desirable, particularly for the fuel injector application requiring precise positioning of the needle, and puts additional requirements on the control systems. Due to the operational requirements of fuel injection systems, the actuators are subjected to high frequencies (>100 Hz) and high temperatures (up to 120°C). The dynamic operation at high frequencies and high electric field magnitudes causes self-heat generation inside the actuators. This self-heat combined with the high operational temperatures can accelerate material aging. It may also produce thermal stresses which can lead to a structural failure by debonding the interface between the ceramic layer and electrodes [33]. The PZT ceramics have low fracture toughness (less than $1 \text{ MPa } \sqrt{\text{m}}$) and therefore, a strong propensity for cracking. This characteristic also poses a challenge in designing suitable actuators for the dynamic operation expected in a fuel injector.

1.5. Self-Heat Generation in Piezoelectric Stack Actuators

During a dynamic operation of a PZT stack actuator, self-heating phenomenon is observed even in the linear range of operation. It is caused by energy losses such as mechanical damping and dielectric loss. Ferroelectric hysteresis loss, believed to be caused by domain switching, is the major contributor to the dielectric loss [14,41,42]. The temperature rise in the PZT actuators due to self-heat generation can substantially affect their overall performance and durability, and may limit their applications. Electromechanical coupling coefficients, resonance frequencies and oscillation amplitudes of piezoelectric elements are some of the important characteristics that can get affected due to self-heating resulting in an unreliable actuator performance [43]. From an operational point of view, self-heating has a direct effect on current consumption and total displacement of an actuator [44]. Therefore, self-heat generation in a PZT stack actuator can be a serious issue in the fuel injection applications where a precise accuracy is required.

The mechanism of self-heating in piezoelectric materials was theoretically modelled by Zheng *et al* [45]. Their model was based on the law of energy conservation and the assumption that the rate of heat generation was directly proportional to the frequency and hysteresis loss per driving cycle per unit volume. The model provided a closed-form solution of temperature increase during a dynamic operation and represented it in the form of classical exponential variation with respect to time as

$$\delta T = \delta T_{\infty}(1 - e^{-t/\tau}) \quad (1.3)$$

where δT and δT_{∞} are the actuator's temperature rise at time t and at steady state respectively. τ is a time constant dependent on the actuator material and geometry. The effect of heat dissipation from the actuator by convection and/or radiation was later added to this model by Lesieutre *et al* [46]. A more comprehensive model based on a similar approach and relevant to the fuel injection application was developed by Senousy *et al* [47]. This model accounted for different parameters such as geometry, magnitude and frequency of applied electric field, duty cycle percentage and surrounding properties.

Experimental investigations to study the effect of actuator geometry on self-heating were performed by Zheng *et al* [45]. Five different actuator sizes with varying layer thicknesses were tested under different operating conditions at room temperature. The steady state temperature rise δT_{∞} was found to increase linearly with the ratio V_e/A (V_e and A are the total active volume and the total surface area of the actuator, respectively). The steady state temperature rise δT_{∞} was also found to increase with increased applied electric field and frequency.

1.6. Hydrogen in IC Engines

The present day transportation sector is heavily reliant on fossil fuels such as gasoline and diesel. Fossil fuel combustion releases large amounts of greenhouse gases, the most significant being carbon dioxide. Presence of these greenhouse gases in the earth's atmosphere does not allow the heat coming from the sun to escape out of the atmosphere, thereby resulting in the increase of earth's average temperature. This phenomenon is termed as *global warming* and the use of fossil fuels in the transportation sector is a major contributor to it. The global warming is receiving a world-wide attention as a significant environmental problem. In addition to the greenhouse gases, the combustion of fossil fuels also produces other *air pollutants*, such as nitrogen oxides, sulfur dioxide, volatile organic compounds and heavy metals. These pollutants can prove to be hazardous to the human and animal health as well as the global ecosystem. Another concern associated with an excessive dependency on the fossil fuels is *energy security*. The fossil fuels are limited in supply and are getting depleted quickly due to their accelerated global consumption. Therefore, an unprecedented interest currently exists in the transportation sector to find alternatives to the fossil fuels that are renewable and produce minimal amounts of greenhouse gases and other harmful pollutants. Natural gas, bio-fuels, hydrogen and electricity are amongst the primary candidates being explored for this purpose.

Hydrogen as an energy source for vehicles is still being developed but is extremely promising. Combustion of hydrogen in automobiles produces no greenhouse gases or air pollutants except for traces of nitrogen oxides (NOx) when burned in IC engines. This makes hydrogen a clean and environmentally friendly fuel. Hydrogen can

be produced from diverse sources using a variety of process technologies. Hydrogen-containing compounds such as fossil fuels, biomass or even water can be a source of hydrogen [35]. There is, therefore, a tremendous scope for localized production of hydrogen which can curtail the dependencies that exist in the form of petroleum imports. This would help towards achieving a global energy security. There are, however, certain challenges that need to be addressed before a commercial utilization of hydrogen as a transportation fuel gets widespread acceptance. Due to its relatively low volumetric energy density, transportation, storage and delivery to the point of use can be one of the significant costs and energy inefficiencies associated with using hydrogen as an energy carrier. Hydrogen is also highly reactive chemically and diffuses into almost every material. A vehicle powered with hydrogen may use it directly for running the IC engines or convert it into electricity using fuel cells. In both cases, hydrogen is stored on-board and can be used to replenish the IC engine or fuel cell just like a traditional diesel or gasoline engine.

An early attempt to use hydrogen in the IC engines was made by N. A. Otto in 1860s when he reportedly used a synthetic producer gas for fuel, which probably had a hydrogen content of over 50%. Due to the development of safe gasoline engines, hydrogen received very little attention as a transportation fuel for IC engines in the following years. It remained, however, the fuel of choice for rocket engines because of its highest energy-to-weight ratio compared to any other fuel. The properties which make hydrogen a suitable combustible fuel for an IC engine are:

- Wide range of flammability allowing for a wide range of fuel-air-mixtures
- Low ignition energy
- Small quenching distance
- High auto-ignition temperature allowing for higher compression ratios
- High flame speed
- High diffusivity resulting in a uniform air-fuel mixture

Hydrogen's lower ignition energy, wider flammability range and shorter quenching distance, however, can cause a problem of premature ignition in the IC engines. Premature ignition occurs when the fuel mixture in the combustion chamber becomes

ignited before ignition by the spark plug, and results in an inefficient, rough running engine. Backfire conditions can also develop if the premature ignition occurs near the fuel intake valve and the resultant flame travels back into the induction system. Also, hydrogen has a very low density resulting in a bulkier storage system and a low power output compared to the gasoline and diesel engines [36].

Westport Power Inc., Vancouver is the leading Canadian developer of internal combustion engine technology based on clean-burning fuels such as natural gas, hydrogen and Hydrogen-enriched Compressed Natural Gas (HCNG). Westport has been developing hydrogen-based internal combustion engine technology since early 2000 and is collaborating with Ford and BMW in this area. Westport's HCNG engines run on 20% hydrogen (by volume) and 80% natural gas. These engines emit 65% less nitrogen oxides (NO_x), 80% less particulate matter and about 10 tonnes per year less greenhouse gases (GHG) than similar sized engine using gasoline or diesel fuel.

1.7. Literature Review

1.7.1. *Experimental Investigation*

The performance of piezoelectric stack actuators under conditions that are similar to the operating conditions of a fuel injector has received some attention in the past. Quasi-static thermo-electro-mechanical performance of cylindrical actuators made from soft PZT material and manufactured by Kinetic Ceramics Inc. (*KCI*) was investigated by Li *et al* [2] over a temperature range of -30 °C to 125 °C under driving-electric fields varying from 0.3 to 1.8 kV/mm. They reported that the electrically-induced stroke of the actuator increased steadily with temperature. At higher applied electric fields, a non-linear transition zone existed in the stroke-temperature plot over the temperature range 25-50°C. The dielectric constant was also found to increase with temperature. The actuator stroke showed a bilinear dependence on the applied electric field with a point of inflection occurring at 0.3 kV/mm in the stroke-driving field plot. The preload dependence of the stroke was found to be negligible up to 30 MPa.

A comprehensive investigation of the dynamic thermo-electro-mechanical performance of smaller sized actuators from the same manufacturer (*KCI*) was carried

out by Senousy *et al* [3]. The actuator response was studied over a temperature range of -30°C to 80°C under sinusoidal and trapezoidal AC electric fields of up to 2.8 kV/mm, frequencies of up to 400 Hz and various duty cycles, rise times and DC offset voltages. At low frequencies (≤ 100 Hz), the relationship of dynamic stroke to applied electric field as well as temperature followed a trend similar to that of the quasi-static stroke reported by Li *et al* [2]. Although the dynamic stroke showed a positive increase with increasing frequencies (*above 100 Hz*) and decreasing rise times, the accuracy of the observed relationships is debatable due to the presence of system vibrations caused by resonance. The biased DC offset voltage was found to slightly affect the dynamic stroke of PZT actuators by reducing the extrinsic contribution due to non-180° domain walls. In addition to performance testing, the temperature increase due to self-heat generation during a dynamic operation and its effect on the actuator response was also studied. Self-heating was found to increase non-linearly with both applied electric fields and frequencies. Although the duty cycle had almost no effect on the dynamic stroke, it linearly increased the self-heat generation inside the actuators.

Fatigue responses of PZT stacks (*Noliac, Denmark*) under semi-bipolar electric cycling were experimentally investigated by Wang *et al* [4]. The stacks were cycled for more than 10^8 cycles using a 100 Hz semi-bipolar sine wave with an electric field range of +4.5/-0.9 kV/mm. Significant reductions in piezoelectric and dielectric responses were observed during the cycling. Possible damage mechanisms including electrode delamination, pores and etch grooves were revealed during microstructure investigations.

Although the experiments conducted by Li *et al* [2], Senousy *et al* [3] and Wang *et al* [4] were targeted towards the fuel injector applications, they all were performed in an air environment. The impact of the type of fuel on the PZT stack actuator performance was not assessed during these studies. This was mainly due to the reason that the injector can be sealed completely from traditional hydrocarbon fuels and there is no chemical reaction with PZT. This, however, is not true for hydrogen-based fuel injectors due to the fact that hydrogen is highly diffusive and chemically reactive.

Past studies have indicated that hydrogen can have deleterious effects on the properties and microstructure of the PZT material. Experiments conducted by Wu *et al*

[5] have shown that the piezoelectric properties (*piezoelectric constant* d_{33}) and the ferroelectric properties (*remnant polarization* P_r) of a bulk PZT material are strongly influenced by the content of hydrogen trapped inside. According to their results, the values of both d_{33} and P_r increased respectively by 45.3% and 27.3% when the concentration of trapped hydrogen (C_t) inside PZT increased to 1.1 wppm. These values, however, began to decrease when C_t was increased further and at $C_t = 2.1$ wppm, the PZT material was found to have lost its ferroelectric nature i.e. $P_r = 0$. It was also found that at $C_t = 2.1$ wppm, the resistivity of PZT ceramics is less than $10^9 \Omega\text{m}$ where the material becomes a semiconductor. The dielectric constant and the dielectric loss of the PZT ceramics was also reported to have increased with the rise of C_t . Peng *et al* [6] observed hydrogen-induced initiation and growth of micro-cracks along the grain boundaries of PZT. Wang *et al* [7] observed reduction in the values of mechanical properties (*strength & fracture toughness*) with increased hydrogen content inside PZT. Alvine *et al* [53] investigated the structural and compositional changes occurring in thin (50 nm) PZT films under hydrogen exposure conditions (13.8 MPa , 100°C) comparable to a typical fuel injector. After 24 hours of hydrogen treatment, they observed hydrogen-induced blistering on the surface of bare PZT films and PZT films with Pd electrodes. They also observed significant mixing of Pd layer into the PZT film along with migration of Pb into the Pd layer. According to their results, the absorption of hydrogen into PZT increased due to the presence of Pd layer. Recent studies conducted by Shafiei *et al* [8, 9, 10] indicate changes in the microstructure and electrical properties (*capacitance, resistance, dissipation factor*) of hydrogen treated PZT material. They also observed that the degradation in PZT is accelerated by the presence of electrodes. The degradation consisted of the development of a porous layer just beside the electrodes on the PZT surface, detachment of the electrodes from the PZT and extensive damage to the Ag/Pd electrodes. According to Shafiei *et al* [9], a new structure is possibly formed in PZT upon exposure to hydrogen. Protons are expected to be the constituents of this new structure, and the changes in the electrical properties can be attributed to their presence. It should be noted that all of the above mentioned studies have been conducted on bulk PZT material.

From the above results obtained for the bulk PZT material, it is expected that the performance of PZT-based stack actuators in a hydrogen environment will be different

from that in air. The differences, however, may not be exactly similar to those observed in these studies. This is because, unlike the bulk material, a PZT-based stack actuator is a more complex structure containing multiple PZT layers, electrodes, protective coating etc. which may further complicate the interaction between actuator and hydrogen [Fig. 1.6]. Therefore, in order to effectively utilize the PZT-based piezoelectric actuator technology in the fuel injectors of hydrogen-based IC engines, it is imperative that a comprehensive understanding of the behaviour of these actuators under applicable hydrogen environment and loading conditions is developed. The present research effort is the first experimental attempt aimed at gaining this understanding.

1.7.2. Numerical Modelling

In addition to the experimental work, finite element (FE) modelling has been used in the past to theoretically predict the behaviour of piezoelectric materials. These models utilize the constitutive relations to incorporate the coupling effects exhibited by these materials. A comprehensive survey of the finite element modelling of piezoelectric materials for adaptive structure applications was provided by Benjeddou [37]. Senousy *et al* [38] developed a 2-D fully-coupled linear thermo-electro-mechanical finite element model based on the weighted-residual principle. This model was later extended to account for the non-linear material behaviour caused by non-linear constitutive relations and/or domain switching effects [39]. It successfully predicted the experimentally obtained D_3 - E_3 and ϵ_{33} - E_3 hysteresis loops at different applied electric field magnitudes, stress preloads and temperatures. It also provided a better prediction of the 'butterfly loops' than the previous models. Sapsathiarn *et al* [40] developed a finite difference (FD) model to simulate the non-linear diffusion process of hydrogen in the PZT material. This FD model was later coupled to the linear thermo-electro-mechanical FE model [38] and included the dependence of d_{33} on hydrogen concentration as reported by Wu *et al* [5]. This model was used to theoretically analyse the time-histories and spatial profiles of temperature, hydrogen concentration and displacement within the PZT stack actuator layer exposed to hydrogen.

These 2-D models were developed for a single layer in a stack actuator assuming plane stress conditions in one of the lateral directions. This assumption is useful enough for predicting the trends in an actuator response but does not completely

simulate the real-world conditions in which the actuator has comparable lateral dimensions and therefore, no plane stress conditions. This means that it is necessary to develop a 3-D finite element model in order to fully simulate the actual physics involved when a piezoelectric stack actuator is run in hydrogen environments. This has also been attempted for the first time in the present research effort.

1.8. Scope of the Present Work

Based on the literature review presented in the previous section, it is evident that the current understanding of thermo-electro-mechanical performance of PZT-based stack actuators in hydrogen environment under conditions relevant to fuel injection systems is still in its infancy. Further research efforts are necessary to answer some of the critical research questions before a commercial implementation of this technology is pursued. Therefore, this thesis has two main objectives:

1. To experimentally study the thermo-electro-mechanical performance of PZT-based stack actuators under operating conditions relevant to the fuel injection systems after exposing the actuators to relevant hydrogen environment conditions.
2. To theoretically model the response of a 3-dimensional hydrogen-exposed piezoelectric actuator using linear thermo-electro-mechanical constitutive relations.

A comparison between the experimental results from the first objective and the theoretical results from the second objective is also presented.

The organization of this thesis is as follows: in Chapter 2, the thermo-electro-mechanical performance of soft PZT-based stack actuators manufactured by *PI Ceramic, Germany* is experimentally investigated. The actuators, after exposure to relevant hydrogen environment conditions, are examined under both quasi-static and dynamic applied voltages of 10-120 Volts magnitude over a temperature range 5-80°C. The effect of different applied frequencies, excitation waveforms, duty cycles, rise times and DC offset voltages on the actuator performance is also studied. Additionally, self-heating in the actuators under different applied voltage magnitudes

and frequencies is investigated. The observed results are also validated by carrying out microstructure and dielectric investigations.

In Chapter 3, a 3-dimensional finite element model of a single PZT stack actuator layer exposed to hydrogen environment is presented. Concentration gradient is assumed to be the driving force responsible for causing diffusion of hydrogen atoms into the PZT layer. The diffused hydrogen atoms affect the piezoelectric strain coefficient d_{33} of the PZT as per the experimental results reported by Wu *et al* [5]. This model takes into account a full coupling between mechanical, electrical, thermal and diffusion variables. It is also a non-linear model due to the dependency of coefficient d_{33} on hydrogen concentration variable. The conclusions of the present study and the recommendations for future work are presented in Chapter 4.

2. Experimental Investigation

2.1. Experimental Procedure

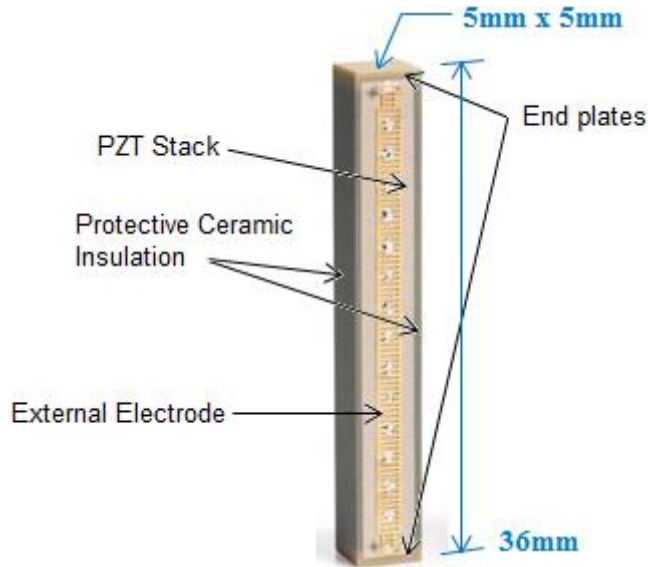


Figure 2.1 Image of PI-885.91 actuator depicting its external features

Piezoelectric actuators made from stacks of soft PZT material, having dimensions 5 mm x 5 mm x 36 mm and manufactured by PI Ceramic, Germany (*Model-885.91*) were used in this work. Fig. 2.1 shows some of the external features of an original PI-885.91 actuator which was experimentally tested during the present study. Table 2.1 shows some of the important characteristics of these actuators. The exposure of actuators to hydrogen was done in a hydrogen-safe chamber available at the University of British Columbia (*UBC*) Clean Energy and Research Center (*CERC*). Experiments concerning quasi-static and dynamic performance evaluation, self-heat generation, dielectric behavior and fatigue cycling effects, similar to those conducted by Li *et al* [2], Senousy *et al* [3] and Wang *et al* [4], were performed on these actuators using a test rig and other facilities available at Westport Innovations Inc., Vancouver. Microstructure investigation of the actuators was carried out at Electron Microscope Laboratory of the Materials Engineering Department at the UBC. A detailed description of the hydrogen exposure approaches and the type of tests conducted is provided in the subsequent sections.

Table 2.1. Characteristics of PI-885.91 actuators

Actuator property	Value
Curie temperature (°C)	350
Stiffness (N/μm)	25
Electrical capacitance (μF) *	3.1±20%
Operating voltage (V)	-30 to +130
Piezoelectric strain coefficient d_{33} (pC/N)	400
PZT Layer thickness (μm) **	53 (approx.)
Number of layers **	600 (approx.)

* Capacitance at 1 V_{pp}, 1 kHz

** Measured under microscope

2.1.1. Hydrogen Exposure

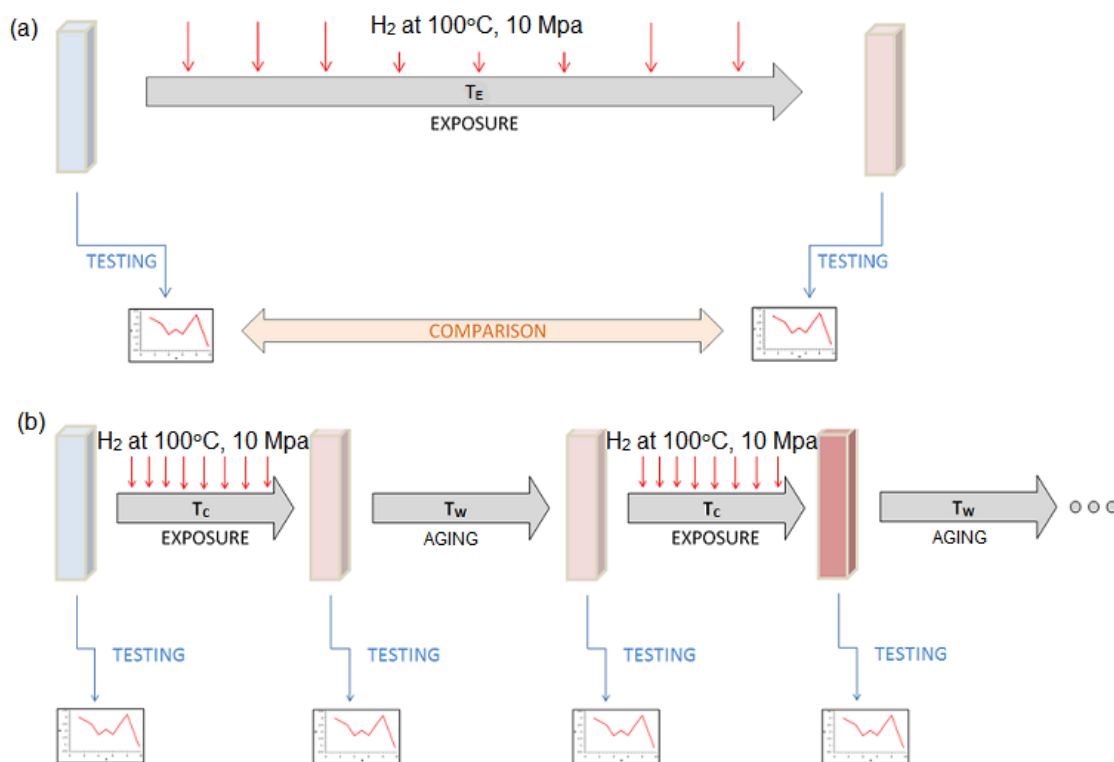


Figure 2.2 (a) Continuous and (b) Cyclic exposure approaches

Two different types of approaches, namely; (a) *the continuous approach*; and (b) *the cyclic approach* were employed to carry out the exposure of actuators to hydrogen. In the continuous approach, different actuator sample sets were placed in the

hydrogen chamber continuously for a time duration $T_E = 4, 9$ and 12 weeks. Each sample set was withdrawn from the chamber after the completion of desired exposure duration following which the testing was conducted. In the cyclic approach, one sample set was placed in the chamber for time $T_C = 4$ weeks \rightarrow Tested after withdrawal \rightarrow Kept outside the chamber for aging at room temperature for time $T_W = 4$ weeks \rightarrow Tested again for aging effects \rightarrow Placed back into the chamber to repeat the same cycle. Both the approaches are graphically illustrated in Fig. 2.2. The temperature and pressure inside the chamber were maintained at 100°C and 10 MPa respectively for all exposures and were chosen according to the practical conditions expected in a typical fuel injector [8]. Each sample set consisted of two actuators.

2.1.2. Testing

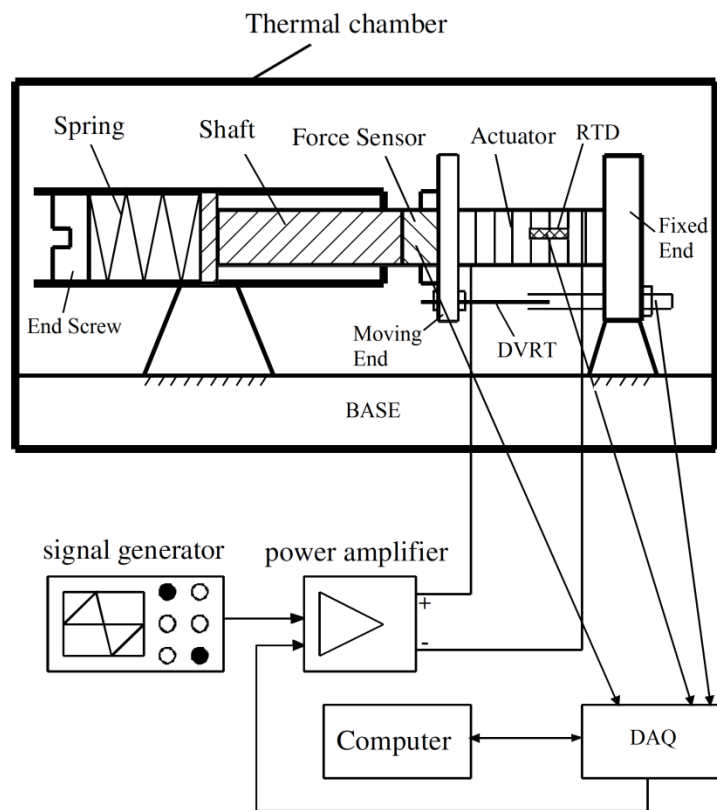


Figure 2.3 Schematic of test rig

A schematic of the test rig is shown in Fig. 2.3. Testing was conducted by placing the rig inside a thermal chamber (*TestEquity[®] Model 1007C*) having temperature

controlled to $\pm 0.1^\circ\text{C}$. The actuator was mounted in a groove on the moving end such that its polar axis was aligned with the axis of the shaft. Using an end screw and a spring ($k = 25 \text{ N/mm}$), a compressive preload was applied to the actuator in order to tighten it between the moving end and the fixed end. Such a preload is also present in fuel injectors for the purpose of alignment, counteracting stress concentrations and other design requirements [3,4]. Preload of approx. 2 MPa was applied during quasi-static loading and approx. 15 MPa during dynamic loading which was measured using a force sensor (*Futek*[®]) placed between the shaft and the moving end. The elongation or contraction of the actuator, due to the applied electric voltage, causes a displacement of the moving end w.r.t. the fixed end. This displacement is the actuator stroke and was measured using a Differential Variable Reluctance Transducer (DVRT) (*Microstrain*[®]) having a resolution of $\pm 0.1 \mu\text{m}$. A Resistance Temperature Detector (RTD) was attached to the surface of the actuator to measure its surface temperature. The electrical energy in the form of voltage for driving the actuator was provided by a power amplifier. Output voltage from the power amplifier was controlled either manually using a signal generator (*Agilent*[®]) or automatically using a Data Acquisition Card (DAQ) (*National Instruments*[®]). Measurements, in the form of voltage signals, from force sensor, DVRT and RTD were input simultaneously into the DAQ and fed to the computer software (*LabView*[®]) where they were interpreted in terms of their real physical units after applying suitable calibration scaling.

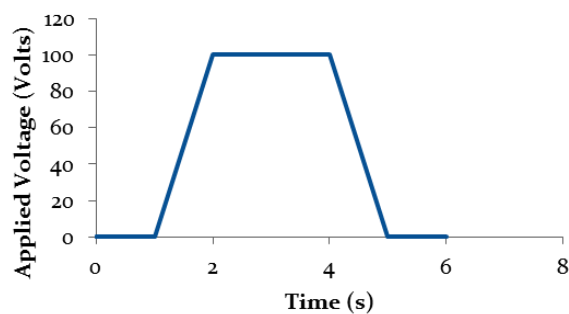


Figure 2.4 Typical quasi-static driving signal

Quasi-static testing was carried out by driving the actuator with a voltage signal which is ‘infinitely slow’ from a fuel injector application viewpoint. Fig. 2.4 shows a typical example. The voltage takes 1 sec to linearly reach the maximum value, has a holding time of 2 sec at the maximum value and decreases back to zero linearly in 1 sec.

Actuator stroke was measured at different voltages (10-120V) and ambient temperatures (5-80°C).

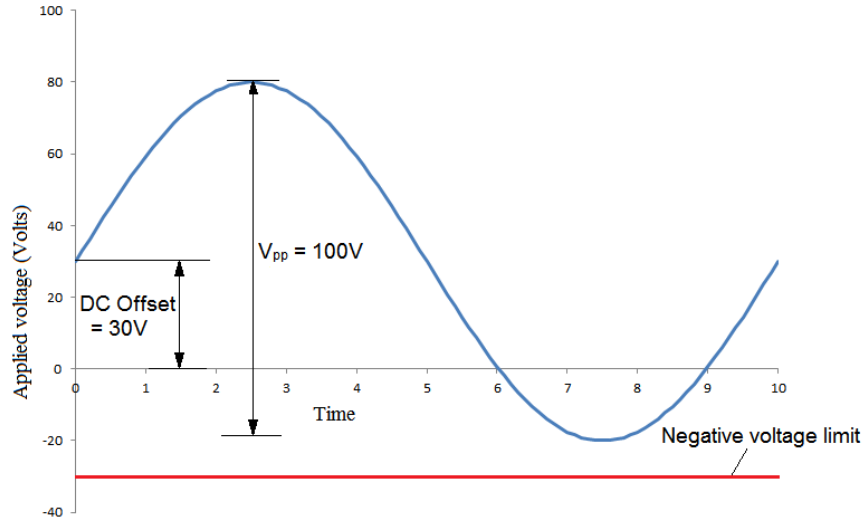


Figure 2.5 *Dynamic driving signal with DC offset*

During practical situations, the actuators are driven at a certain frequency. This frequency is an important parameter that controls the functioning of a fuel injector. The effect of sinusoidal driving signal frequencies of up to 200Hz was investigated during the dynamic testing. The tests were conducted at different peak-to-peak driving voltages (10-120V_{pp}) and ambient temperatures (5-80°C). It should be noted that the maximum negative voltage prescribed for these actuators is -30 Volts [Table 2.1]. Accordingly, it was necessary to use a positive DC offset in order to apply peak-to-peak driving voltages of up to 120V_{pp}. For example, to apply a 100V_{pp} signal, a DC offset of +30V was used to ensure that the negative voltage does not go beyond the prescribed limit [Fig. 2.5].

In many applications, including fuel injectors, the driving signal on the actuator is not applied continuously. There is usually a time gap between the finishing point of one signal and the beginning of next signal. If the time gap is constant, the entire signal can be altogether viewed as a periodic signal repeating with period T_p as shown in Fig. 2.6. *Duty Cycle* d_t is defined as the ratio of driving signal time period T_d to the periodic signal time period T_p i.e., $d_t = T_d / T_p$. A duty cycle of 100% means a continuous driving signal,

while a 0% duty cycle implies no signal or a DC signal. The actuator stroke was measured for different duty cycle values (25-100%).

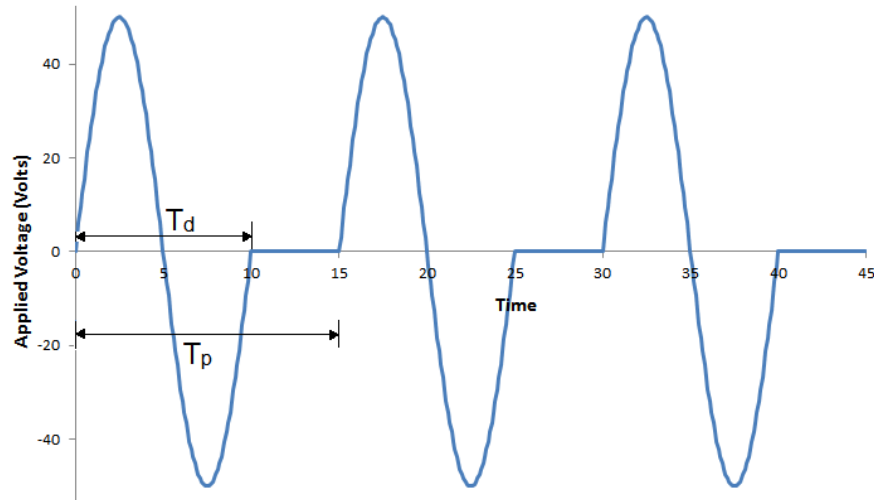


Figure 2.6 Sinusoidal driving signal with duty cycle

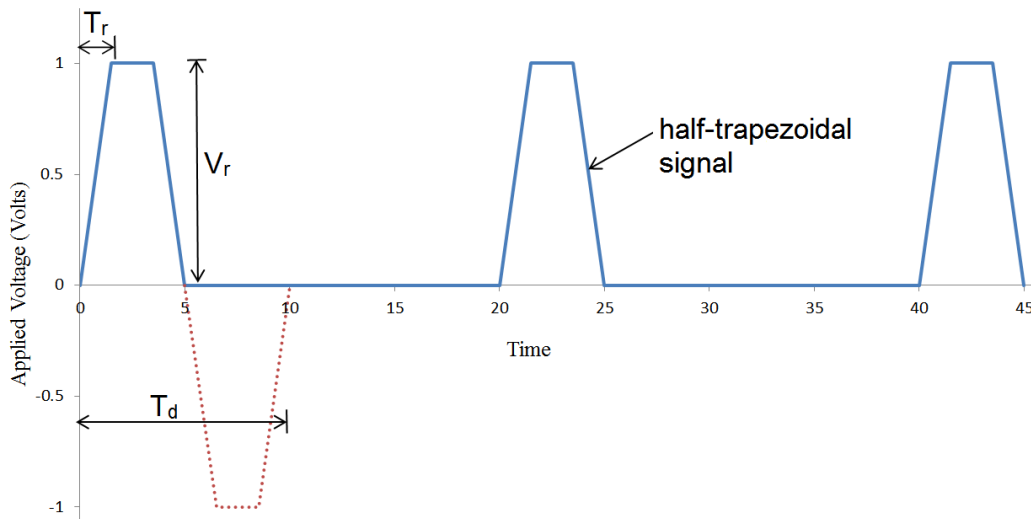


Figure 2.7 Half-trapezoidal driving signal with 25 % duty cycle

In addition to the sinusoidal signal, actuator's response to a trapezoidal driving signal was also investigated. *Rise time percentage* for a trapezoidal signal is defined as the ratio of time T_r taken for reaching the maximum voltage V_r to the driving signal time period T_d [Fig. 2.7]. When the *Rise time percentage* was decreased, the moving parts experienced a greater acceleration. The response measured by the DVRT during such

tests was overlapped with vibrations caused by the inertia of moving parts. In order to detect the actuator stroke most accurately, a half-trapezoidal signal was applied at a 25% duty cycle allowing sufficient time for the vibrations to damp out. Tests were conducted to investigate the dependence of the actuator stroke on the *Rise time percentage* (2.5-20%) at different voltages V_r and frequencies (or time period T_d).

During a dynamic operation involving continuous electrical loading-unloading cycles, there are piezoelectric and dielectric hysteresis losses in a piezoelectric actuator. These losses result in self-heat generation within the actuator material causing its temperature to rise. When operated at typical fuel injection frequencies, there can be a significant amount of temperature increase that can affect the properties of the PZT material. The effect of driving signal voltage and frequency on this temperature increase was also investigated during the dynamic tests.

The general step-by-step procedure for conducting all type of tests was:

1. Mounting the piezoelectric actuator on the moving end.
2. Preloading the actuator to the desired value by tightening the spring using the end screw.
3. Performing a check to make sure that all the sensors are properly mounted and give correct pre-test outputs.
4. Choosing the desired driving voltage signal depending on the type of test to be performed.
5. Firing the actuator with the chosen signal from the power amplifier controlled by signal generator or DAQ.
6. Recording data from all the sensors using DAQ.

Additionally, a few tests were also conducted to examine the effects of hydrogen exposure on the dielectric response of the actuators. This was done using a high-resolution impedance analyser LCR817 (*InsteK*[®]).

2.1.3. Experimental Challenges

A number of challenges were encountered during the experimental phase which demanded expenditure of effort and time in addition to that spent on conducting the experiments. Some of the major challenges are described as follows:

- i. During the initial phase of testing, the DVRT gave an inconsistent response under similar repeated conditions. The problem did not solve even after a re-calibration was performed by its manufacturer. After extensive troubleshooting efforts it was found that one of the components in the test rig was fabricated from a magnetic material. When the actuators were operated by applying electric fields, this component used to get magnetized and the induced magnetic field interfered with the functioning of the DVRT resulting in inconsistent outputs. The magnetic component was subsequently replaced with a non-magnetic material and consistency in the DVRT response was achieved.
- ii. The natural frequency of the test system was calculated to be approx. 500 Hz. When the operating frequency of the actuator approached this value, vibrations developed in the system and the stroke of the actuator at such frequencies could not be accurately measured due to the superposition of vibrations. This was particularly deterrent during the *Rise Time Testing* which involved greater accelerations of the moving parts than during a sinusoidal driving input. In order to overcome this issue, the test system was analyzed as a spring-mass model as shown in Fig. 2.8. M is the mass of the moving parts composed primarily of the mass of the shaft; k_a is the stiffness of the actuator (25×10^6 N/m); and k_s is the stiffness of the preload spring (25×10^3 N/m). Since the springs k_a and k_s are mechanically connected in parallel, the natural frequency f_n of the system is given by,

$$f_n = \frac{1}{2\pi} \sqrt{\frac{(k_a + k_s)}{M}} \quad (2.1)$$

Solutions for increasing the natural frequency of the system were first explored so that the resonance effects could be minimized. The value of k_a for an actuator is fixed and an increase in the value of k_s is not recommended as it would reduce the stroke that can be produced in the actuator at a particular applied voltage. Upon contacting *Nippon Bearing®*, the manufacturer of the shaft used in the test rig, it was learnt that a change in the shaft material (*with less mass density*) was not possible and drilling a bore in the solid shaft (*to reduce its mass*) within specified dimensions does not improve the natural frequency significantly. Therefore, the options of increasing the stiffness and/or reducing the mass of the system were both ruled out. Instead, a half-trapezoidal signal with 25% duty cycle was utilized during the Rise Time Testing. The duty cycle helped in damping out the vibrations between successive signals and the use of ‘half’ signal helped in reducing the error involved in stroke measurements.

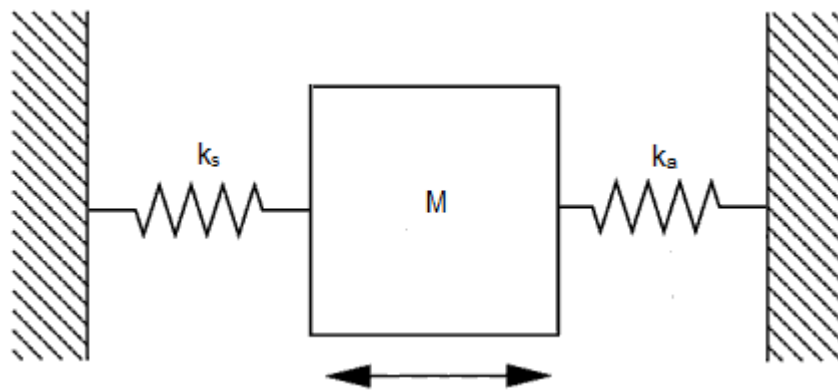


Figure 2.8 Spring-mass model of test system

- iii. The original groove in the test rig was designed for actuators with circular cross-sections. In order to accommodate the PI-885.91 actuators, having a rectangular cross-section, a new groove had to be machined with appropriate dimensions.
- iv. In-house programs were developed in *LabView®* software to run the experiments and record the results. Due to the wide variety of tests and parameters, the program development involved a significant amount of effort.

- v. *National Instruments*® data acquisition card *DAQCard-6062E* was originally used for recording the input data from the sensors and controlling the output signals from the power amplifier. This card got damaged during the later stages of testing. *NI USB-6009* data acquisition card had to be used in its place to complete the remaining tests. The *NI USB-6009* had a much lower input sampling rate of 48 kS/s compared to 500 kS/s of the *DAQCard-6062E*. This necessitated modifications in majority of the *LabView*® programs that were written to control the tests. The *NI USB-6009* also had lower unipolar output range of 0 to +5V (*insufficient for running the complete set of tests*) compared to the bipolar $\pm 10V$ range of the *DAQCard-6062E*. An *Agilent*® signal generator was, therefore, used to provide the required full-range, bipolar output voltage. The use of signal generator, however, introduced a manual step into an otherwise automated operation. Finally, by taking these necessary actions, all the planned tests were completed.
- vi. As few of the experimental facilities had to be shared with other groups, the scheduling of experiments required some extra consideration. The Materials Engineering group at UBC was conducting a parallel study in which actuators had to be exposed inside the hydrogen-safe chamber, located at CERC, which could simultaneously accommodate a maximum of three actuators. The thermal chamber, at Westport Innovations Inc., had to be vacated on an ad hoc basis when their industrial projects demanded its use.

2.2. Experimental Results and Discussion

In order to verify the effects of hydrogen on actuator performance, the base results for unexposed actuators were determined first. These base results were then compared to the results for actuators exposed to hydrogen under various exposure cycles described in Sec.2.1.1. The differences observed, if any, were attributed to the interaction of the actuators with hydrogen. A comparison of the performance of PI Ceramic actuators used in the present work was also made with that of the KCl actuators used by Li *et al* [2] and Senousy *et al* [3] during previous studies. The detailed results are presented in the subsequent sections.

2.2.1. Performance of Unexposed Actuators

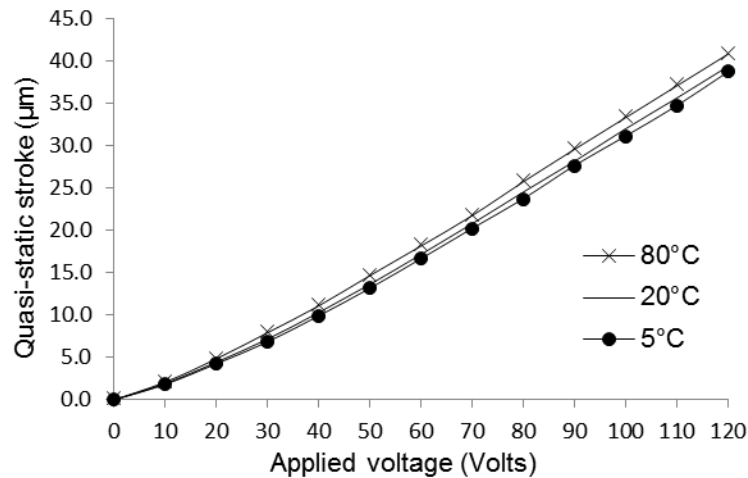


Figure 2.9 Quasi-static stroke-voltage relationship of unexposed actuator for different ambient temperatures

Fig. 2.9 shows the dependence of quasi-static stroke of an unexposed actuator on the driving voltage over a temperature range 5-80°C. The stroke-voltage relationship is slightly non-linear with the slope increasing with applied voltage. The slope is representative of the longitudinal piezoelectric strain coefficient d_{33} of the actuator material. It is therefore evident that d_{33} increases with driving voltage, and its value at the maximum voltage used in this study (120V) is about 1.7 times the value corresponding to the initial linear regime of 0-20 V. This observation is in close agreement with the results obtained by Li *et al* [2] and is attributed to the presence of non-linear effects such as non-180° domain switching at higher driving voltages. The effect of temperature on

the quasi-static stroke is minor with the stroke increasing slightly with ambient temperature [Fig. 2.10].

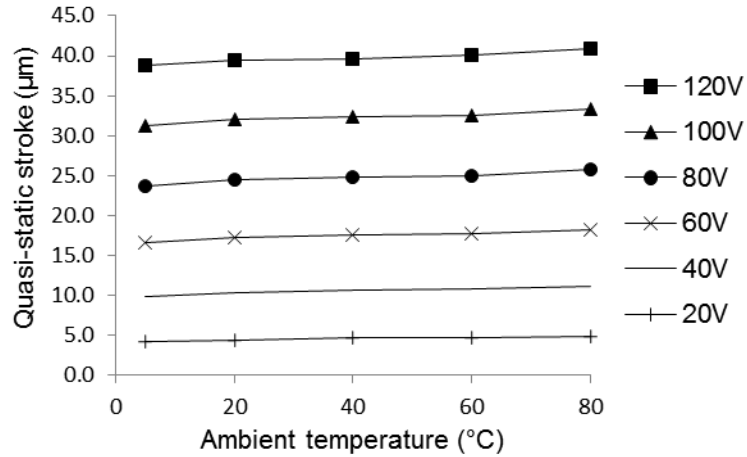


Figure 2.10 *Quasi-static stroke-temperature relationship of unexposed actuator for different applied voltages.*

During the experiments, the actuators were allowed a sufficient time to expand/contract due to the variations in ambient temperature. The electric voltage was then applied to them and the resulting stroke was measured. This experimentally measured stroke, therefore, did not include any contributions due to thermal strain. Also, the applied preload stresses were too small to produce any measurable mechanical strain. Therefore, it can be safely assumed that the actuator stroke measured during the experiments was only due to the piezoelectric effect. For fuel injector applications, the longitudinal piezoelectric strain coefficient d_{33} is the property responsible for this stroke and any variation in its value during the operation can seriously affect the reliability of the system. d_{33} can be computed from the experimental results using the following relation:

$$d_{33} = \frac{\text{Measured stroke}}{\text{Number of actuator layers} * \text{Applied voltage}} \quad (2.2)$$

The variation of d_{33} with applied voltage is depicted in Fig. 2.11. d_{33} is found to be constant up to 20 Volts beyond which its value starts increasing with the applied voltage. Based on this relationship, an actuator gives a linear response to an applied voltage for up to 20 Volts and a non-linear response at voltages greater than 20 Volts. The computed value of d_{33} at room temperature (20°C) and low driving voltages (≤ 20 Volts)

is about 3.70×10^{-10} m/V which is very close to the vendor-specified data of 3.94×10^{-10} m/V. Even in the linear region, the value of d_{33} increases by about 15% when the ambient temperature rose from 5°C to 80°C indicating a functional dependence of d_{33} on temperature. This dependence is found to be linear according to the plot presented in Fig. 2.12.

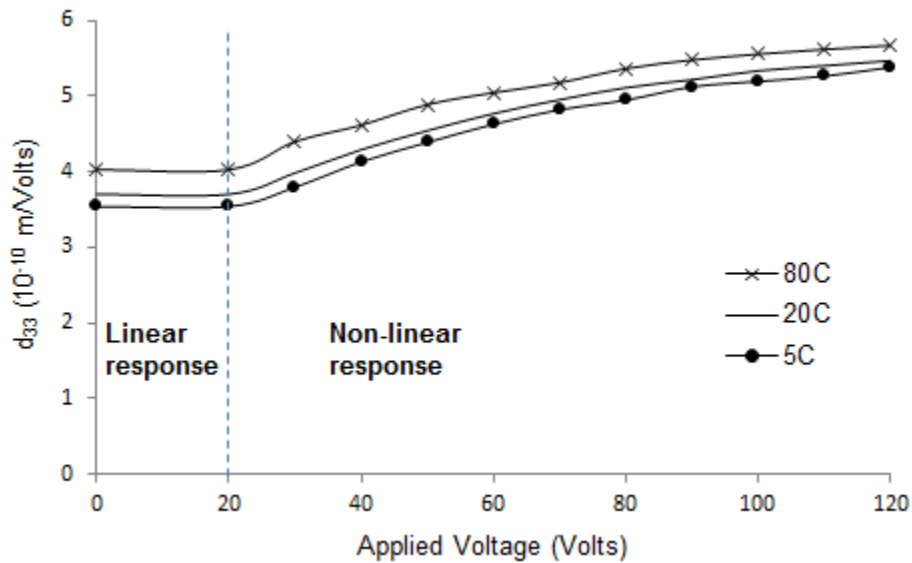


Figure 2.11 Variation of d_{33} with applied quasi-static voltage at different ambient temperatures for an unexposed actuator.

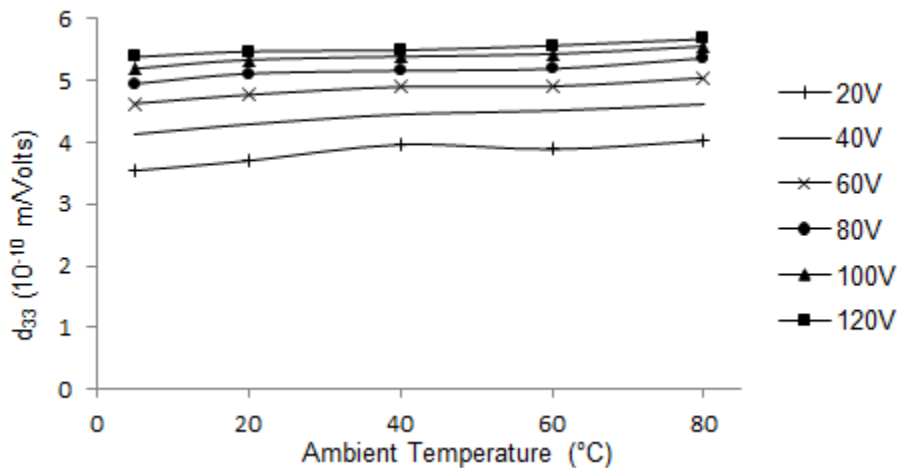


Figure 2.12 Variation of d_{33} with ambient temperature at different applied quasi-static voltages for an unexposed actuator.

In a piezoelectric material, the values of the material properties (*including* d_{33}) are a result of both intrinsic and extrinsic contributions. The intrinsic properties are material properties from a single-domain material, while the extrinsic properties are mainly from domain walls. According to Zhang *et al* [15,50], at low applied voltages, the extrinsic contributions to d_{33} are only due to temperature variations. This explains the behaviour observed in the ‘Linear response’ section of Fig. 2.11 where we observe an increase in the d_{33} value with temperature but not with applied voltage. At higher applied voltages, however, an additional extrinsic part is introduced to account for the increased activities of non-180° domain walls. The trend observed in Fig. 2.11 and Fig. 2.12 is in good agreement with the results obtained by Senousy *et al* [3] for the KCl actuators.

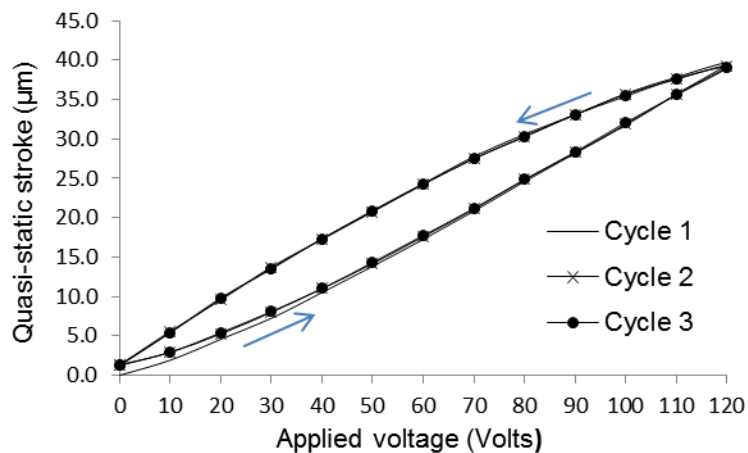


Figure 2.13 Quasi-static piezoelectric hysteresis of unexposed actuator at 20°C

Fig. 2.13 shows the quasi-static stroke during three consecutive electrical loading-unloading cycles at 20°C. Piezoelectric hysteresis is found to be present during all the cycles which causes self-heat generation in the actuator during a dynamic operation. It is also observed that a zero point drift exists between the beginnings of loading cycle 1 and 2 but disappears during the subsequent cycles.

During practical situations, actuators are driven at a certain frequency. The effect of frequency on the actuator stroke under sinusoidal AC driving voltages is shown in Fig. 2.14. It is observed that up to 100 Hz, there is a minor reduction in the measured stroke. This can be attributed to a lower relaxation frequency (or higher reorientation time) of a certain percentage of dipoles in the PZT material [11]. As these dipoles are unable to reorient themselves at the increased driving frequencies due to insufficient time available

to reorient, they do not contribute to the piezoelectric effect. The increasing trend in stroke for the frequencies above 100 Hz is mainly due to resonance. The resonance frequency of the test system is near 500 Hz.

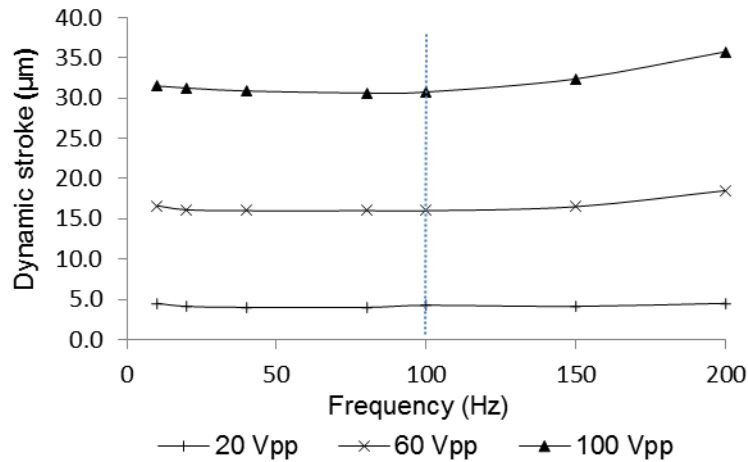


Figure 2.14 Effect of sinusoidal driving signal frequency on dynamic stroke of unexposed actuator for different driving voltages at 20°C

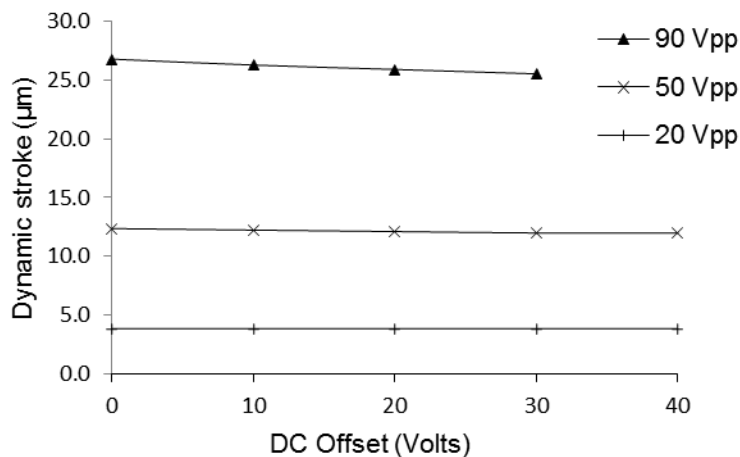


Figure 2.15 Effect of positive DC offset on dynamic stroke of unexposed actuator for different applied voltages at 20°C

As already explained in Sec. 2.1.2., a limit on the maximum allowable negative voltage necessitates the use of a DC offset during AC electrical loadings. For a particular applied peak-to-peak voltage, the amount of DC offset used may affect the actuator stroke obtained at that voltage. This is shown in Fig. 2.15 for a 100 Hz sinusoidal AC driving signal. At lower applied voltages (20-50 V_{pp}), the DC offset has negligible effect on the stroke. At higher applied voltages (90 V_{pp}), however, the DC offset causes the

stroke to decrease slightly. According to Masys *et al* [12], a positive DC offset results in the pinning of domain walls. This pinning reduces the extrinsic contribution to the piezoelectric response. As the extrinsic contribution is more at higher applied voltages [2], the effect of pinning caused by DC offset is also more evident at higher applied voltages.

The effect of duty cycle percentage on the dynamic stroke was investigated for a 100 Hz sinusoidal AC driving signal at different applied voltages and the results are presented in Fig. 2.16. Within the tested parameters, the duty cycle is found to have no effect on the actuator stroke. This observation agrees well with the results obtained by Senousy *et al* [3]. Unless otherwise stated, the duty cycle is 100% for all the dynamic test results presented in this chapter.

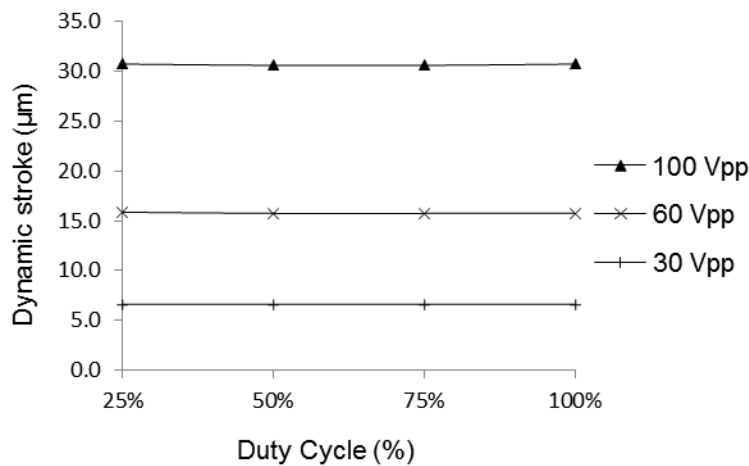


Figure 2.16 Effect of duty cycle percentage on dynamic stroke of unexposed actuator for different applied voltages at 20°C

Fig. 2.17 shows the effect of rise time percentage on the dynamic stroke of the actuator during a trapezoidal driving signal. For the reasons stated in Sec. 2.1.2., these tests were conducted by applying a half-trapezoidal signal with a 25% duty cycle. A lower rise time percentage provides a longer holding time at the maximum voltage. According to Sherrit *et al* [13], more non-180° domain walls can contribute to the piezoelectric response during longer holding times. Thus, an increase in stroke is observed at lower rise time percentages for both 50 Hz and 100 Hz trapezoidal signals. Additionally, at the lower rise time percentages, the measured response is also

superimposed by the vibrations produced due to the inertia of moving parts as explained in Sec. 2.1.2.

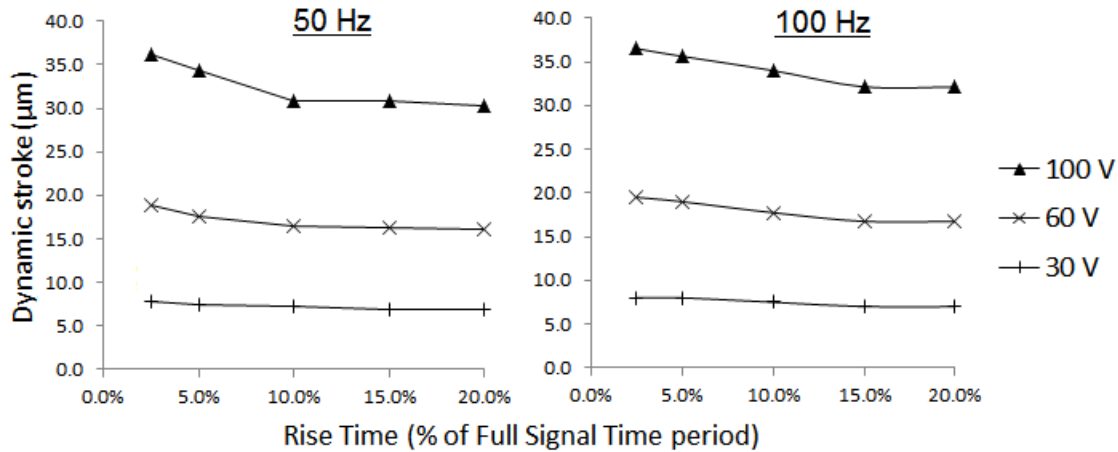


Figure 2.17 Effect of rise time percentage on dynamic stroke of unexposed actuator for different applied voltages at 20°C

2.2.2. Self-heating in Unexposed Actuators

During a continuous operation, self-heating can take place inside the actuator material due to losses, such as piezoelectric and dielectric hysteresis [14]. The rate of self-heating can be significant when the actuators are driven under high voltages and/or high frequencies [3]. This self-heating, during the dynamic operation, causes the temperature of the actuator material to rise which can affect the reliability and material properties of these actuators, and may also limit their application.

To investigate the self-heating behavior of actuators used in the current study, the actuators were driven continuously for 10 minutes under continuous sinusoidal electric loading cycles at various frequencies (100-200 Hz) and applied voltages (30-120 V_{pp}). The ambient temperature inside the thermal chamber was maintained such that the actuator surface was at approx. 20°C before the start of each test. ΔT represents the rise in actuator surface temperature during the test from its initial value.

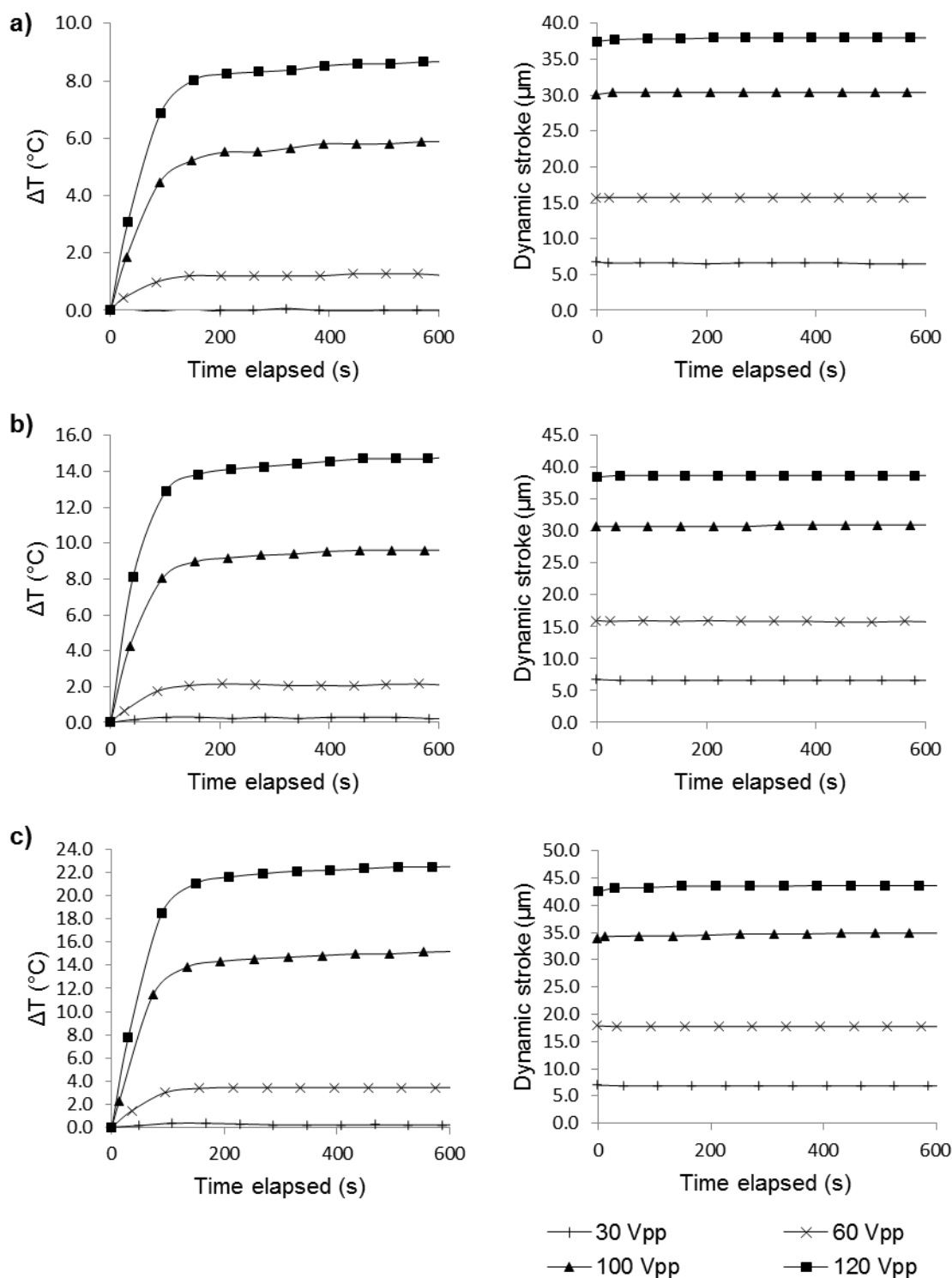


Figure 2.18 Temperature rise and dynamic stroke during continuous sinusoidal electric loading under different applied voltages at frequencies; a) 100 Hz; b) 150 Hz; and c) 200 Hz

It can be seen from Fig. 2.18 that the actuator temperature shows an initial increasing trend with time and later reaches a steady-state value. The steady-state temperature is found to increase with increasing applied voltage and frequency. During the tests, the actuator stroke was also measured and is plotted adjacent to the temperature plots in Fig. 2.18. As no measurable variation is seen in the dynamic stroke, it can be concluded that the temperature increase, due to self-heating, does not result in any performance changes when the actuator is operated at frequencies up to 200 Hz. This behaviour is consistent with the ambient temperature effects presented in Fig. 2.10. It should be noted that the dynamic stroke represents the peak-to-peak sinusoidal response of an actuator to a sinusoidal electric driving signal. Any thermal strain, due to actuator temperature rise, will only result in shifting the center line of this response and will not affect the peak-to-peak stroke value discussed here. In other words, the measured dynamic stroke was uncoupled from the thermal strain effects during measurements.

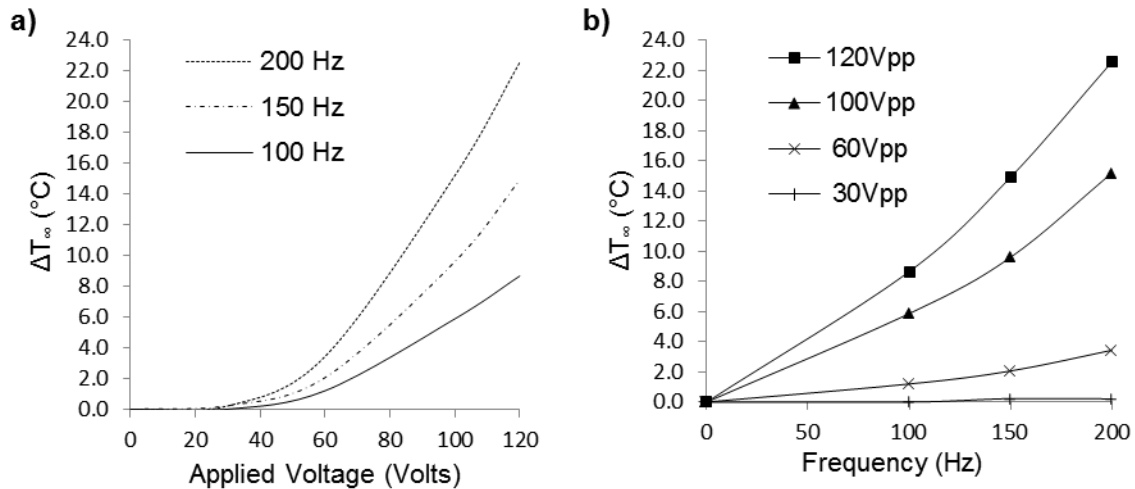


Figure 2.19 Variation of steady-state temperature with; a) applied voltage; and b) frequency

The variation of steady-state temperature (ΔT_{∞}) with applied voltage is shown in Fig. 2.19(a) for different frequencies. A non-linear relationship is observed for the variation. The non-linearity also seems to increase with increasing frequencies. A similar trend is seen for the variation of steady-state temperature with frequency at different applied voltages [Fig. 2.19(b)]. These results confirm that the driving signal voltage and

frequency are important parameters affecting the thermal behaviour of PI actuators during a dynamic operation.

Senousy *et al* [47] developed an analytical model to explain the self-heating behaviour of piezoelectric stack actuators. This model is based on the first law of thermodynamics and takes into account different parameters, such as actuator geometry, magnitude and frequency of the applied electrical signal, duty cycle and ambient conditions. The actuator temperature increase with time is expressed in a classical exponential closed-form by the model. *Displacement hysteresis* D_f is represented by the hysteresis area [Fig. 2.13] and defined as the energy loss of the sample per electric charge per driving cycle. At an applied voltage of 120 V, D_f is found to have a value of 10.78 J/C/cycle. If D_f is assumed to remain constant during the actuator operation, the steady-state temperature rise ΔT_∞ experienced by the actuator is expressed by the model [47] as follows:

$$\Delta T_\infty = \frac{d_t C V D_f f}{\bar{h} A_1} \quad (2.3)$$

Where,

d_t = Duty cycle percentage

C = Capacitance of the actuator

V = Applied voltage magnitude

f = Applied voltage frequency

\bar{h} = Overall heat convection coefficient

A_1 = Actuator's surface area exposed to the ambient air

The aluminum bracket, in which the actuator is placed when loaded on a test rig, also acts as a heat sink providing an overall heat convection coefficient of 84.3 W/m². Fig. 2.20 compares the theoretical steady-state temperatures obtained using Eq. 2.3 with those observed during the experiments under an applied sinusoidal signal of 120 V_{pp} at 100% duty cycle. The slight difference observed in the results may be attributed to the fact that in Eq. 2.3, the heat escaping from the two ends of the actuator is not considered. Moreover, the contact of the actuator with aluminium and steel at these ends should further increase the value of \bar{h} in Eq. 2.3, thereby resulting in a decreased theoretical temperature value.

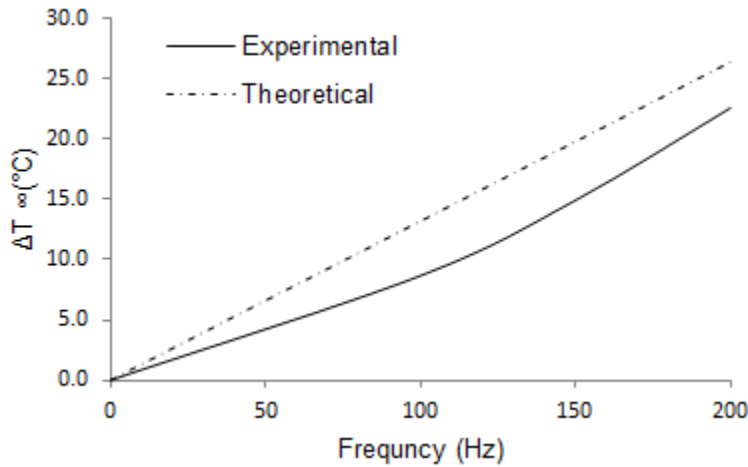


Figure 2.20 Comparison of experimental and theoretical steady-state temperature rise for a continuous 120 V_{pp} sinusoidal signal at 20°C

2.2.3. Comparison of PI and KCI Actuators

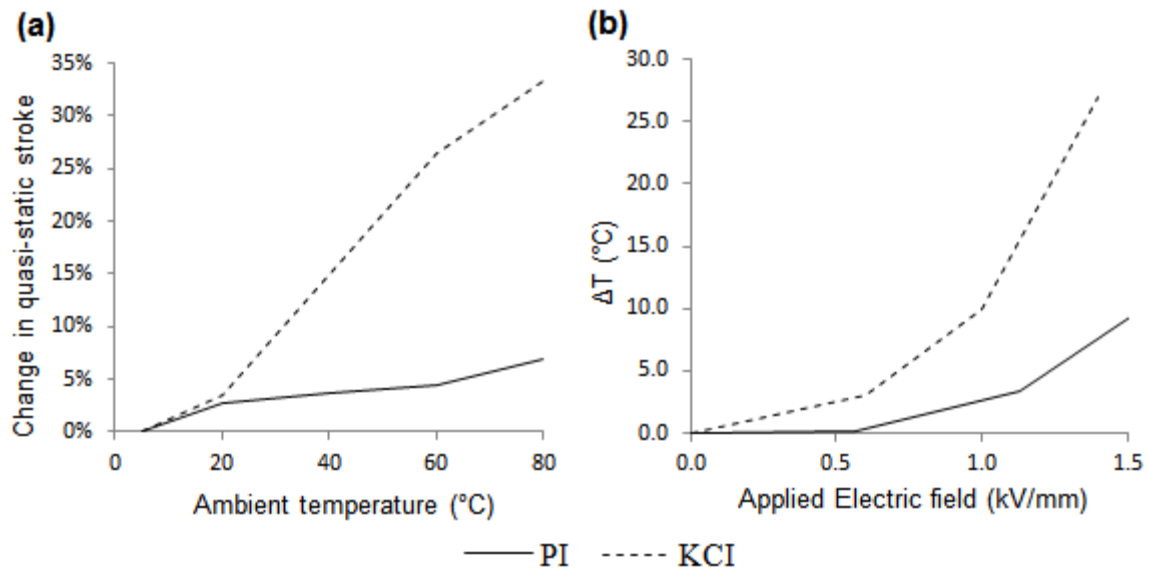


Figure 2.21 Comparative thermal performance of PI and KCI actuators; (a) temperature dependence of quasi-static stroke at 1.8 kV/mm applied electric field; and (b) temperature increase due to self-heating under 200 Hz sinusoidal dynamic excitation

The temperature dependency of the quasi-static stroke of the PI actuators, used in the present study, is compared with the KCI actuators, used by Li *et al* [2], in Fig. 2.21(a). It is observed that under an applied electric field of 1.8 kV/mm, the effect of temperature on the quasi-static stroke of PI actuators is less than 7% over the selected

temperature range (5-80°C). Under similar conditions, however, the KCl actuators showed a variation of up to 35%. Additionally, during dynamic electric loading, the temperature rise (ΔT) due to self-heating in the PI actuators is about 4 times less than the KCl actuators used by Senousy *et al* [3] [Fig. 2.21(b)]. This means that in comparison to the KCl actuators, the PI actuators not only generate less heat but also the temperature rise occurring in the actuator, due to the generated heat, produces a significantly lesser variation in performance. This indicates that the PI actuators are more thermally stable and, therefore, can provide a better control of the fuel injector under the expected operating conditions.

2.2.4. Performance of Actuators after Continuous and Cyclic Hydrogen Exposure

The exposure of actuators to hydrogen was carried out under the conditions and as per the approaches mentioned in Sec. 2.1.1. Performance of these exposed actuators was then experimentally assessed under both quasi-static and dynamic electrical loading conditions. This section presents the effects of continuous and cyclic hydrogen exposure approaches on the actuator performance.

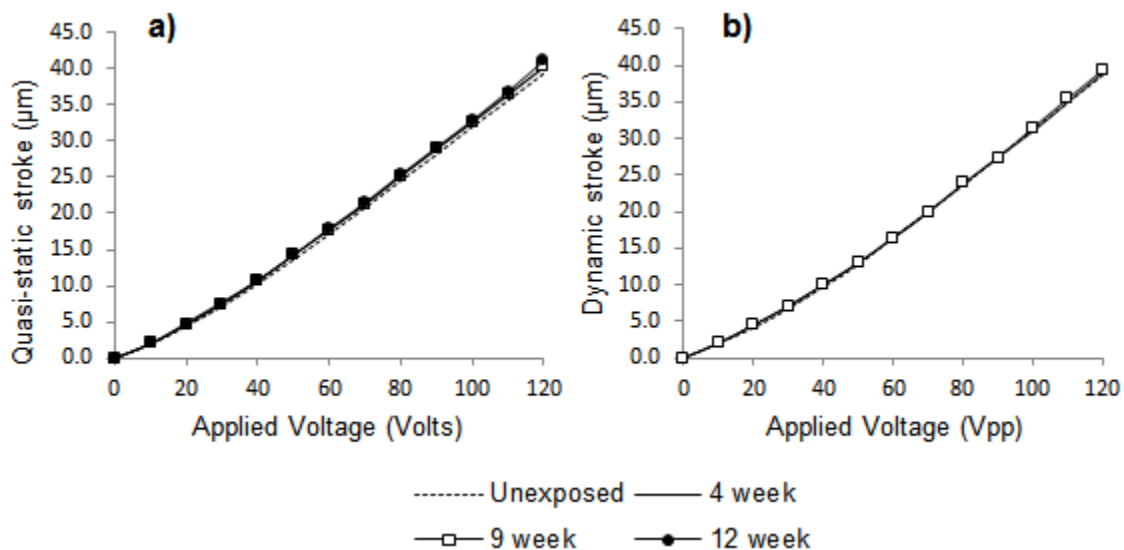


Figure 2.22 Effect of continuous hydrogen exposure on actuator stroke at 20°C under; a) quasi-static; and b) 100 Hz sinusoidal dynamic electrical loading

Fig. 2.22(a) shows the effect of up to 12 weeks of continuous hydrogen exposure on the quasi-static actuator stroke measured at 20°C. Negligible variation in the stroke is observed due to this continuous exposure. Similar results were obtained for additional quasi-static tests conducted at 5°C, 40°C, 60°C and 80°C (*Not shown here*) which confirms that the observed invariance of stroke with continuous hydrogen exposure is true for the entire temperature range expected in a fuel injector. The result of dynamic testing conducted at 100Hz also indicates a similar behaviour [Fig. 2.22(b)].

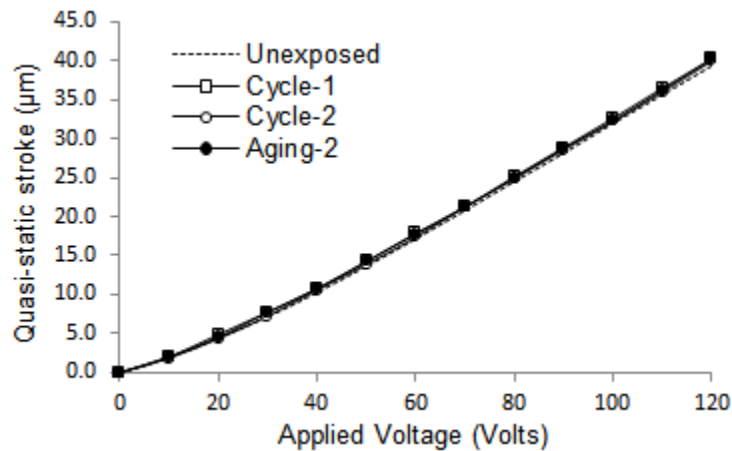


Figure 2.23 Effect of cyclic hydrogen exposure on quasi-static stroke at 20°C

In a practical situation, a piezoelectric actuator used in a hydrogen-based fuel injector could be subjected to multiple hydrogen exposure cycles of shorter durations. It has also been confirmed experimentally that hydrogen atoms are able to escape from PZT samples during aging at room temperature [5]. This condition can practically occur when the engine is turned off after operation. The diffusion pattern of hydrogen in PZT during such cyclic conditions and its consequential effect on the actuator performance can possibly be different from a continuous exposure. To investigate this, a cyclic exposure approach was followed in which an actuator sample set was exposed to hydrogen for multiple 4 week cycles with a 4 week aging period between two consecutive cycles [Sec 2.2.1]. Quasi-static performance at 20°C is shown for the cycled samples in Fig. 2.23. It is observed that the cyclic hydrogen exposure and subsequent aging have a negligible effect on the quasi-static actuator stroke. The behaviour was similar at other testing temperatures as well. Dynamic testing was not performed for this case.

2.2.5. Explanation for Negligible Hydrogen Effects on Actuator Performance

It is evident from the results presented in the previous section that the exposure of actuators, either continuous or cyclic, to hydrogen has a negligible effect on their performance. This behaviour exhibited by the PI actuators after exposure to hydrogen is very different from the limited experimental results reported in literature for piezoelectric thin disks interacting with hydrogen. Wu *et al* [5] showed that d_{33} of PZT varies significantly with the concentration of hydrogen in it. According to their results, charging of thin PZT disks (25mm x 25mm x 1mm) having Ag electrodes with H₂ gas at 100°C temperature and 0.1 MPa pressure increases their d_{33} by more than 15% within 20 hrs. It should be noted that in a fuel injector, the stroke of an actuator is primarily controlled by the value of d_{33} . Therefore, its variation should accordingly affect the measured stroke. Under more severe hydrogen exposure conditions (100°C , 10 MPa), similar to those employed in the current work, Shafiei *et al* [8] conducted a microstructure investigation of thin PZT disks (10mm x 10mm x 1mm) with Ag and Ag/Pd electrodes. They reported the formation of a corroded layer inside the PZT disks and delamination of electrodes within 2-3 weeks of continuous exposure. The formation of corroded layer produces heterogeneity in the material of the disk. According to Shafiei *et al* [10], this heterogeneity alters the electrical capacitance of the disk under dynamic electrical loading conditions. It is well known that d_{33} is proportional to the electrical capacitance [2]. Therefore, it is expected that this variation in dynamic capacitance, initiated by hydrogen exposure, should also affect the dynamic stroke of the actuator. None of these effects were, however, observed in the hydrogen exposed PI actuators.

A possible explanation for this unusual behaviour of PI actuators can be found in the mechanism governing diffusion of hydrogen into the PZT material. The results reported by Wu *et al* [5] and Shafiei *et al* [8,9,10] are based on experiments conducted on the bulk PZT material. Fig. 2.24(a) shows a typical sample used during these bulk studies. The sample consists of a thin PZT disk sandwiched between metallic electrodes. During exposure, molecular hydrogen H₂ attacks the sample from all directions (top, bottom and 4 sides). According to Shafiei *et al* [8], H₂ gas molecules dissociate into H-atoms at the surface of the metallic electrodes [Fig. 2.24(b)]. It is these H-atoms (not H₂ molecules) which diffuse into the adjacent PZT disk. This diffusion of H-

atoms can take place, (1) *Laterally* by ‘spill over’ action from the sides at the PZT-electrode interface; and (2) *Longitudinally* from the top (and bottom) into the PZT region adjacent to the electrode.

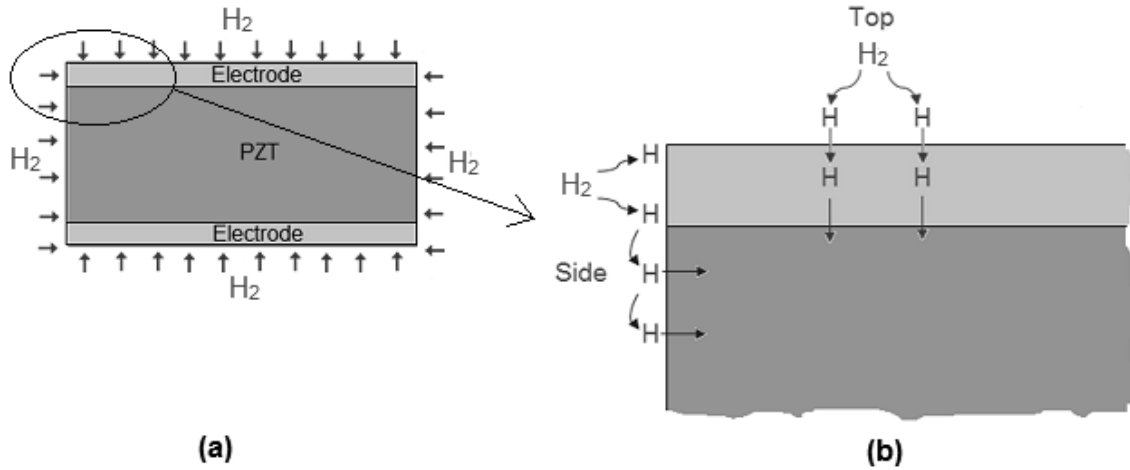


Figure 2.24 a) Cross-section of a typical bulk study sample under hydrogen exposure; and b) mechanism governing diffusion of hydrogen into PZT sample

Some of the structural features of the PI actuators utilized during the present study are different from the bulk study samples. These ‘stack-type’ actuators consist of several thin disks of piezoelectric material sandwiched between alternate positive and negative electrodes. Due to the stacked nature, molecular hydrogen H₂ cannot attack a single PZT layer within the actuator from the top and bottom directions (except for the end layers). As there is no molecular hydrogen H₂, there is no possibility of the formation of H-atoms and consequently no *longitudinal* diffusion. Additionally, a 50 μm thick protective ceramic insulation is provided on the lateral surface of PI actuators. This insulation cuts-off any direct contact between the metallic electrode and the molecular hydrogen H₂ attacking from the sides. This may cause the rate of formation of H-atoms at the electrodes and their consequential *lateral* diffusion into the PZT layer to slow down considerably. Therefore, it may be concluded that the mechanism responsible for the diffusion of hydrogen into the PZT material, which was active during the bulk studies, is not active during the present study conducted on the PI actuators [Fig. 2.25]. As a result, the concentration of hydrogen in the PZT layers of the PI actuator is unable to reach

such values that can measurably affect their d_{33} as per [5]. Therefore, the negligible variation observed in the PI actuator stroke even after significant hydrogen exposure is attributed mainly to their stacked nature and the presence of protective ceramic insulation.

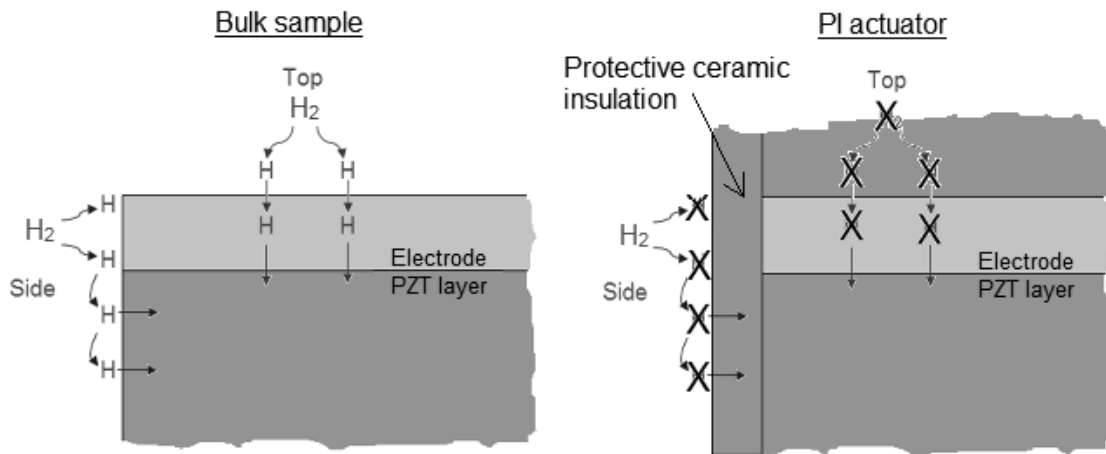


Figure 2.25 Comparison of hydrogen diffusion mechanism in bulk sample and PI actuator

2.2.6. Performance of Fatigue Cycled - Hydrogen Exposed Actuators

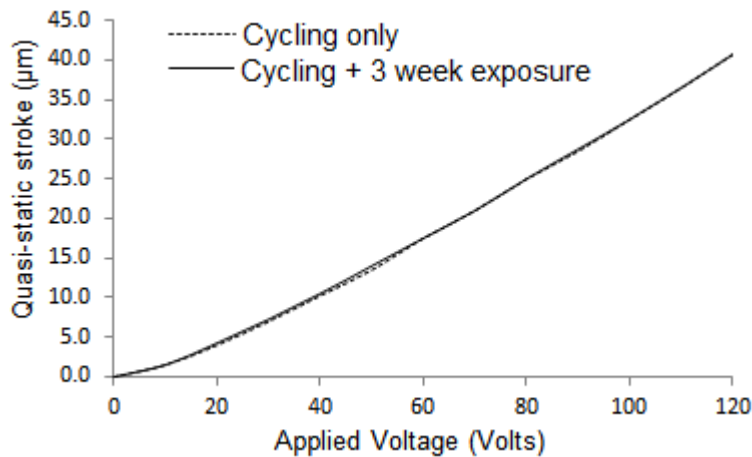


Figure 2.26 Hydrogen exposure effects on the quasi-static performance of cycled actuator at 20°C

During a fuel injector's continuous operation, a piezoelectric actuator is subjected to cyclic electrical loading conditions. This may result in the development of fatigue-

induced cracks/openings in the PI actuator's protective ceramic insulation bringing the surrounding H_2 molecules in contact with the metallic electrode. This can potentially result in the *lateral* diffusion of H-atoms as explained in the previous section. In order to experimentally investigate the actuator performance in such a scenario, the PI actuators were first cycled with a $100 V_{pp}$, 100 Hz sinusoidal electrical signal for 1.8×10^8 cycles. The choice for the number of cycles was made in accordance with a study conducted by Wang *et al* [4]. The cycled actuators were then *continuously* exposed for 3 weeks to hydrogen at $100^\circ C$ temperature and 10 MPa pressure. Quasi-static performance of the actuators immediately after cycling and after their subsequent hydrogen exposure is compared in Fig. 2.26. It is observed that up to 3 weeks of continuous hydrogen exposure does not affect the stroke of the cycled actuators. This observation further substantiates the reliability of PI actuators in hydrogen-based fuel injector applications which involve cyclic electrical loadings.

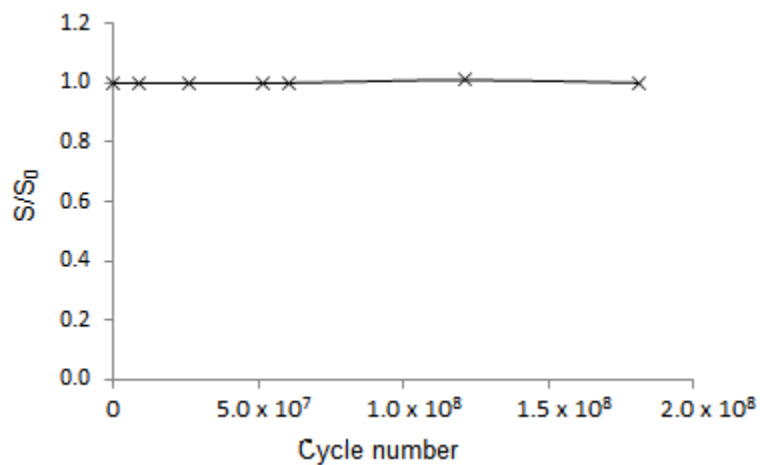


Figure 2.27 Normalized dynamic stroke of PI actuators during fatigue cycling

This study also provided some insight into the electrical fatigue response of PI actuators. The dynamic stroke of the actuators was constantly monitored during the fatigue cycling done with a continuous $100 V_{pp}$, 100 Hz sinusoidal signal. Fig. 2.27 shows the variation of normalized dynamic stroke (S/S_0 , where S_0 is the pre-fatigue value) with cycling. It is found that the dynamic stroke remains consistent during the fatigue cycling for up to 1.8×10^8 cycles. This fatigue response of the PI actuators to cyclic electrical loading is a significant improvement upon that of the Noliac® actuators studied by Wang *et al* [4]. During their study, Wang *et al* [4] started observing a

decrease in the actuator stroke as early as 10^6 cycles and more than 40% reduction had taken place by the completion of 10^8 cycles.

2.2.7. Microstructure and Dielectric Investigation

The microstructure investigation of the tested actuators was performed by a Hitachi S 3000-N Scanning Electron Microscope (SEM) using an Electron Dispersive X-ray Spectroscopy (EDS) detector and Quartz X-One X-ray post-processing software. The SEM/EDS investigations were performed in a low vacuum – variable pressure mode, using the Back Scattered Electron method, which offers good contrast and allows the study of non-conducting specimen without applying any conductive coating to avoid charging [8]. Micrographs of the lateral surface of new PI actuators and after their 12 week exposure to hydrogen (100°C , 10 MPa) are shown in Fig. 2.28. The lateral surface is the surface of protective ceramic insulation present on the actuators. No noticeable structural changes are observed in the micrographs due to the hydrogen exposure. This agrees well with the observations made by Shafiei *et al* [8] for bare (without electrodes) PZT plates exposed to a similar hydrogen atmosphere for 7 weeks. This also confirms the explanation provided in Sec. 2.2.5 regarding the inactiveness of hydrogen diffusion mechanism in the PI actuators.

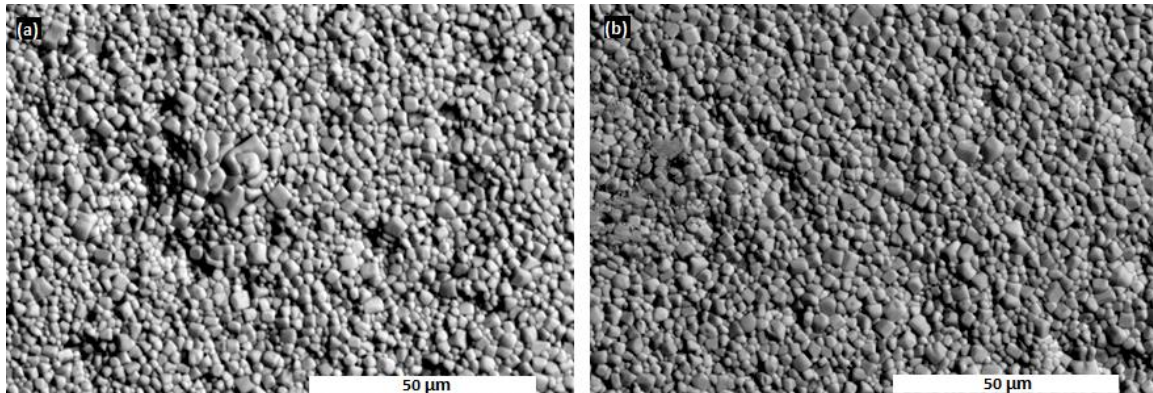


Figure 2.28 Micrographs of lateral surface of; (a) new PI actuators; and (b) after their 12 week hydrogen (100°C , 10 MPa) exposure

Theoretically, the intrinsic piezoelectric response of a piezoelectric material is proportional to its intrinsic dielectric response [15]. This implies that a negligible variation observed in the actuator stroke upon hydrogen exposure should also result in a negligible variation in the actuator capacitance. This was investigated at 20°C , with a

1.275 Volt and 100 Hz signal, using a high-resolution impedance analyser LCR817 (*Instek*[®]). It was found that a continuous hydrogen exposure of up to 12 weeks does not produce any measurable variation in the capacitance (or the dielectric constant ϵ_{33}). This result theoretically validates the behaviour observed in the PI actuators.

2.3. Summary of Experimental Results

Quasi-static and dynamic thermo-electro-mechanical performance of PI 885.91 soft, PZT-based stack actuators under different operating conditions, relevant to a typical Hydrogen-based fuel injector, was experimentally investigated in this chapter. The relationship between the observed actuator stroke and applied voltage, frequency, DC-offset, duty cycle and rise time followed a similar trend as reported previously by Li *et al* [2] and Senousy *et al* [3] for the studies conducted on KCl actuators. However, in comparison to the KCl actuators, the PI actuators used in the present study showed a better thermal stability, lower heat generation and smaller hysteresis. The results obtained from the self-heating tests revealed that the temperature rise due to self-heating increased non-linearly with both driving voltage and frequency, which also is consistent with the findings of Senousy *et al* [3]. The actuators were exposed to hydrogen at 100°C temperature and 10 MPa pressure following; (a) *Continuous approach* - for up to 12 weeks; and (b) *Cyclic approach* - for multiple 4 week exposure cycles with a 4 week aging period between two consecutive cycles. Both these exposure approaches had a negligible effect on the quasi-static and dynamic performance of the PI actuators when tested within the temperature range 5-80°C. This behaviour was attributed mainly to the presence of a protective ceramic insulation layer on the lateral surface of the PI actuators which deactivated the mechanism responsible for hydrogen diffusion into the PZT layers, thereby preventing any consequential variation in the actuator performance. This was further confirmed by microstructure and dielectric investigations that showed negligible microstructure and capacitance variations respectively in the actuators after 12 weeks of continuous hydrogen exposure. Finally, fatigue cycling of the actuators was carried out to potentially introduce any cracks/openings in the ceramic insulation which may activate the hydrogen diffusion mechanism. After a fatigue cycling of 1.8×10^8 cycles with a 100 V_{pp}, 100 Hz sinusoidal electrical signal followed by a 3 week hydrogen exposure, the performance of the PI

actuators was still unaltered. The electrical fatigue response of the PI actuators also remained consistent during the entire cycling which is a significant improvement upon previously reported results for the Noliac® actuators [4].

3. Numerical Modelling

3.1. Linear Thermo-Electro-Mechanical Material Behaviour

In a 3-dimensional Cartesian co-ordinate system, the governing equations for thermo-electro-mechanical response of a piezoelectric material are given by [38],

$$\sigma_{ij,j} + b_i = \rho \ddot{u}_i \quad (3.1a)$$

$$D_{i,i} - \varphi_e = 0 \quad (3.1b)$$

$$q_{i,i} + T_{ref} \dot{S} = \varphi_t \quad (3.1c)$$

i, j = x, y, z directions

Where,

u_i = Mechanical displacement vector

D_i = Electric displacement vector

q_i = Heat flux vector

σ_{ij} = Mechanical stress tensor

b_i = Mechanical body force vector

φ_e = Electric body charge density

φ_t = Heat source density

S = Entropy density

T_{ref} = Reference temperature of the material equal to 20°C

ρ = Mass density of the material

In the above equation set, Eqs.3.1 (a-c) represents mechanical, electrical and thermal equilibria respectively.

The coupling between mechanical, electrical and thermal domains within the piezoelectric material is mathematically represented using the following constitutive relations [38]:

$$\sigma_{ij} = c_{ijkl} \epsilon_{kl} - e_{kij} E_k - \lambda_{ij} T \quad (3.2a)$$

$$D_i = e_{ikl} \epsilon_{kl} + \varepsilon_{ik} E_k + p_i T \quad (3.2b)$$

$$S = \lambda_{kl} \epsilon_{kl} + p_k E_k + \alpha_v T \quad (3.2c)$$

$i, j, k, l = x, y, z$ directions

Where,

ϵ_{kl} = Mechanical strain tensor

E_k = Electric field vector

T = Temperature rise from the stress-free state

c_{ijkl} = Elastic stiffness coefficient

ε_{ik} = Absolute dielectric permittivity coefficient

α_v = A material constant dependent on density (ρ), specific heat at constant volume (C_v) and reference temperature (T_{ref}) of the material; $\alpha_v = \frac{\rho C_v}{T_{ref}}$

e_{ikl} = Piezoelectric stress coefficient

λ_{ij} = Thermal stress coefficient

p_i = Pyroelectric coefficient

The mechanical stress tensor σ_{ij} , electric displacement vector D_i and entropy density S are replaced in the governing equations [Eq. 3.1] using the constitutive relations [Eq. 3.2]. The mechanical strain tensor ϵ_{kl} , electric field vector E_k and heat flux vector q_i are further converted into the most fundamental state variables (mechanical displacement vector u_i , electric voltage V and temperature rise from the stress-free state T) using the following basic relations:

$$\epsilon_{ij} = \frac{1}{2} [u_{i,j} + u_{j,i}] \quad (3.3a)$$

$$E_i = -V_{,i} \quad (3.3b)$$

$$q_i = -\kappa_{ij} T_{,j} \quad (3.3c)$$

$i, j = x, y, z$ directions

Where,

κ_{ij} = Thermal conductivity coefficient

Finally, a set of partial differential equations expressed in terms of the most fundamental state variables (u_i, V and T) are obtained. This set of equations is then required to be solved for the variables u_i, V and T at every point in the continuum at all times.

In order to obtain the solution for the partial differential equations, both initial conditions and boundary conditions for a given problem need to be specified. On a boundary Π , the admissible boundary condition equations can be expressed in the following forms:

$$\text{Mechanical:} \quad u_i = \bar{u}_i \quad \text{or} \quad \sigma_{ij} n_j = \bar{t}_i \quad (3.4a)$$

$$\text{Electrical:} \quad V = \bar{V} \quad \text{or} \quad D_i n_i = -\bar{Q} \quad (3.4b)$$

$$\text{Thermal:} \quad T = \bar{T} \quad \text{or} \quad -\kappa_{ij} T_{,j} n_i = \bar{q} + h_v(T - T_f) \quad (3.4c)$$

$i, j = x, y, z$ directions

Where,

\bar{u}_i = Prescribed surface displacement vector

n_j = Outward unit normal vector to the boundary Π

\bar{t}_i = Prescribed surface traction vector

\bar{V} = Prescribed surface electric potential

\bar{Q} = Prescribed Surface charge

\bar{T} = Prescribed surface temperature w.r.t. the stress-free state temperature

\bar{q} = Prescribed surface flux out

h_v = Convection heat transfer coefficient

T_f = Ambient fluid temperature w.r.t. the stress-free state temperature

3.2. Hydrogen Diffusion in PZT

As already discussed in Sec. 2.2.5, the hydrogen gas molecules H_2 , surrounding a PZT stack actuator in a hydrogen-based fuel injector, are dissociated at the surface into H-atoms after coming into contact with the metallic electrodes. The H-atoms which are formed on the surface then diffuse into the PZT layer of the actuator. Since the H-atoms are uncharged particles, they do not experience any driving force due to the electric fields developed inside the PZT layer when the actuator is electrically loaded. Therefore, *electrotransport* phenomenon is absent during the problem under investigation. Sapsathiam *et al* [40] reported that the temperature gradient has a minor influence on the diffusion of H-atoms inside the PZT. Also, the temperature gradients exist only during the early stages of diffusion and a uniform temperature is attained very rapidly by the PZT layer. Therefore, *thermotransport* phenomenon can also be safely neglected while solving the present problem. This means that the diffusion of H-atoms into the PZT layer is primarily controlled by the gradient of H-atoms concentration which is also known as *Fickian diffusion*. In this case, the time-dependent diffusion is mathematically represented using the *Fick's second law* given as [54]:

$$\dot{C} = -J_{i,i} \quad (3.5)$$

Where,

$J_i = -D_{ij}C_{,j}$ = H-atoms diffusion flux vector

C = H-atoms concentration

D_{ij} = Diffusion coefficient of H-atoms in PZT

Fig. 3.1 depicts the hydrogen exposure conditions for a single layer of a stack actuator. Hydrogen molecules H_2 attack the PZT layer from the lateral surfaces and H-atoms are formed on these surfaces. As a result, concentration gradients of H-atoms are created in the x and y directions resulting in an inward diffusion of H-atoms into the PZT layer. Accordingly, the boundary conditions for the lateral surfaces are prescribed by Eq. 3.6a. It is also assumed that there is no loss of H-atoms flux from the top and bottom surfaces. This is incorporated by prescribing zero diffusion flux boundary conditions on the top and bottom surfaces [Eq. 3.6b].

$$\text{Lateral surfaces:} \quad C = \bar{C} \quad (3.6a)$$

$$\text{Top and bottom surfaces:} \quad J_i n_i = 0 \quad (3.6b)$$

Where,

\bar{C} = Prescribed surface concentration of H-atoms

n_i = Outward unit normal vector to the top and bottom surfaces

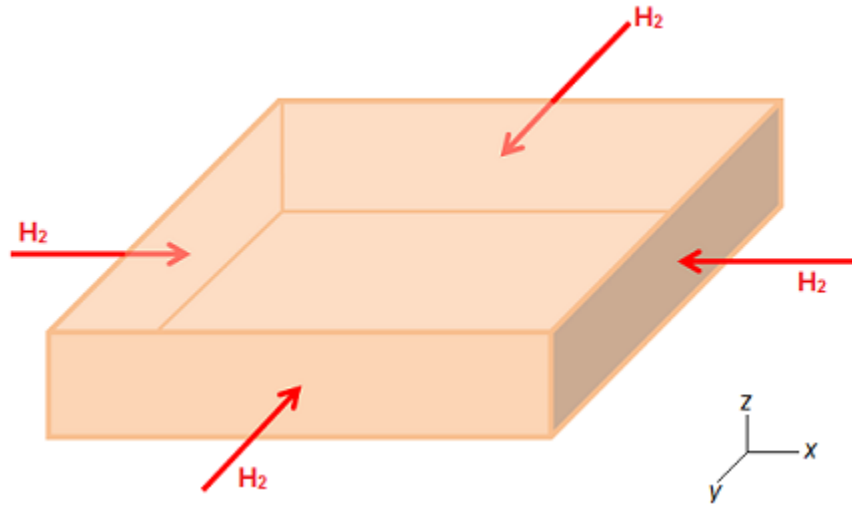


Figure 3.1 Hydrogen exposure conditions for a single PZT stack actuator layer

3.3. Effect of Hydrogen on PZT Material Properties

As already explained in the ‘Literature Review’ [Sec.1.7.1], the presence of hydrogen can affect the mechanical, electrical, piezoelectric as well as other relevant properties of the PZT material. In the present study, attention is paid only to the effect of hydrogen on the piezoelectric strain coefficient d_{33} . This is reasonable because the stroke of an actuator is primarily controlled by d_{33} and there is no significant mechanical loading on the actuator. Wu *et al* [5] experimentally measured the variation of d_{33} of 1mm x 25mm x 25mm PZT disks having Ag electrodes at different concentrations of trapped H-atoms inside the disks. The trapped H-atoms were infused into the disks either by electroplating them in solutions or by annealing them in the forming gas. The trapped hydrogen concentration was measured using the vacuum thermal extraction method and d_{33} was measured using a quasi-static piezoelectric d_{33} meter. The data reported by Wu

et al [5] is approximated by a smooth curve as shown in Fig. 3.2; where d_{33}^n is the piezoelectric strain coefficient in the absence of hydrogen. This relationship has been utilized in the present modelling work to represent a functional dependence of d_{33} on H-atoms concentration inside PZT.

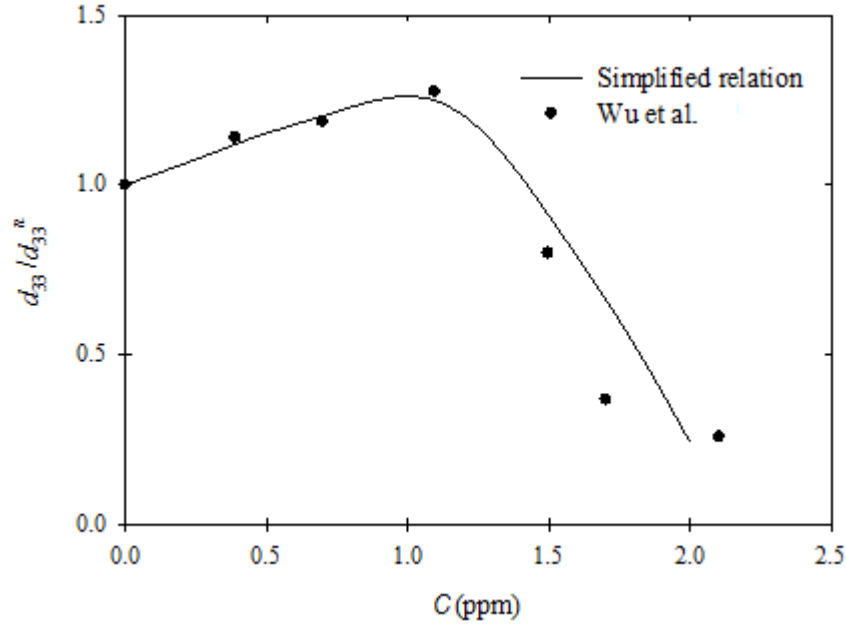


Figure 3.2 Simplified relation for the dependence of d_{33} on H-atoms concentration approximated from the results of Wu *et al* [5]

According to Wu *et al* [5], when H-atom enters PZT unit cell, it can occupy four possible sites to bond with O-atoms. The occupation of the most stable site results in the formation of H-O dipole which is favourably aligned with the host polarization. This enhances the spontaneous polarization of the PZT which consequently enhances its value of d_{33} . It should, however, be noted that the H-atom is a shallow donor impurity in the piezoelectric crystals. Therefore, if the H-atoms concentration in the PZT becomes too high, the material begins to behave more like a conductor and its piezoelectric properties (d_{33}) will be degraded. This explains the trend observed in Fig. 3.2.

It is important to note that the relationship depicted in Fig. 3.2 is for d_{33} and not e_{33} . Mathematically, e_{33} and e_{31} are a function of d_{33} . Therefore, any variation in d_{33} caused by H-atoms concentration will affect both e_{33} and e_{31} . Since the constitutive relations [Eq. 3.2] are expressed in the *e-form*, it is necessary to apply suitable conversions in order to accurately incorporate the hydrogen effects in the model.

3.4. Numerical Solution using ‘Equation Based Modelling’ in COMSOL

The ‘Equation Based Modelling’ feature of *COMSOL Multiphysics*[®] provides a flexible technique to solve simultaneous Partial Differential Equations (PDEs) in space and time. The solution procedure is based on the Finite Element Method (FEM). It provides a convenient way to solve those physical systems for which the predefined modules are not commercially available. The present problem, involving coupled mechanical, electrical, thermal and diffusion effects, is one such example. Typically in such situations, a user is required to code a complete FEM solution program. The ‘Equation Based Modelling’ feature eliminates this coding requirement from the modelling work, thereby significantly reducing the user effort involved.

The governing PDEs for a given problem can be expressed in either *strong form* or *weak form*. Depending upon the problem, the PDEs may also be linear or non-linear. In order to accommodate these variations present in the PDEs, the ‘Equation Based Modelling’ feature comes with three options [48]:

1. COEFFICIENT FORM PDE – To express *strong form* and linear PDEs
2. GENERAL FORM PDE - To express *strong form* and non-linear PDEs
3. WEAK FORM PDE - To express *weak form* PDEs

In modelling the present problem, the governing PDEs for mechanical, electrical and thermal equilibria [Eq. 3.1] and the *Fickian diffusion* [Eq. 3.5] are to be simultaneously solved for u_i , V , T and C fields. These PDEs are expressed in their *strong forms*. Moreover, as mentioned in Sec. 3.3, one of the material properties (d_{33}) is dependent upon a variable (C). This introduces non-linearity into the system of equations. Due to these reasons, the ‘General Form PDE’ option is chosen for modelling the present work. In order to use this option, *mass coefficients*, *damping coefficients*, *flux vectors* and *source terms*, present in the governing PDEs, are supplied by the user in the form of expressions. The user also supplies the expressions for the initial conditions and the applicable boundary conditions. Geometry creation, meshing and solving is performed using the software like any other commercial package. Since the treatment of the problem is purely mathematical and the results are the spatial and temporal values of the involved variables, the user is required to post-process these values in order to

analyse the physical quantities of interest. For example, in a structural engineering problem, the ‘Equation Based Modelling’ solution will only result in the displacement field and the user is required to apply appropriate conversions to it for analysing the stress and strain fields.

3.5. Model Description

During the experiments presented in Ch-2, the overall stroke of a PI actuator was measured under various ambient, operating and hydrogen exposure conditions. In order to have a closer look into the localized effects which contribute to this overall stroke and to gain a better understanding of the distribution of those localized effects within the actuator, an FEM-based numerical model for the problem under consideration is presented here. Of particular interest for an actuator application are the spatial and temporal variations of displacement in the longitudinal direction within the actuator.

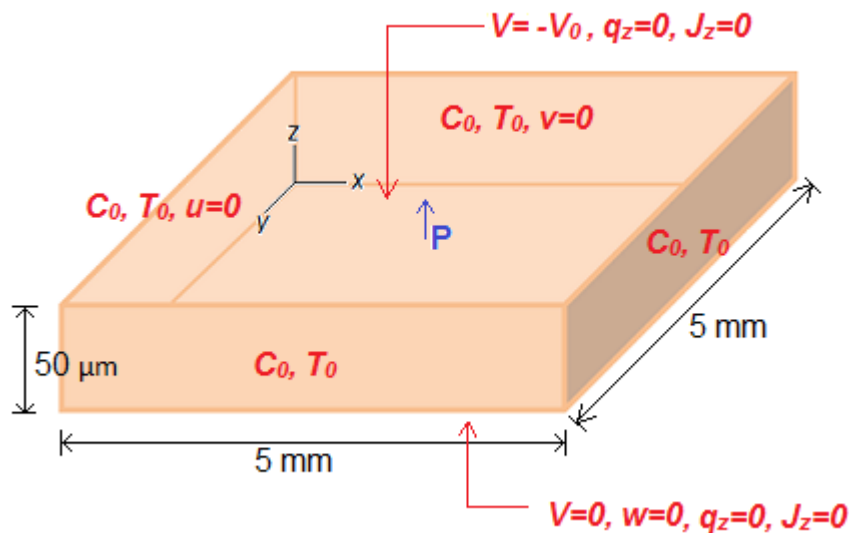


Figure 3.3 3-D model of a single PZT layer depicting its dimensions, polarization and prescribed boundary conditions

Instead of modelling the entire *PI 885.91* actuator, which was tested during the experiments, only a single actuator layer is modelled. Assuming that each layer within the actuator undergoes an equivalent longitudinal displacement during operation, the overall actuator stroke can be calculated by multiplying the longitudinal displacement of

a single layer by the total number of layers [Table 2.1]. Each layer has a rectangular disk-shaped geometry having dimensions as shown in Fig. 3.3. Electrodes are present on the top and bottom surfaces on the layer where electric voltage is applied. It should be noted that the protective ceramic insulation coating, present on the lateral surfaces of the *PI 885.91* actuator, is not a part of the model. The model, therefore, simulates the operation of an uncoated actuator in a hydrogen-based fuel injector. The modelled layer is made from PZT ceramic material which exhibits hexagonal symmetry resulting in transversely isotropic material properties [Appendix A]. It is assumed that the effect of trapped H-atoms on d_{33} of the model material is the same as that reported by Wu *et al* [5] and presented in Sec. 3.3.

Fig. 3.3 also depicts the boundary conditions prescribed for the modelled PZT layer. The mechanical displacements in x, y and z directions are zero, i.e. fixed constraint, at the planes $x=0$, $y=0$ and $z=0$ respectively. Electric potential difference of magnitude $-V_0$ is applied across the z-direction faces. A negative voltage is chosen because it creates an electric field in the positive z-direction [Eq. 3.3b]. Since the polarization within the layer (*indicated by an arrow with P*) is also in the positive z-direction, a tensile strain is produced resulting in a positive z-direction displacement within the layer. When used inside a fuel injector, the temperature of the four lateral faces of an actuator (*and the modelled PZT layer*) is assumed to be same as the ambient temperature T_0 . As already stated in Sec. 2.2.5, the H_2 gas molecules surrounding the actuator placed inside a fuel injector get dissociated into H-atoms upon coming into contact with the electrodes. The rate of formation of H-atoms depends on various factors including the temperature and pressure of surrounding H_2 gas, the type of electrodes and the presence of protective coating on the actuator. Moreover, the H-atoms are formed at the PZT-electrode interface only and not on the entire lateral surface. After formation, the H-atoms *laterally* diffuse into the PZT layer by the ‘spill over’ action. The present model, however, assumes that a uniform and constant H-atoms concentration C_0 is present on the four lateral surfaces of the modelled PZT layer. This is an idealized condition aimed at developing an early stage approximation of the hydrogen diffusion phenomenon in PZT and does not represent a definitive analysis of the problem. Due to a limited availability of experimental data, the range of C_0 values selected for analysis is between 0-2 ppm [5]. On the top and bottom surfaces of the

layer, the heat flux and the diffusion flux in z-direction from the adjacent layers cancels out resulting in a zero flux (*heat and diffusion*) boundary condition on these surfaces.

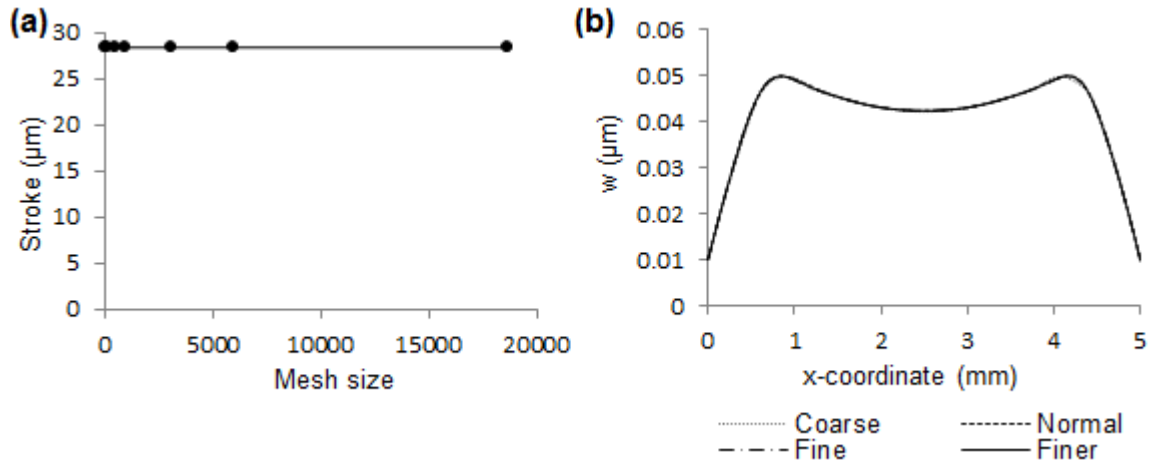


Figure 3.4 Mesh independence analysis: (a) Variation of overall actuator stroke with mesh size when $C_0=0\text{ppm}$, $T_0=20^\circ\text{C}$ and $V_0=120$ Volts; and (b) z-displacement profiles after 10 min. along the x-axis on the top surface of PZT layer for different mesh sizes when $C_0=2\text{ppm}$, $T_0=20^\circ\text{C}$ and $V_0=100$ Volts

The governing equations presented in Sec. 3.1 and 3.2 are solved using the 'Equation Based Modelling' feature of COMSOL Multiphysics[®]. A 3-D, 4-node tetrahedral element with six degrees of freedom per node (*3 displacements + 1 voltage + 1 temperature + 1 concentration*) is used to mesh the geometry. Fig. 3.4(a) shows the variation of the computed actuator stroke with mesh size (*total number of elements*) at 120V applied static voltage, 20°C temperature and no hydrogen exposure. Fig. 3.4(b) shows the z-displacement profiles after 10 min. along the x-axis on the top surface of the modelled PZT layer for different mesh sizes (*Coarse – 968 elements, Normal – 3115 elements, Fine – 5936 elements, Finer – 18630 elements*). The loading conditions are $C_0=2\text{ppm}$, $T_0=20^\circ\text{C}$ and $V_0=100$ Volts. It is clear from Fig. 3.4 that the computed overall actuator stroke and the local displacements within the layer are independent of the mesh size. Based on this analysis and due to minimal computational requirements in running the model, a 'Fine' mesh with 5936 elements is chosen for all cases during this study. Since the lateral dimensions of the PZT layer are two orders of magnitude greater than the longitudinal dimension, a meshing ratio of $x:y:z::1:1:20$ is applied during meshing. The in-built 'Time Dependent Solver' is used to generate the solution at time intervals of $\Delta t = 1$ sec. During the time-dependent analysis, the initial values for displacements,

electric voltage and concentration are set to zero and the initial temperature is set to T_{ref} .

3.6. Numerical Results and Discussion

3.6.1. Case Study I – Unexposed Actuators

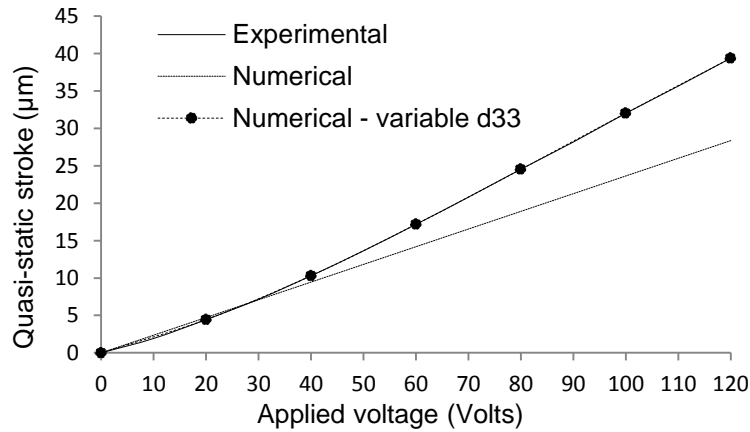


Figure 3.5 Comparison of experimental and numerical quasi-static stroke-voltage relationship at 20°C for an unexposed actuator

Stationary test cases were run on the developed FEM model to analyze the theoretical response of a piezoelectric stack actuator when subjected to static electric loading conditions. Since unexposed actuators are analyzed in this case study, the boundary concentration of H-atoms was kept as 0 ppm. Fig. 3.5 shows the numerically evaluated stroke-voltage relationship at 20°C. Since linear constitutive relations [Eq. 3.2] were used for modelling, a linear stroke-voltage relationship is obtained for the entire applied voltage range of 0-120 Volts. This numerical result is compared with the quasi-static actuator stroke measured experimentally under similar conditions. It is observed that the experimental response agrees with the theoretically predicted response for up to 30 Volts. When the applied voltage is increased further, non-linear effects such as reversible non-180° domain switching-induced strain start contributing to the linear stroke [2] and the percentage of this additional contribution increases with the increasing value of applied voltage. Mathematically, this non-linearity can be expressed as an increase in the value of property d_{33} with applied voltage. In the previous chapter, the variation of d_{33} with applied voltage has been derived from the experimentally measured

values of actuator stroke [Sec. 2.2.1]. When these variable values of d_{33} are used to run different cases in the model, the numerically obtained results match exactly with the experiments as shown in Fig. 3.5. This indicates that in order to make a more accurate prediction of the experimentally observed behaviour, the present model must be upgraded to incorporate a functional dependence of d_{33} on the applied voltage.

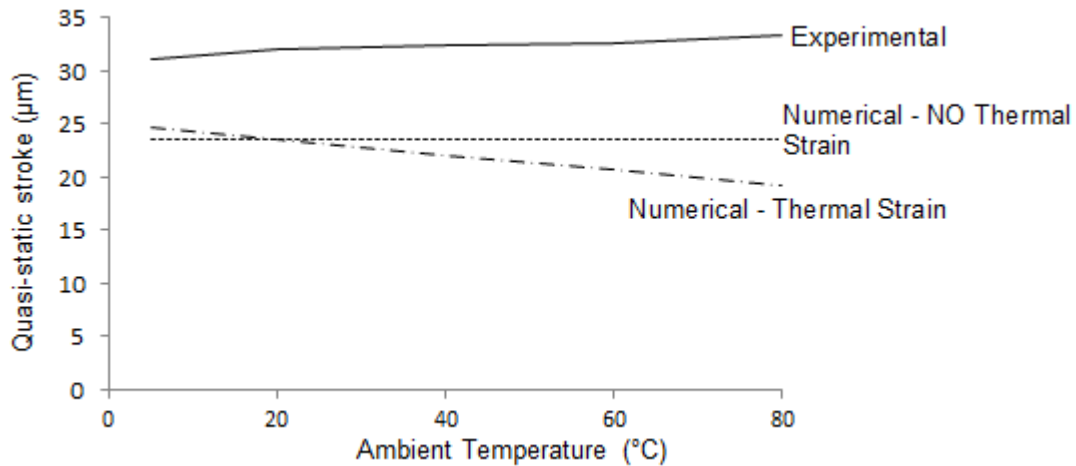


Figure 3.6 Comparison of experimentally measured and numerically evaluated quasi-static stroke-temperature relationship at 100 Volts for an unexposed actuator

An interesting behaviour is observed when the model is used to analyze the effect of ambient temperature on the actuator stroke. In a fully-coupled model, thermal strains occurring due to a change in temperature also contribute to the calculated stroke in addition to the piezoelectric effect due to the applied voltage. When these thermal strains are present, the numerically evaluated stroke is found to decrease linearly with increasing temperature as shown in Fig. 3.6. The decrease is due to a negative value of the thermal expansion coefficient (α_3) in z-direction for the PI Ceramic actuators. This is purposely engineered to compensate for an increase observed in the d_{33} value with increasing temperatures [49]. During the experiments, the actuators were allowed sufficient time to expand/contract due to the variations in ambient temperature. A quasi-static electric voltage was then applied to them and the resulting stroke was measured. This experimentally measured stroke [Fig. 3.6] was, therefore, only due to the piezoelectric effect and did not include any contributions from the thermal strain. To make an appropriate comparison with the experimental results, the thermal expansion coefficients were set to zero in the model thereby neglecting any thermal strains. When

compared, the experimentally measured average value of the stroke is greater than the numerically evaluated value due to the non-linear effects present at the applied voltage of 100 Volts. The slight increase in the experimental stroke with temperature indicates that the d_{33} value is dependent on temperature. This dependency is also not included in the linear model presented here.

3.6.2. Case Study II – Hydrogen Exposed Actuators

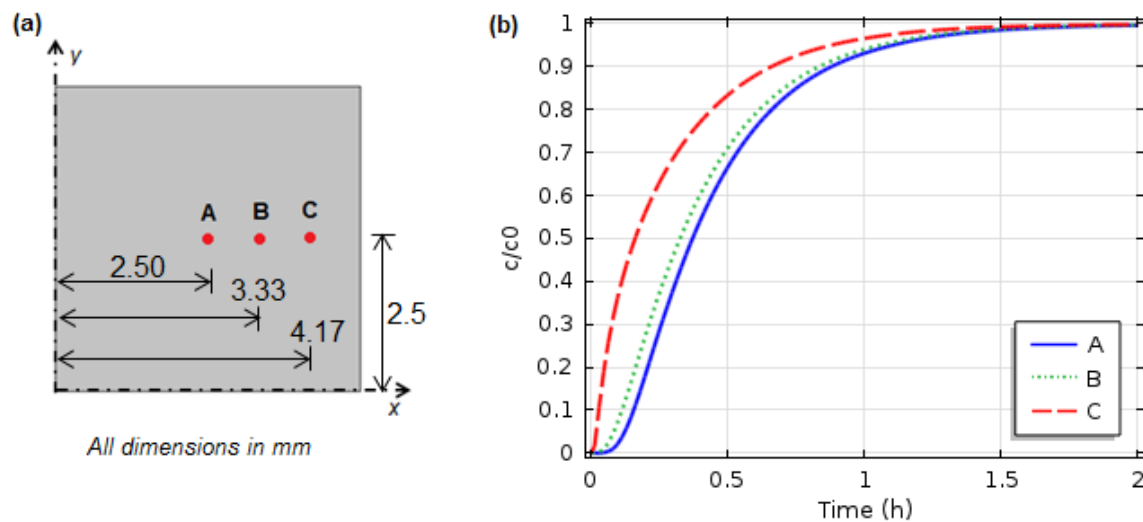


Figure 3.7 (a) Location of analysis points on the top surface of the model; and (b) Concentration time-history at the analysis points when $T_0=80^\circ\text{C}$ and $C_0=2\text{ppm}$

In this case study, the effect of hydrogen exposure on the modelled PZT layer is analyzed at different ambient temperatures when a static voltage is applied to the actuator. Fig. 3.7(a) shows the location of three analysis points (A, B and C) on the top surface of the model. The time-history of H-atoms concentration at these points is shown in Fig. 3.7(b) for boundary conditions $T_0=80^\circ\text{C}$ and $C_0=2\text{ppm}$. As expected, the concentration increases more rapidly at point C which is closer to the exposed surface compared to point A which lies in the middle and is farthest from the exposed surface. All the points reach the same steady-state concentration after approx. 2 hours. However, if the duration of injector operation is less than 2 hours, the concentrations will be different at all the points producing a non-uniform distribution of concentration and its dependent property d_{33} within the PZT layer.

Fig. 3.8 shows the temperature time-history at the analysis points for the same boundary conditions. The initial temperature is assumed to be the reference temperature T_{ref} which is also the room temperature of 20°C. The trend followed by the temperature time-history plot is similar that of the concentration time-history plot. However, the PZT layer reaches a uniform steady-state temperature condition in approx. 20 s which is much faster than the time taken to reach steady-state diffusion. Since a uniform temperature is attained so rapidly, there are negligible temperature gradients within the PZT layer that can act as driving forces for diffusion. This observation justifies the assumption made in Sec. 3.2 to neglect the *thermotransport* phenomenon while modelling hydrogen diffusion.

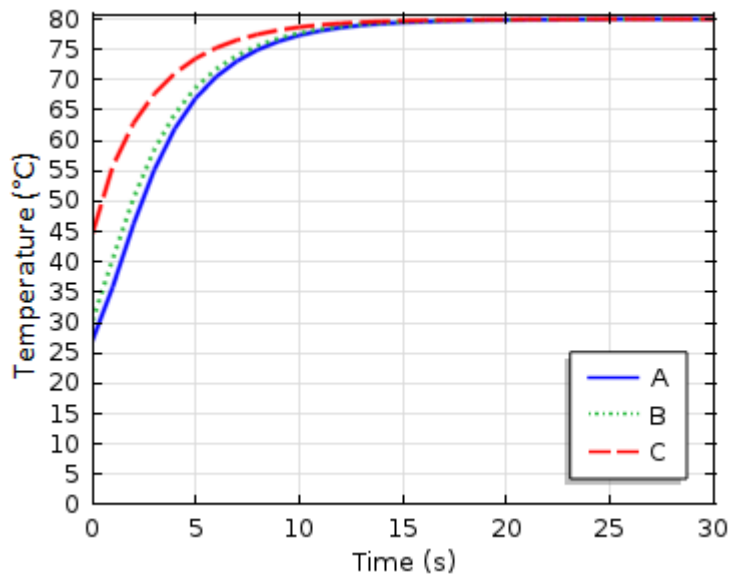


Figure 3.8 Temperature time-history at the analysis points when $T_0=80^\circ\text{C}$ and $C_0=2\text{ppm}$

For a fuel injector application, the longitudinal stroke of a piezoelectric actuator is the most important variable and therefore, requires an in-depth analysis. As already mentioned, the longitudinal stroke in the present model can be calculated by multiplying the z-direction displacement w of a single layer by the total number of layers (600). Fig. 3.9 shows the time-history of displacement w at two different temperatures (20°C and 80°C) when the actuator is exposed to a boundary concentration of $C_0=2\text{ppm}$ and subjected to a static electric voltage of $V_0=100$ Volts. It is evident that the presence of hydrogen has a significant effect on the deformation of the PZT layer. Unlike the case of

an unexposed layer, the displacement w is not always uniform for a PZT layer exposed to hydrogen. The displacement initially increases and then begins to decrease with time. This is attributed to the nature of dependence of d_{33} on H-atoms concentration as depicted in Fig. 3.2. A uniform displacement profile is achieved after approx. 2 hours, the duration coinciding with the time taken to reach the steady-state concentration [Fig. 3.7]. The trend of displacement time-history does not seem to vary with temperature. However, it is interesting to note that the magnitude of displacement is less at 80°C compared to that at 20°C. This is attributed to a negative thermal expansion coefficient in z-direction for the PI actuators [Appendix A]. The variation in displacement due to the thermal effects occurs during the initial 20 seconds and H-atoms concentration is the only factor responsible for the variation beyond this time.

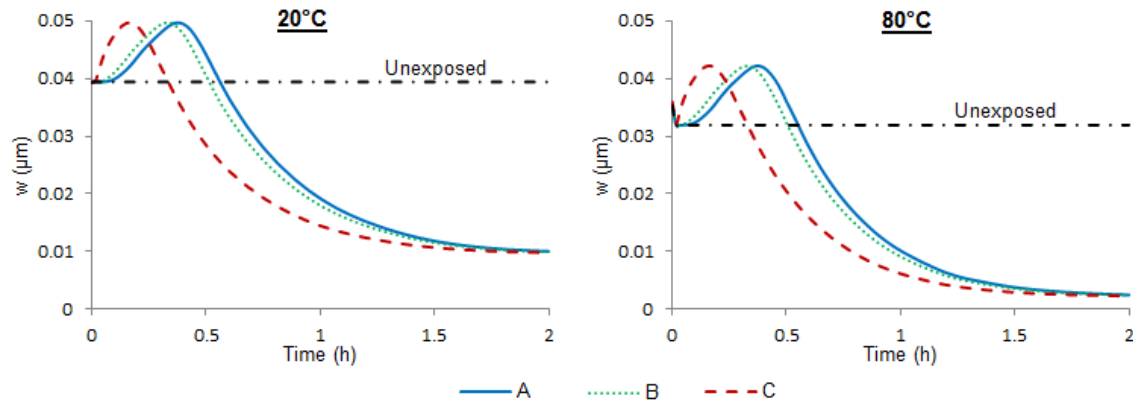


Figure 3.9 Displacement time-history at the analysis points for $T_0=20^\circ\text{C}$ and 80°C , $C_0=2\text{ppm}$ and $V_0=100$ Volts

Fig. 3.10 shows the concentration and displacement profiles along the x-axis on the top surface of the modelled PZT layer. The loading conditions are $C_0=2\text{ppm}$, $T_0=20^\circ\text{C}$ and $V_0=100$ Volts. Since this analysis is performed at room temperature, the effect of thermal expansion on the displacement is nullified. It is obvious from Fig. 3.10(a) that the concentration is not always uniform along the x-axis. The dependence of d_{33} on the concentration results in a non-uniform displacement along the top surface of the PZT layer as shown in Fig. 3.10(b). The presence of displacement non-uniformity, until a steady-state concentration is reached, can enhance electrode delamination process in an actuator under repeated hydrogen exposure cycles. This is a very critical issue which can affect the durability of these actuators in hydrogen-based fuel injector applications. In addition to that, the final steady-state displacement is approximately 75%

less than that of an unexposed actuator [Fig. 3.9]. Consequently, the final steady-state stroke will also be proportionately smaller causing a severe performance limitation while using these actuators in the hydrogen-based fuel injectors.

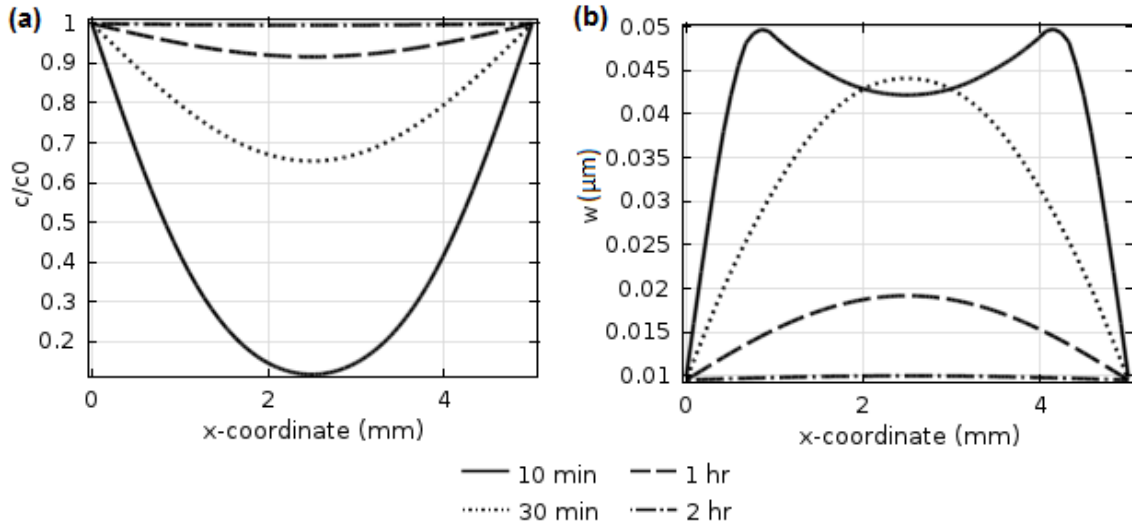


Figure 3.10 (a) Concentration profiles; and (b) Displacement profiles; along x-axis on the top surface of PZT layer at different times when $C_0=2$ ppm, $T_0=20^\circ\text{C}$ and $V_0=100$ Volts

According to the experimental results reported by *Wu et al* [5] shown in Fig. 3.2, the piezoelectric strain coefficient d_{33} shows an increasing trend with hydrogen concentration for up to 1 ppm. However, if the concentration increases further from 1 ppm to 2 ppm, the value of d_{33} begins to decrease. Therefore, the behaviour of an actuator when the boundary concentration is below 1 ppm can be expected to differ from the case when it is between 1-2 ppm. This has been explored in Fig. 3.11 which shows the displacement time-history and the displacement profiles along the x-axis when the boundary conditions are $C_0=1$ ppm, $T_0=20^\circ\text{C}$ and $V_0=100$ Volts. As expected, the displacement time-history at all the analysis points (*A*, *B* and *C*) shows only an increasing trend culminating in a displacement which is greater than that of an unexposed actuator. Also, the time taken to reach a steady state displacement is approx. 1 hour which is about half of what it takes at 2 ppm hydrogen exposure [Fig. 3.9]. The shape of the displacement profiles along the x-axis at 1 ppm [Fig. 3.11(b)] is markedly different and less complex compared to that at 2 ppm [Fig. 3.10(b)]. Based on these results, it may be concluded that the durability and performance of a PZT-based

stack actuator would be much less compromised if the boundary concentration of H-atoms is maintained below 1 ppm.

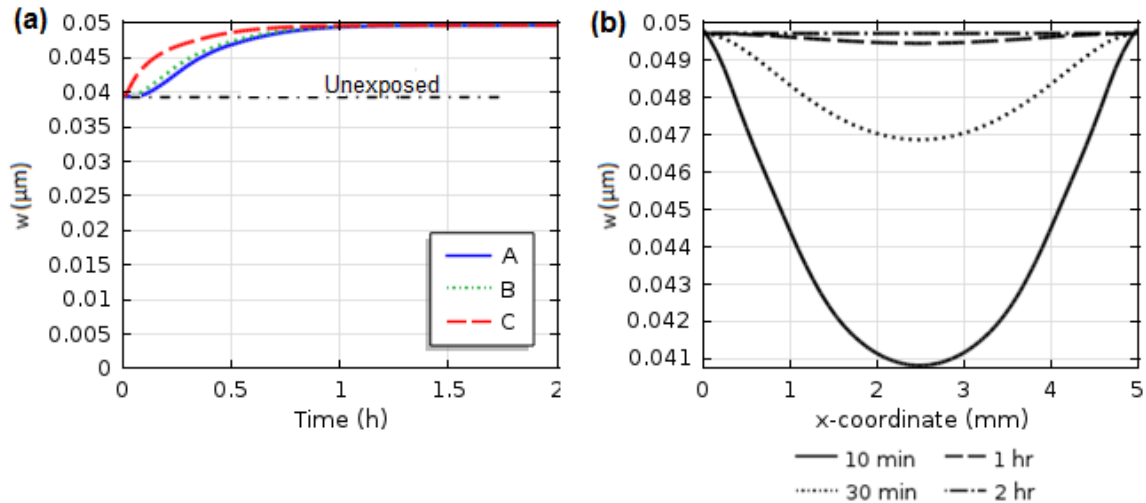


Figure 3.11 (a) Displacement time-history at the analysis points; and (b) Displacement profiles along x-axis on the top surface of PZT layer at different times; when $C_0=1$ ppm, $T_0=20^\circ\text{C}$ and $V_0=100$ Volts

3.7. COMSOL Model Validation with In-house Thermo-Electro-Mechanical FE Model

As already mentioned in Sec. 3.4, some engineering problems (*including the present one*) cannot be completely defined and therefore, solved with the limited modules available in the current commercial packages. This makes it necessary to develop in-house computer programs which can numerically model and solve such problems. Alternatively, utilization of the 'Equation Based Modelling' feature of *COMSOL Multiphysics*[®] can help reduce some of the effort required in the program development. This feature of COMSOL has been utilized in in the present work to model a piezoelectric stack actuator exposed to hydrogen under conditions relevant to the hydrogen-based fuel injectors and the results of the analysis are presented in the previous section. In order to validate the COMSOL model and to develop an understanding of the FE formulations and numerical procedures involved, an in-house FE-based numerical model was additionally developed in MATLAB to simulate the Thermo-Electro-Mechanical response of a stack actuator in 3-D space. This FE model is based on the *Principle of Virtual Work* and uses 3-D eight-node hexahedron

isoparametric finite elements with five degrees of freedom per node. A single layer of a PZT-based piezoelectric stack actuator is modelled. A detailed description of the Principle of Virtual Work, FE formulation using this principle and utilization of the hexahedron isoparametric finite elements for modelling is provided in Appendix B.

Fig. 3.12 shows the stroke-voltage relationship at 20°C under static electric loading conditions obtained from both the COMSOL model and the in-house FE program developed in MATLAB. It is evident that the actuator response predicted by both the models is identical. This observation confirms the validity of COMSOL model's results under the conditions selected here. Moreover, since different types of finite elements were used in the two models, this comparison justifies the choice of tetrahedral element during COMSOL modelling.

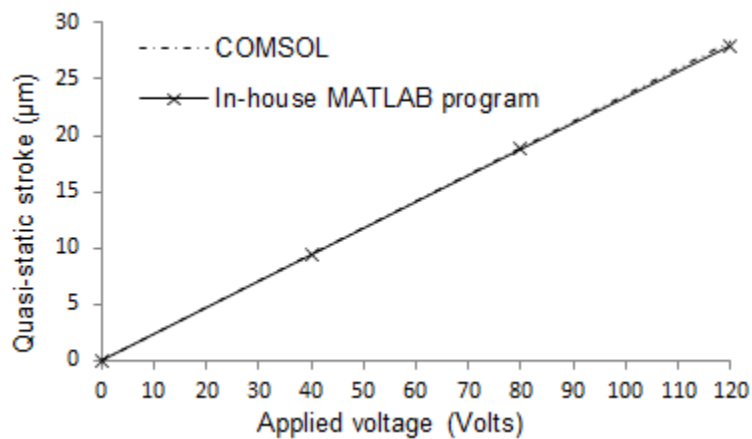


Figure 3.12 Stroke-voltage relationship at 20°C under static electric loading obtained from COMSOL model and in-house MATLAB program

3.8. Summary of Numerical Results

A Finite Element Method (FEM) based numerical model is developed using the 'Equation Based Modelling' feature of *COMSOL Multiphysics*[®] to study the 3-dimensional behaviour of a piezoelectric stack actuator exposed to hydrogen. The model incorporates full coupling between mechanical, electrical, thermal and diffusion state variables. Experimental data for the dependence of piezoelectric strain coefficient d_{33} on hydrogen concentration [5] is implemented in the analysis. Selected numerical results in the form of time-histories and spatial profiles of concentration of hydrogen, temperature

and actuator stroke are presented for conditions relevant to hydrogen-based fuel injectors. When a PI-885.91 actuator is subjected to external temperature increase, a steady-state temperature along with a uniform temperature profile is attained by the actuator within approx. 20 sec. The diffusion of hydrogen is relatively slower and it takes approx. 2 hrs to reach a steady-state concentration. Based on these findings, it is concluded that the effect of temperature gradient on diffusion is negligible and, therefore, the assumption to neglect thermodtransport in the model is justified. The stroke of an actuator is significantly influenced by the presence of hydrogen within the actuator. When exposed to a low hydrogen concentration ($\leq 1 \text{ ppm}$), the steady-state stroke is greater than the stroke of an unexposed actuator indicating a positive effect on the actuator performance. At higher hydrogen concentrations ($1-2 \text{ ppm}$), however, a significant non-uniformity of stroke is found within an actuator layer which can potentially cause electrode delamination. Moreover, the final steady-state stroke is substantially lower than the stroke of an unexposed actuator resulting in a highly compromised actuator performance which may limit their use in the fuel injector applications. A comparison between experimentally measured and numerically evaluated relationships of the actuator stroke with applied voltage and ambient temperature under static electric loading and unexposed conditions is also presented. The comparison highlights the need of adding non-linear effects (*dependence of d_{33} on voltage and temperature*) to the present model in order to predict the actuator behaviour more accurately.

4. Conclusions

4.1. Summary and Conclusions

The major findings and conclusions of the present research effort are summarized as follows:

1. A comprehensive experimental investigation of both quasi-static and dynamic thermo-electro-mechanical performance of PZT-based stack actuators under operating conditions relevant to hydrogen-based fuel injection systems is provided in this thesis. PI-885.91 model of actuators manufactured by PI Ceramics, Germany were selected to carry out this study. The experimental findings provide a better understanding of the response of these actuators under different controlling parameters, such as voltage, frequency, rise time, duty cycle and DC offset of the driving signal. The effect of environmental parameters, such as ambient temperature and exposure to hydrogen, on the actuator performance is also determined. Dependence of piezoelectric strain coefficient d_{33} on the experimental parameters is derived and self-heating phenomenon during a dynamic operation is also investigated. Microstructure evolution and dielectric behaviour is correlated to some of the observed results. It is found that:
 - a) The actuator stroke-voltage relationship is slightly non-linear with the slope increasing with applied voltage. This is attributed to the presence of non-linear effects such as non-180° domain switching at higher driving voltages. The increase in the stroke of the PI actuators with ambient temperature, however, is very minor within the tested temperature range of 5-80°C. The dynamic stroke shows a minor reduction with applied signal frequency for up to 100 Hz. The effect of DC offset voltage on the dynamic stroke is observed only at higher applied voltages where the DC offset causes the stroke to decrease slightly due to the pinning of domain walls. The duty cycle is found to have no effect on the actuator stroke. A lower rise time

percentage of the applied dynamic voltage provides a longer holding time at the maximum voltage producing an increase in the stroke at lower rise times.

- b) The piezoelectric strain coefficient d_{33} is constant with the applied voltage for up to 20 Volts but increases linearly with the ambient temperature in the range 5-80°C. This shows that at low applied voltages (≤ 20 Volts), the extrinsic contributions to d_{33} are only due to temperature variations. An additional extrinsic contribution to d_{33} is introduced at higher voltages due to an increased activity of non-180° domain walls induced by these voltages.
- c) Self-heating in the PI actuators was experimentally investigated under a sinusoidal electric loading at different applied voltages (30-120 V_{pp}) and frequencies (100-200 Hz). The steady-state temperature attained by the actuators showed a non-linear increase with both applied voltage and frequency. It is also found that the increase in the actuator temperature due to self-heating does not produce any performance changes when operated at frequencies up to 200 Hz.
- d) *Continuous exposure* of the PI actuators to hydrogen at 100°C temperature and 10 MPa pressure for up to 12 weeks has a negligible effect on their performance when tested within the temperature range 5-80°C. *Cyclic exposure*, consisting of multiple 4 week exposure cycles with a 4 week aging period between two consecutive cycles, also does not induce any performance variations. This resistance to hydrogen is attributed mainly to the presence of a protective ceramic insulation layer on the lateral surface of the PI actuators which deactivates the mechanism responsible for hydrogen diffusion into the internal PZT layers. No changes to the actuator's microstructure and dielectric properties are observed during the hydrogen exposure.
- e) The electrical fatigue response of the PI actuators remains consistent for up to 1.8×10^8 cycles when cycled with a 100 V_{pp} , 100 Hz sinusoidal electrical signal. Exposure of the cycled actuators to hydrogen for 3 weeks does produce any performance variation which indicates that the fatigue cycling

does not introduce any cracks/openings in the ceramic insulation which may activate the hydrogen diffusion mechanism.

2. A numerical model to predict the thermo-electro-mechanical response of a single PZT-layer of the PI-885.91 stack actuators when exposed to hydrogen is presented in this thesis. The model is based on the Finite Element Method (FEM) and is developed using the 'Equation Based Modelling' feature of *COMSOL Multiphysics*[®]. This model is a first attempt to incorporate full coupling between mechanical, electrical, thermal and diffusion variables in a 3-D space. Based on the results obtained from selected case studies, the major findings from the model are as follows:
 - a) When subjected to an ambient temperature different from the initial room temperature, the PZT layer quickly reaches a steady-state temperature in approx. 20 sec. On the other hand, the diffusion of hydrogen (*H-atoms*) into the layer is much slower and a steady-state concentration is attained in approx. 2 hrs. This suggests that the contribution of *thermotransport* phenomenon, caused by the presence of temperature gradients, to the hydrogen diffusion flux is negligible.
 - b) The stroke of an actuator is significantly influenced by the presence of hydrogen within the actuator. The effects, however, may be different depending upon the value of hydrogen concentration to which the PZT-layer is exposed. Below a boundary concentration of 1 ppm, the stroke of an actuator increases due to the presence of hydrogen producing a positive effect on the actuator performance. Between 1-2 ppm boundary concentrations, the effects on performance are highly deleterious that may result in a compromised actuator performance and its possible damage due to electrode delamination.

4.2. Recommendations for Future Work

To gain a deeper understanding of the behaviour of piezoelectric stack actuators in hydrogen-based fuel injectors, the following suggestions are made for future work:

- (1) In the present study, the exposure of the actuators to hydrogen and their performance testing was not conducted simultaneously. When an actuator is operated inside a hydrogen environment, the presence of induced electric, stress and thermal fields can possibly complicate the diffusion of hydrogen into the actuator's PZT layers. This can be explored by building a hydrogen-safe test-rig to carry out the experiments in the presence of hydrogen.
- (2) Piezoelectric ceramics are brittle and susceptible to cracking under cyclic electric-field and/or mechanical loading [52]. The extremely low rise times demanded by the fuel injectors can further aggravate this propensity for cracking. A comprehensive investigation of the fatigue behaviour of actuators under loading conditions relevant to a typical fuel injector is necessary to ascertain the durability of the proposed actuators. For the reasons given in (1), this fatigue testing should, ideally, be performed in a hydrogen environment.
- (3) The comparison of experimental and numerical results done in Ch-3 showed that the response of the actuators can be non-linear due to the dependence of material properties (*such as d_{33}*) on the ambient and controlling variables. This dependency needs to be functionally quantified based on the available literature and included in the model in order to make a more accurate prediction of the actuator behaviour.

References

- [1] Scharf A., "Prize-Winning Piezo, Piezo-Actuators in Fuel Injection Systems", *EPCOS technical articles* 2006 (<http://www.epcos.com>).
- [2] Li F.X., Rajapakse R.K.N.D., Mumford D., Gadala M., "Quasi-static thermo-electromechanical behaviour of piezoelectric stack actuators", *Smart Materials and Structures* 17 (2008) 015049.
- [3] Senousy M.S., Li F.X., Mumford D., Gadala M., Rajapakse R.K.N.D., "Thermo-electro-mechanical Performance of Piezoelectric Stack Actuators for Fuel Injector Applications", *Journal of Intelligent Material Systems and Structures* 20 (2009) 387.
- [4] Wang H., Cooper T.A., Lin H.T., Wereszczak A.A., "Fatigue responses of lead zirconate titanate stacks under semibipolar electric cycling with mechanical preload", *J. Appl. Phys.* 108 (2010) 084107.
- [5] Wu M., Huang H., Chu W., Guo L., Qiao L., Xu J., Zhang T.Y., "Tuning the ferroelectric and piezoelectric properties of $0.91\text{Pb}(\text{Zn}_{1/3}\text{Nb}_{2/3})\text{O}_3\text{-}0.09\text{PbTiO}_3$ single crystals and lead zirconate titanate ceramics by doping hydrogen", *J. Phys. Chem. C* 114 (2010) 9955–9960.
- [6] Peng X., Su Y.J., Gao K.W., Qiao L.J., Chu W.Y., "Hydrogen fissure in PZT ferroelectric ceramic", *Mater. Lett.* 58 (2004) 2073–2075.
- [7] Wang Y., Chu W.Y., Qiao L.J., Su Y.J., "Hydrogen-induced delayed fracture of PZT ceramics during dynamic charging under constant load", *Mater. Sci. Eng.*, B98 (2003) 1–5.
- [8] Shafiei A., Oprea C., Troczynski T., "Investigation of the Effects of High-Pressure Hydrogen on $\text{Pb}(\text{Zr,Ti})\text{O}_3$ (PZT) Ceramics" *J. Am. Ceram. Soc.* 95 [2] (2012) 782–787
- [9] Shafiei A., Oprea C., Alfantazi A., Troczynski T., "In situ monitoring of the effects of hydrogen on $\text{Pb}(\text{Zr,Ti})\text{O}_3$ structure" *Journal of Applied Physics* 109 (2011) 114108
- [10] Shafiei A., Nickchi T., Oprea C., Alfantazi A., Troczynski T., "Investigation of hydrogen effects on the properties of $\text{Pb}(\text{Zr,Ti})\text{O}_3$ in tetragonal phase using water electrolysis technique" *Applied Physics Letters* 99 (2011) 212903

- [11] Callister W.D., Rethwisch D.G., "Fundamentals of Materials Science and Engineering" *John Wiley and Sons Inc.*, 2008
- [12] Masys A.J., Ren W., Yang G., Mukherjee B.K., "Piezoelectric strain in lead zirconatetitanate ceramics as a function of electric field, frequency, and dc bias" *Journal of Applied Physics* 94 (2003) 1155
- [13] Sherrit S., Van Nice D.B., Graham J.T., Mukherjee B.K., Wiederick H.D., "Domain wall motion in piezoelectric materials under high stress" *Proceedings of the Eighth IEEE International Symposium on Applications of Ferroelectrics* (1992)167.
- [14] Ochi A., Takahashi S., Tagami S., "Temperature characteristics for multilayer piezoelectric ceramic actuator" *Japanese Journal of Applied Physics* (1985) 24:209
- [15] Zhang Q. M. *et al*, "Direct evaluation of domain-wall and intrinsic contributions to the dielectric and piezoelectric response and their temperature dependence on lead zirconate–titanate ceramics" *Journal of Applied Physics* 75 (1994) 454–9
- [16] Leo D.J., "Engineering Analysis of Smart Material Systems" *John Wiley and Sons Inc.*, 2007
- [17] Cady W.G., "Piezoelectricity" *McGraw-Hill*, 1946
- [18] Ikeda T., "Fundamentals of Piezoelectricity" *Oxford University Press Inc.*, 1996
- [19] Uchino K., "Piezoelectric Actuators and Ultrasonic Motors" *Kluwer Academic Publishers*, 1997
- [20] Youssef M.S.S., "Experimental Investigation and Theoretical Modelling of Piezoelectric Actuators used in Fuel Injectors" *Ph.D. thesis, The University of British Columbia*, 2009
- [21] Lines M., Glass A., "Principles and applications of ferroelectrics and related materials" *Clarendon Press*, 1979
- [22] Pokharel B.P., Karki N.R., "Electrical Engineering Materials" *Alpha Science International Ltd*, 2007
- [23] Fujishima S., "The history of ceramic filters" *IEEE Transactions on Ultrasonics, Ferroelectrics and Frequency Control*, 2000; 47:1
- [24] Jäker P., "Electro-Mechanical Characterization of High-Performance Piezoactuators" *Proceedings of SPIE*, 1997; 3039:670
- [25] Ardelean E.V., Cole D.G., Clark R.L., "High performance 'V-stack' piezoelectric actuator" *Journal of Intelligent Material Systems and Structures*, 2004; 15:879

- [26] Chen Q., Yao D.J., Kim C.J., Carman G.P., "Frequency response of an inchworm motor fabricated with micromachined interlocking surface mesoscale actuator device (MAD)" *Proceedings of SPIE*, 1998; 3329:768
- [27] Haertling G.H., "Ferroelectric Ceramics: History and Technology" *Journal of the American Ceramic Society*, 1999; 82:797
- [28] Uchino K., "Ferroelectric Devices" *Marcel Dekker Inc.*, 2000
- [29] Wolff A., Cramer D., Hellebrand H., Probst I., Lubitz K., "Optical two channel elongation measurement of PZT piezoelectric multilayer stack actuators" *IEEE International Symposium on Applications of Ferroelectrics*, 1994
- [30] Gromek B., Shen J.J., "Multiple stack piezoelectric actuator for a fuel injector" *United States Patent, Patent Number 6,345,771*, 2000
- [31] Takase S., "Piezoelectric actuator and fuel-injection apparatus using the actuator" *United States Patent, Patent Number 6-155-500*, 1999
- [32] Fujii A., Toyao T., "Piezoelectric actuators with high reliability for diesel injection valve" *10th International Conference on New Actuators*, 2006
- [33] Aburatani H., Harada S., Uchino K., Furuta A., Fuda Y., "Destruction mechanisms in ceramic multilayer actuators" *Japanese Journal of Applied Physics*, 1994
- [34] Nuffer J., Bein T., "Application of piezoelectric materials in transportation industry" *Global Symposium on Innovative Solutions for the Advancement of the Transport Industry*, 2006
- [35] US Department of Energy website (<http://www.hydrogen.energy.gov>)
- [36] Lanz A., Heffel J., Messer C., "Hydrogen Fuel Cell Engines and Related Technologies" *Course, College of the Desert*, 2001
- [37] Benjeddou A., "Advances in piezoelectric finite element modelling of adaptive structural elements: a survey" *Journal of Computers and Structures*, 2000, Vol. 76, Pg. 347-363
- [38] Senousy M. S., Gadala M. S., Rajapakse R.K.N.D., "Coupled finite element modelling of piezothermoelastic materials" *Proceedings of SPIE*, 2007, Vol. 6526, Pg. 65260H1-11
- [39] Senousy M. S., Rajapakse R.K.N.D., Gadala M. S., "A Temperature-Dependent Two-Step Domain-Switching Model for Ferroelectric Materials" *Acta Materialia*, 2009
- [40] Sapsathiarn Y., Rajapakse R.K.N.D., "Modelling of Hydrogen Diffusion in a Piezoceramic with Temperature Gradient" *IEEE International Symposium on Applications of Ferroelectrics - ISAF*, 2011

- [41] Uchino K., Hirose S., "Loss mechanisms in piezoelectrics: How to measure different losses separately" *IEEE Transactions on Ultrasonics, Ferroelectrics, and Frequency Control*, 2001
- [42] Yao K., Uchino K., Xu Y., Dong S., Lim L.C., "Compact piezoelectric stacked actuators for high power applications" *IEEE Transactions on Ultrasonics, Ferroelectrics, and Frequency Control*, 2000
- [43] Keoschkerjan R., Harutyunyan M., Wurmus H., "Analysis of self-heating phenomenon of piezoelectric microcomponents actuated harmonically" *Microsystem Technologies*, 2002
- [44] Ronkanen P., Kallio P., Viikko M., Koivo H.N., "Self heating of piezoelectric actuators: Measurement and compensation" *International Symposium on Micro-NanoMechatronics and Human Sci.*, 2004
- [45] Zheng J., Takahashi S., Yoshikawa S., Uchino K., de Vries J.W.C., "Heat generation in multilayer piezoelectric actuators" *Journal of the American Ceramic Society*, 1996
- [46] Lesieutre G.A., Fang L., Koopmann G.H., Pai S.P., Yoshikawa S., "Heat generation of a piezoceramic induced-strain actuator embedded in a glass/epoxy composite panel" *Smart Structures and Materials*, 1996
- [47] Senousy M. S., Rajapakse R.K.N.D., Mumford D., Gadala, M. S., "Self-heat generation in piezoelectric stack actuators used in fuel injectors" *Journal of Smart Materials and Structures*, 2009
- [48] "COMSOL Multiphysics® Modelling Guide" Version 3.5a, 2008
- [49] "Piezoelectric Actuators – COMPONENTS, TECHNOLOGIES, OPERATION" (www.piceramic.com)
- [50] Zhang Q.M., Wang H., Zhao J., "Effect of Driving Field and Temperature on the Response Behavior of Ferroelectric Actuator and Sensor Materials" *Journal of Intelligent Material Systems and Structures*, 1995
- [51] Safari A., Akdogan E.K., "Piezoelectric Actuators and Acoustic Materials for Transducer Applications" *Springer*, 2008
- [52] Shindo Y., Narita F., Horiguchi K., Magara Y., Yoshida M., "Electric fracture and polarization switching properties of piezoelectric ceramic PZT studied by the modified small punch test" *Acta Materialia*, 2003
- [53] Alvine K.J., Shutthanandan V., Bennett W. D., Bonham C. C., Skorski D., Pitman S. G., Dahl M. E., Henager C. H., "High-Pressure Hydrogen Materials Compatibility of Piezoelectric Films" *Applied Physics Letters*, 2010
- [54] Mehrer H., "Diffusion in Solids" *Springer*, 2007

Appendices

Appendix A.

Material Properties of PI 885.91 actuators

Elastic stiffness matrix at constant electric field (Source: PI Ceramic, Germany)

$$c^E = \begin{bmatrix} 12.30 & 7.67 & 7.02 & 0 & 0 & 0 \\ 7.67 & 12.30 & 7.02 & 0 & 0 & 0 \\ 7.02 & 7.02 & 9.71 & 0 & 0 & 0 \\ 0 & 0 & 0 & 2.23 & 0 & 0 \\ 0 & 0 & 0 & 0 & 2.23 & 0 \\ 0 & 0 & 0 & 0 & 0 & 2.31 \end{bmatrix} 10^{10} N/m^2$$

Absolute dielectric permittivity matrix at constant strain (Source: PI Ceramic, Germany)

$$\varepsilon^S = \begin{bmatrix} 930 & 0 & 0 \\ 0 & 930 & 0 \\ 0 & 0 & 857 \end{bmatrix} 8.8542 \times 10^{-12} C/m.V$$

Piezoelectric strain coefficient matrix (Source: PI Ceramic, Germany)

$$d = \begin{bmatrix} 0 & 0 & 0 & 0 & 5.35 & 0 \\ 0 & 0 & 0 & 5.35 & 0 & 0 \\ -1.74 & -1.74 & 3.94 & 0 & 0 & 0 \end{bmatrix} 10^{-10} m/V$$

Thermal expansion coefficient matrix (Source: PI Ceramic, Germany)

$$\alpha = \begin{bmatrix} 6 \\ 6 \\ -2.5 \\ 0 \\ 0 \\ 0 \end{bmatrix} 10^{-6} /K$$

Pyroelectric coefficient matrix (Source: Senousy et al [38])

$$\alpha = \begin{bmatrix} 2.5 \\ 2.5 \\ 2.5 \end{bmatrix} 10^{-5} C/m^2.K$$

Thermal conductivity matrix (Source: PI Ceramic, Germany)

$$\kappa = \begin{bmatrix} 1.1 & 0 & 0 \\ 0 & 1.1 & 0 \\ 0 & 0 & 1.1 \end{bmatrix} W/m.K$$

Diffusion coefficient matrix (Source: Sapsathiarn et al [40])

$$D = \begin{bmatrix} 1.1 & 0 & 0 \\ 0 & 1.1 & 0 \\ 0 & 0 & 1.1 \end{bmatrix} 10^{-9} \text{ m}^2/\text{s}$$

Mass density (Source: *PI Ceramic, Germany*)

$$\rho = 7800 \text{ kg/m}^3$$

Specific heat at constant volume (Source: *PI Ceramic, Germany*)

$$C_v = 350 \text{ J/kg.K}$$

Appendix B.

FE Formulation of the In-house Thermo-Electro-Mechanical Model

APPLICATION OF THE PRINCIPLE OF VIRTUAL WORK:

Upon subjecting a piezoelectric material volume Ω to virtual displacements $(\delta u_x, \delta u_y, \delta u_z)$, virtual electric potential change (δV) and virtual temperature change (δT) and thereafter, applying the *Principle of Virtual Work* to the Thermo-Electro-Mechanical governing equations given in Chapter-3 [Eq. 3.1] gives the following result:

$$\int_{\Omega} (\sigma_{ij,j} + b_i - \rho \ddot{u}_i) \delta u_i \, d\Omega + \int_{\Omega} (D_{i,i} - \varphi_e) \delta \varphi \, d\Omega + \int_{\Omega} (q_{i,i} + T_{ref} \dot{S} - \varphi_t) \delta \theta \, d\Omega = 0 \quad (B.1)$$

Upon expanding the terms inside brackets we get

$$\begin{aligned} \int_{\Omega} \sigma_{ij,j} \delta u_i \, d\Omega + \int_{\Omega} b_i \delta u_i \, d\Omega - \int_{\Omega} \rho \ddot{u}_i \delta u_i \, d\Omega + \int_{\Omega} D_{i,i} \delta V \, d\Omega - \int_{\Omega} \varphi_e \delta V \, d\Omega + \int_{\Omega} q_{i,i} \delta T \, d\Omega \\ + \int_{\Omega} T_{ref} \dot{S} \delta T \, d\Omega - \int_{\Omega} \varphi_t \delta T \, d\Omega = 0 \end{aligned} \quad (B.2)$$

$\sigma_{ij,j}$, $D_{i,i}$ and $q_{i,i}$ are divergences of stress tensor, electric displacement vector and heat flux vector respectively that are integrated over the volume Ω . Application of Divergence Theorem to these terms over the volume Ω and surface Π yields

$$\begin{aligned} - \int_{\Omega} \sigma_{ij} \delta u_{i,j} \, d\Omega + \int_{\Pi} \sigma_{ij} n_j \delta u_i \, d\Pi + \int_{\Omega} b_i \delta u_i \, d\Omega - \int_{\Omega} \rho \ddot{u}_i \delta u_i \, d\Omega - \int_{\Omega} D_i \delta V_{,i} \, d\Omega + \int_{\Pi} D_i n_i \delta V \, d\Pi \\ - \int_{\Omega} \varphi_e \delta V \, d\Omega - \int_{\Omega} q_i \delta T_{,i} \, d\Omega + \int_{\Pi} q_i n_i \delta T \, d\Pi + \int_{\Omega} T_{ref} \dot{S} \delta T \, d\Omega - \int_{\Omega} \varphi_t \delta T \, d\Omega = 0 \end{aligned} \quad (B.3)$$

Substituting the boundary condition equations [Eq. 3.4] inside surface integrals we get

$$\begin{aligned} - \int_{\Omega} \sigma_{ij} \delta u_{i,j} \, d\Omega + \int_{\Pi} \bar{t}_i \delta u_i \, d\Pi + \int_{\Omega} b_i \delta u_i \, d\Omega - \int_{\Omega} \rho \ddot{u}_i \delta u_i \, d\Omega - \int_{\Omega} D_i \delta V_{,i} \, d\Omega - \int_{\Pi} \bar{Q} \delta V \, d\Pi \\ - \int_{\Omega} \varphi_e \delta V \, d\Omega - \int_{\Omega} q_i \delta T_{,i} \, d\Omega + \int_{\Pi} \bar{q} \delta T \, d\Pi + \int_{\Pi} h_v (T - T_f) \delta T \, d\Pi + \int_{\Omega} T_{ref} \dot{S} \delta T \, d\Omega \\ - \int_{\Omega} \varphi_t \delta T \, d\Omega = 0 \end{aligned} \quad (B.4)$$

By reversing the tensor subscripts, we can write

$$\sigma_{ij} \delta u_{i,j} = \sigma_{ji} \delta u_{j,i} = \frac{1}{2} [\sigma_{ij} \delta u_{i,j} + \sigma_{ji} \delta u_{j,i}] \quad (B.5a)$$

Now, the stress tensor is symmetric i.e. $\sigma_{ij} = \sigma_{ji}$.

Therefore,

$$\sigma_{ij} \delta u_{i,j} = \frac{1}{2} [\sigma_{ij} \delta u_{i,j} + \sigma_{ij} \delta u_{j,i}] = \sigma_{ij} \frac{1}{2} [\delta u_{i,j} + \delta u_{j,i}] \quad (\text{B.5b})$$

The strain tensor is defined from the gradient of displacement vector field through the following relationship:

$$\epsilon_{ij} = \frac{1}{2} [u_{i,j} + u_{j,i}] \quad (\text{B.5c})$$

Virtual displacements would result in a 'virtual' strain tensor given by

$$\delta \epsilon_{ij} = \frac{1}{2} [\delta u_{i,j} + \delta u_{j,i}] \quad (\text{B.5d})$$

Using the above relations [B.5b and B.5d] we can write

$$\sigma_{ij} \delta u_{i,j} = \sigma_{ij} \delta \epsilon_{ij} \quad (\text{B.5e})$$

Electric field vector is defined from the gradient of electric potential (*a scalar*) field through the following relationship

$$E_i = -V_{,i} \quad (\text{B.5f})$$

For a virtual potential change δV , the 'virtual' electric field vector becomes

$$\delta E_i = -\delta V_{,i} \quad (\text{B.5g})$$

Heat flux vector is defined from the gradient of temperature (*a scalar*) field through the following relationship

$$q_i = -\kappa_{ij} T_{,i} \quad (\text{B.5h})$$

Replacing ($\sigma_{ij} \delta u_{i,j}$), $\delta V_{,i}$ and q_i in [Eq. B.4] we get

$$\begin{aligned} & - \int_{\Omega} \sigma_{ij} \delta \epsilon_{ij} d\Omega + \int_{\Pi} \bar{t} \delta u_i d\Pi + \int_{\Omega} b_i \delta u_i d\Omega - \int_{\Omega} \rho \ddot{u}_i \delta u_i d\Omega + \int_{\Omega} D_i \delta E_i d\Omega - \int_{\Pi} \bar{Q} \delta V d\Pi \\ & - \int_{\Omega} \varphi_e \delta V d\Omega + \int_{\Omega} \kappa_{ij} T_{,i} \delta T_{,i} d\Omega + \int_{\Pi} \bar{q} \delta T d\Pi + \int_{\Pi} h_v (T - T_f) \delta T d\Pi \\ & + \int_{\Omega} T_{ref} \dot{S} \delta T d\Omega - \int_{\Omega} \varphi_t \delta T d\Omega = 0 \end{aligned} \quad (\text{B.6})$$

Substituting for σ_{ij} , D_i and S using the Constitutive Relations [Eq. 3.2] we get

$$\begin{aligned} & - \int_{\Omega} \delta \epsilon_{ij} c_{ijkl} \epsilon_{kl} d\Omega + \int_{\Omega} \delta \epsilon_{ij} e_{ijk} E_k d\Omega + \int_{\Omega} \delta \epsilon_{ij} \lambda_{ij} T d\Omega + \int_{\Pi} \bar{t} \delta u_i d\Pi + \int_{\Omega} b_i \delta u_i d\Omega \\ & - \int_{\Omega} \rho \ddot{u}_i \delta u_i d\Omega + \int_{\Omega} \delta E_i e_{ikl} \epsilon_{kl} d\Omega + \int_{\Omega} \delta E_i \epsilon_{ik} E_k d\Omega + \int_{\Omega} \delta E_i p_i T d\Omega - \int_{\Pi} \bar{Q} \delta T d\Pi - \int_{\Omega} \varphi_e \delta V d\Omega \\ & + \int_{\Omega} \kappa_{ij} T_{,i} \delta T_{,i} d\Omega + \int_{\Pi} \bar{q} \delta T d\Pi + \int_{\Pi} h_v (T - T_f) \delta T d\Pi + \int_{\Omega} T_{ref} (\lambda_{kl} \dot{\epsilon}_{kl} + p \dot{E}_k + \alpha_v \dot{T}) \delta T d\Omega \\ & - \int_{\Omega} \varphi_t \delta T d\Omega = 0 \end{aligned} \quad (\text{B.7})$$

In matrix notation, this can be expressed more conveniently as

$$\begin{aligned}
& - \int_{\Omega} \{\delta \epsilon\}^T [c] \{\epsilon\} d\Omega + \int_{\Omega} \{\delta \epsilon\}^T [e]^T \{E\} d\Omega + \int_{\Omega} \{\delta \epsilon\}^T \{\lambda\} T d\Omega + \int_{\Pi} \{\delta u\}^T \{\bar{t}\} d\Pi + \int_{\Omega} \{\delta u\}^T \{b\} d\Omega \\
& - \int_{\Omega} \rho \{\delta u\}^T \{\ddot{u}\} d\Omega + \int_{\Omega} \{\delta E\}^T [e] \{\epsilon\} d\Omega + \int_{\Omega} \{\delta E\}^T [\varepsilon] \{E\} d\Omega + \int_{\Omega} \{\delta E\}^T \{p\} T d\Omega \\
& - \int_{\Pi} \bar{Q} \delta V d\Pi - \int_{\Omega} \varphi_e \delta V d\Omega + \int_{\Omega} \{\delta T_{,i}\}^T [\kappa] \{T_{,i}\} d\Omega + \int_{\Pi} \delta T \bar{q} d\Pi + \int_{\Pi} \delta T h_v T d\Pi \\
& - \int_{\Pi} \delta T h_v T_f d\Pi + \int_{\Omega} \delta T T_{ref} \{\lambda\}^T \{\dot{\epsilon}\} d\Omega + \int_{\Omega} \delta T T_{ref} \{p\}^T \{\dot{E}\} d\Omega \\
& + \int_{\Omega} \delta T T_{ref} \alpha_v \dot{T} d\Omega - \int_{\Omega} \delta T \varphi_t d\Omega = 0
\end{aligned} \tag{B.8}$$

FINITE ELEMENT FORMULATION FOR A GENERAL 3-D ELEMENT:

The displacement, electric potential and temperature at any point within a finite element can be interpolated in terms of its nodal displacements $\{\bar{u}\}$, nodal electric potentials $\{\bar{V}\}$ and nodal temperatures $\{\bar{T}\}$ respectively using *Shape-function matrices* as follows:

$$\{u\} = [N_u] \{\bar{u}\}; \quad V = [N_V] \{\bar{V}\}; \quad T = [N_T] \{\bar{T}\} \tag{B.10}$$

Similarly, the strain, electric field and temperature gradient vectors at any point within a finite element can be interpolated in terms of its nodal displacements, nodal electric potentials and nodal temperatures respectively using *B-matrices* as follows:

$$\{\epsilon\} = [B_u] \{\bar{u}\}; \quad \{E\} = -[B_V] \{\bar{V}\}; \quad \{T_{,i}\} = [B_T] \{\bar{T}\} \tag{B.11}$$

Substitution of these interpolations in the matrix equation [Eq. B.8] of the *Virtual Work Principle* yields

$$\begin{aligned}
& - \int_{\Omega} \{\delta \bar{u}\}^T [B_u]^T [c] [B_u] \{\bar{u}\} d\Omega - \int_{\Omega} \{\delta \bar{u}\}^T [B_u]^T [e]^T [B_V] \{\bar{V}\} d\Omega \\
& + \int_{\Omega} \{\delta \bar{u}\}^T [B_u]^T \{\lambda\} [N_T] \{\bar{T}\} d\Omega + \int_{\Pi} \{\delta \bar{u}\}^T [N_{us}]^T \{\bar{t}\} d\Pi
\end{aligned}$$

$$\begin{aligned}
& + \int_{\Omega} \{\delta \bar{u}\}^T [N_u]^T \{b\} d\Omega - \int_{\Omega} \{\delta \bar{u}\}^T [N_u]^T \rho [N_u] \{\ddot{u}\} d\Omega - \int_{\Omega} \{\delta \bar{V}\}^T [B_V]^T [e] [B_u] \{\bar{u}\} d\Omega \\
& + \int_{\Omega} \{\delta \bar{V}\}^T [B_V]^T [\varepsilon] [B_V] \{\bar{V}\} d\Omega - \int_{\Omega} \{\delta \bar{V}\}^T [B_V]^T \{p\} [N_T] \{\bar{T}\} d\Omega \\
& - \int_{\Pi} \{\delta \bar{V}\}^T [N_{Vs}]^T \bar{Q} d\Pi - \int_{\Omega} \{\delta \bar{V}\}^T [N_V]^T \varphi_e d\Omega + \int_{\Omega} \{\delta \bar{T}\}^T [B_T]^T \{\kappa\} [B_T] \{\bar{T}\} d\Omega \\
& + \int_{\Pi} \{\delta \bar{T}\}^T [N_{Ts}]^T \bar{q} d\Pi + \int_{\Pi} \{\delta \bar{T}\}^T [N_{Ts}]^T h_v [N_{Ts}] \{\bar{T}\} d\Pi \\
& - \int_{\Pi} \{\delta \bar{T}\}^T [N_{Ts}]^T h_v T_f d\Pi + \int_{\Omega} \{\delta T\}^T [N_T]^T T_{ref} \{\lambda\}^T [B_u] \{\dot{\bar{u}}\} d\Omega \\
& - \int_{\Omega} \{\delta \bar{T}\}^T [N_T]^T T_{ref} \{p\}^T [B_V] \{\dot{\bar{V}}\} d\Omega + \int_{\Omega} \{\delta \bar{T}\}^T [N_T]^T T_{ref} \alpha_v [N_T] \{\dot{\bar{T}}\} d\Omega \\
& - \int_{\Omega} \{\delta \bar{T}\}^T [N_T]^T \varphi_t d\Omega = 0
\end{aligned}$$

(B.12)

As the nodal values within an element are constant inside the integrals, the above equation can be simplified as

$$\begin{aligned}
& \{\delta \bar{u}\}^T \left[- \int_{\Omega} [B_u]^T [c] [B_u] \{\bar{u}\} d\Omega - \int_{\Omega} [B_u]^T [e]^T [B_V] \{\bar{V}\} d\Omega + \int_{\Omega} [B_u]^T \{\lambda\} [N_T] \{\bar{T}\} d\Omega + \right. \\
& \left. \int_{\Pi} [N_{us}]^T \{\bar{\varepsilon}\} d\Pi + \int_{\Omega} [N_u]^T \{b\} d\Omega - \int_{\Omega} [N_u]^T \rho [N_u] \{\ddot{u}\} d\Omega \right] \\
& + \{\delta \bar{V}\}^T \left[- \int_{\Omega} [B_V]^T [e] [B_u] \{\bar{u}\} d\Omega + \int_{\Omega} [B_V]^T [\varepsilon] [B_V] \{\bar{V}\} d\Omega - \right. \\
& \left. \int_{\Omega} [B_V]^T \{p\} [N_T] \{\bar{T}\} d\Omega - \int_{\Pi} [N_{Vs}]^T \bar{Q} d\Pi - \int_{\Omega} [N_V]^T \varphi_e d\Omega \right] \\
& + \{\delta \bar{T}\}^T \left[\int_{\Omega} [B_T]^T \{\kappa\} [B_T] \{\bar{T}\} d\Omega + \int_{\Pi} [N_{Ts}]^T \bar{q} d\Pi + \int_{\Pi} [N_{Ts}]^T h_v [N_{Ts}] \{\bar{T}\} d\Pi - \right. \\
& \left. \int_{\Pi} [N_{Ts}]^T h_v T_f d\Pi + \int_{\Omega} [N_T]^T T_{ref} \{\lambda\}^T [B_u] \{\dot{\bar{u}}\} d\Omega - \int_{\Omega} [N_T]^T T_{ref} \{p\}^T [B_V] \{\dot{\bar{V}}\} d\Omega + \right. \\
& \left. \int_{\Omega} [N_T]^T T_{ref} \alpha_v [N_T] \{\dot{\bar{T}}\} d\Omega - \int_{\Omega} [N_T]^T \varphi_t d\Omega \right] = 0
\end{aligned}$$

(B.13)

This equation would be true for all arbitrary values of nodal virtual displacements $\{\delta \bar{u}\}$, nodal virtual electric potential change $\{\delta \bar{V}\}$ and nodal temperature change $\{\delta \bar{T}\}$ if and only if the coefficients of these terms are simultaneously zero. This results in the following set of coupled finite element equations

$$\begin{aligned}
& \int_{\Omega} [B_u]^T [c] [B_u] \{\bar{u}\} d\Omega - \int_{\Omega} [B_u]^T [e]^T [B_V] \{\bar{V}\} d\Omega + \int_{\Omega} [B_u]^T \{\lambda\} [N_T] \{\bar{T}\} d\Omega + \\
& \int_{\Pi} [N_{us}]^T \{\bar{t}\} d\Pi + \int_{\Omega} [N_u]^T \{b\} d\Omega - \int_{\Omega} [N_u]^T \rho [N_u] \{\ddot{\bar{u}}\} d\Omega = 0 \\
& - \int_{\Omega} [B_V]^T [e] [B_u] \{\bar{u}\} d\Omega + \int_{\Omega} [B_V]^T [\varepsilon] [B_V] \{\bar{V}\} d\Omega - \int_{\Omega} [B_V]^T \{p\} [N_T] \{\bar{T}\} d\Omega - \\
& \int_{\Pi} [N_{Vs}]^T \bar{Q} d\Pi - \int_{\Omega} [N_V]^T \varphi_e d\Omega = 0 \\
& \int_{\Omega} [B_T]^T \{\kappa\} [B_T] \{\bar{T}\} d\Omega + \int_{\Pi} [N_{Ts}]^T \bar{q} d\Pi + \int_{\Pi} [N_{Ts}]^T h_v [N_{Ts}] \{\bar{T}\} d\Pi - \\
& \int_{\Pi} [N_{Ts}]^T h_v T_f d\Pi + \int_{\Omega} [N_T]^T T_{ref} \{\lambda\}^T [B_u] \{\ddot{\bar{u}}\} d\Omega - \int_{\Omega} [N_T]^T T_{ref} \{p\}^T [B_V] \{\dot{\bar{V}}\} d\Omega + \\
& \int_{\Omega} [N_T]^T T_{ref} \alpha_v [N_T] \{\dot{\bar{T}}\} d\Omega - \int_{\Omega} [N_T]^T \varphi_t d\Omega = 0
\end{aligned} \tag{B.14}$$

This set of equations can be written more conveniently in a matrix form as

$$\begin{aligned}
& \begin{bmatrix} \int_{\Omega} [N_u]^T \rho [N_u] d\Omega & 0 & 0 \\ 0 & 0 & 0 \\ 0 & 0 & 0 \end{bmatrix} \begin{Bmatrix} \ddot{\bar{u}} \\ \dot{\bar{V}} \\ \dot{\bar{T}} \end{Bmatrix} \\
& + \begin{bmatrix} 0 & 0 & 0 \\ 0 & 0 & 0 \\ \int_{\Omega} [N_T]^T T_{ref} \{\lambda\}^T [B_u] d\Omega & - \int_{\Omega} [N_T]^T T_{ref} \{p\}^T [B_V] d\Omega & \int_{\Omega} [N_T]^T T_{ref} \alpha_v [N_T] d\Omega \end{bmatrix} \begin{Bmatrix} \dot{\bar{u}} \\ \dot{\bar{V}} \\ \dot{\bar{T}} \end{Bmatrix} \\
& + \begin{bmatrix} \int_{\Omega} [B_u]^T [c] [B_u] d\Omega & \int_{\Omega} [B_u]^T [e]^T [B_V] d\Omega & - \int_{\Omega} [B_u]^T \{\lambda\} [N_T] d\Omega \\ \int_{\Omega} [B_V]^T [e] [B_u] d\Omega & - \int_{\Omega} [B_V]^T [\varepsilon] [B_V] d\Omega & \int_{\Omega} [B_V]^T \{p\} [N_T] d\Omega \\ 0 & 0 & \int_{\Omega} [B_T]^T \{\kappa\} [B_T] d\Omega + \int_{\Pi} [N_{Ts}]^T h_v [N_{Ts}] d\Pi \end{bmatrix} \begin{Bmatrix} \bar{u} \\ \bar{V} \\ \bar{T} \end{Bmatrix} \\
& = \begin{Bmatrix} \int_{\Pi} [N_{us}]^T \{\bar{t}\} d\Pi + \int_{\Omega} [N_u]^T \{b\} d\Omega \\ - \int_{\Pi} [N_{Vs}]^T \bar{Q} d\Pi - \int_{\Omega} [N_V]^T \varphi_e d\Omega \\ \int_{\Pi} [N_{Ts}]^T h_v T_f d\Pi - \int_{\Pi} [N_{Ts}]^T \bar{q} d\Pi + \int_{\Omega} [N_T]^T \varphi_t d\Omega \end{Bmatrix} \tag{B.15}
\end{aligned}$$

This equation is similar to a typical equation of dynamics written as

$$\begin{bmatrix} M_{uu} & 0 & 0 \\ 0 & 0 & 0 \\ 0 & 0 & 0 \end{bmatrix} \begin{Bmatrix} \ddot{\bar{u}} \\ \dot{\bar{V}} \\ \dot{\bar{T}} \end{Bmatrix} + \begin{bmatrix} 0 & 0 & 0 \\ 0 & 0 & 0 \\ C_{Tu} & C_{TV} & C_{TT} \end{bmatrix} \begin{Bmatrix} \dot{\bar{u}} \\ \dot{\bar{V}} \\ \dot{\bar{T}} \end{Bmatrix} + \begin{bmatrix} K_{uu} & K_{uV} & K_{uT} \\ K_{Vu} & K_{VV} & K_{VT} \\ 0 & 0 & K_{TT} \end{bmatrix} \begin{Bmatrix} \bar{u} \\ \bar{V} \\ \bar{T} \end{Bmatrix} = \begin{Bmatrix} F_u \\ F_V \\ F_T \end{Bmatrix} \tag{B.16}$$

Where

$$M_{uu} = \int_{\Omega} [N_u]^T \rho [N_u] d\Omega$$

$$K_{uu} = \int_{\Omega} [B_u]^T [c] [B_u] d\Omega$$

$$K_{VV} = - \int_{\Omega} [B_V]^T [\varepsilon] [B_V] d\Omega$$

$$K_{uV} = K_{Vu}^T = \int_{\Omega} [B_u]^T [e]^T [B_V] d\Omega$$

$$K_{uT} = - \int_{\Omega} [B_u]^T \{\lambda\} [N_T] d\Omega$$

$$K_{VT} = \int_{\Omega} [B_V]^T \{p\} [N_T] d\Omega$$

$$K_{TT} = \int_{\Omega} [B_T]^T \{\kappa\} [B_T] d\Omega + \int_{\Pi} [N_{Ts}]^T h_v [N_{Ts}] d\Pi$$

$$C_{Tu} = T_{ref} \int_{\Omega} [N_T]^T \{\lambda\}^T [B_u] d\Omega = -T_{ref} K_{uT}^T$$

$$C_{TV} = -T_{ref} \int_{\Omega} [N_T]^T \{p\}^T [B_V] d\Omega = -T_{ref} K_{VT}^T$$

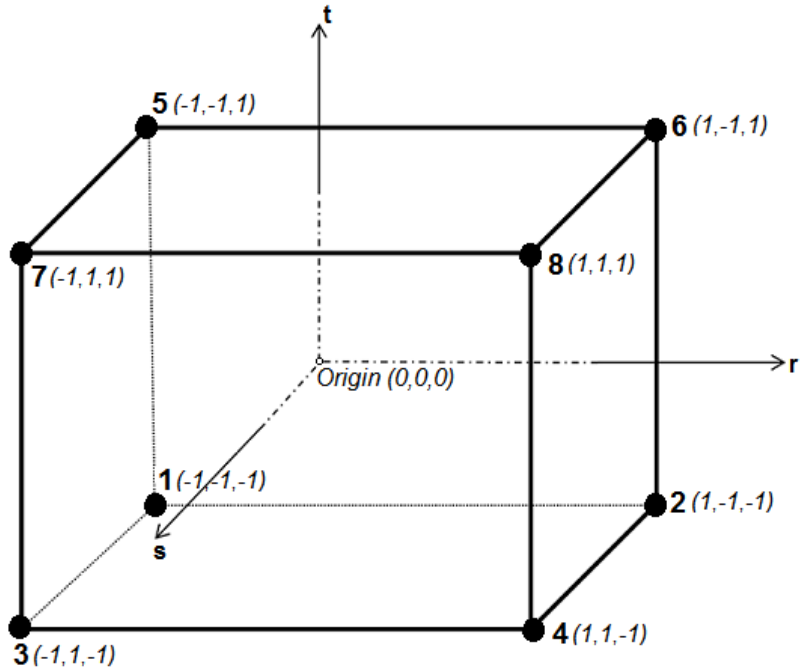
$$C_{TT} = T_{ref} \int_{\Omega} [N_T]^T \alpha_v [N_T] d\Omega = \rho C_v \int_{\Omega} [N_T]^T [N_T] d\Omega$$

$$F_u = \int_{\Pi} [N_{us}]^T \{\bar{\varepsilon}\} d\Pi + \int_{\Omega} [N_u]^T \{b\} d\Omega$$

$$F_V = - \int_{\Pi} [N_{Vs}]^T \bar{Q} d\Pi - \int_{\Omega} [N_V]^T \varphi_e d\Omega$$

$$F_T = \int_{\Pi} [N_{Ts}]^T h_v T_f d\Pi - \int_{\Pi} [N_{Ts}]^T \bar{q} d\Pi + \int_{\Omega} [N_T]^T \varphi_t d\Omega$$

3-DIMENSIONAL, 8-NODE HEXAHEDRON, ISOPARAMETRIC ELEMENT



Order: (r,s,t)

The *Shape Functions* of a 3-D 8-node hexahedron element (shown in the Fig. above) are defined in the analysis plane as follows:

$$\begin{aligned}
 N_1 &= \frac{1}{8}(1-r)(1-s)(1-t) & N_5 &= \frac{1}{8}(1-r)(1-s)(1+t) \\
 N_2 &= \frac{1}{8}(1+r)(1-s)(1-t) & N_6 &= \frac{1}{8}(1+r)(1-s)(1+t) \\
 N_3 &= \frac{1}{8}(1-r)(1+s)(1-t) & N_7 &= \frac{1}{8}(1-r)(1+s)(1+t) \\
 N_4 &= \frac{1}{8}(1+r)(1+s)(1-t) & N_8 &= \frac{1}{8}(1+r)(1+s)(1+t)
 \end{aligned}$$

For a corresponding 8-node element in the physical plane ($x,y,z \equiv r,s,t$), the position of any point within the element can be approximated in terms of its nodal positions using the *Shape Functions* defined in the analysis plane as follows:

$$x = [N_1 \quad N_2 \quad N_3 \quad \dots \quad N_8] \begin{Bmatrix} x_1 \\ x_2 \\ x_3 \\ \dots \\ x_8 \end{Bmatrix} \quad y = [N_1 \quad N_2 \quad N_3 \quad \dots \quad N_8] \begin{Bmatrix} y_1 \\ y_2 \\ y_3 \\ \dots \\ y_8 \end{Bmatrix}$$

$$z = [N_1 \quad N_2 \quad N_3 \quad \dots \quad N_8] \begin{Bmatrix} z_1 \\ z_2 \\ z_3 \\ \dots \\ z_8 \end{Bmatrix} \quad (\text{B.17})$$

In the physical plane, the element has 5 degrees of freedom per node (*3 displacements u, v and w + 1 electric potential V + 1 temperature T*) and a total of 40 degrees of freedom. As this is an 'isoparametric' element, the same *Shape Functions* can also be used to approximate the independent variables at a general point within the element in terms of their nodal values. This gives

$$u = [N_1 \quad N_2 \quad N_3 \quad \dots \quad N_8] \begin{Bmatrix} u_1 \\ u_2 \\ u_3 \\ \dots \\ u_8 \end{Bmatrix} \quad v = [N_1 \quad N_2 \quad N_3 \quad \dots \quad N_8] \begin{Bmatrix} v_1 \\ v_2 \\ v_3 \\ \dots \\ v_8 \end{Bmatrix}$$

$$w = [N_1 \quad N_2 \quad N_3 \quad \dots \quad N_8] \begin{Bmatrix} w_1 \\ w_2 \\ w_3 \\ \dots \\ w_8 \end{Bmatrix} \quad V = [N_1 \quad N_2 \quad N_3 \quad \dots \quad N_8] \begin{Bmatrix} V_1 \\ V_2 \\ V_3 \\ \dots \\ V_8 \end{Bmatrix}$$

$$T = [N_1 \quad N_2 \quad N_3 \quad \dots \quad N_8] \begin{Bmatrix} T_1 \\ T_2 \\ T_3 \\ \dots \\ T_8 \end{Bmatrix} \quad (\text{B.18})$$

Using these relations, the *Shape-function matrices* in 3-D can be written as

$$N_u = \begin{bmatrix} N_1 & 0 & 0 & N_2 & 0 & 0 & \dots & N_8 & 0 & 0 \\ 0 & N_1 & 0 & 0 & N_2 & 0 & \dots & 0 & N_8 & 0 \\ 0 & 0 & N_1 & 0 & 0 & N_2 & \dots & 0 & 0 & N_8 \end{bmatrix}_{3 \times 24} \quad (\text{B.19a})$$

$$N_V = [N_1 \quad N_2 \quad N_3 \quad \dots \quad N_8]_{1 \times 8} \quad (\text{B.19b})$$

$$N_T = [N_1 \quad N_2 \quad N_3 \quad \dots \quad N_8]_{1 \times 8} \quad (\text{B.19c})$$

The strain (ϵ), electric field (E) and temperature gradient (T_i) in 3-D are defined as

$$\epsilon = \begin{Bmatrix} \epsilon_{xx} \\ \epsilon_{yy} \\ \epsilon_{zz} \\ \gamma_{xy} \\ \gamma_{yz} \\ \gamma_{zx} \end{Bmatrix} = \begin{Bmatrix} \frac{\partial u}{\partial x} \\ \frac{\partial v}{\partial y} \\ \frac{\partial w}{\partial z} \\ \frac{\partial v}{\partial x} + \frac{\partial u}{\partial y} \\ \frac{\partial w}{\partial y} + \frac{\partial v}{\partial z} \\ \frac{\partial u}{\partial z} + \frac{\partial w}{\partial x} \end{Bmatrix} = \begin{bmatrix} 1 & 0 & 0 & 0 & 0 & 0 & 0 & 0 & 0 \\ 0 & 0 & 0 & 0 & 1 & 0 & 0 & 0 & 0 \\ 0 & 0 & 0 & 0 & 0 & 0 & 0 & 0 & 1 \\ 0 & 1 & 0 & 1 & 0 & 0 & 0 & 0 & 0 \\ 0 & 0 & 0 & 0 & 0 & 1 & 0 & 1 & 0 \\ 0 & 0 & 1 & 0 & 0 & 0 & 1 & 0 & 0 \end{bmatrix} \begin{Bmatrix} \frac{\partial u}{\partial x} \\ \frac{\partial u}{\partial y} \\ \frac{\partial u}{\partial z} \\ \frac{\partial v}{\partial x} \\ \frac{\partial v}{\partial y} \\ \frac{\partial v}{\partial z} \\ \frac{\partial w}{\partial x} \\ \frac{\partial w}{\partial y} \\ \frac{\partial w}{\partial z} \end{Bmatrix} = [H_u] \begin{Bmatrix} \frac{\partial u}{\partial x} \\ \frac{\partial u}{\partial y} \\ \frac{\partial u}{\partial z} \\ \frac{\partial v}{\partial x} \\ \frac{\partial v}{\partial y} \\ \frac{\partial v}{\partial z} \\ \frac{\partial w}{\partial x} \\ \frac{\partial w}{\partial y} \\ \frac{\partial w}{\partial z} \end{Bmatrix} \quad (\text{B.20a})$$

$$E = \begin{Bmatrix} E_x \\ E_y \\ E_z \end{Bmatrix} = - \begin{Bmatrix} \frac{\partial V}{\partial x} \\ \frac{\partial V}{\partial y} \\ \frac{\partial V}{\partial z} \end{Bmatrix} \quad (\text{B.20b})$$

$$T_i = \begin{Bmatrix} T_{,x} \\ T_{,y} \\ T_{,z} \end{Bmatrix} = \begin{Bmatrix} \frac{\partial T}{\partial x} \\ \frac{\partial T}{\partial y} \\ \frac{\partial T}{\partial z} \end{Bmatrix} \quad (\text{B.20c})$$

We see that the strain, electric field and temperature gradient are defined in terms of derivatives of u, v, w, V and T with respect to x, y and z [Eq. B.20]. However, for the isoparametric element considered in the current analysis, u, v, w, V and T are defined in terms of r, s and t using the *Shape Functions* [Eq. B.18]. Therefore, in order to evaluate the above relations, we first need to relate the derivatives with respect to x, y and z to those with respect to r, s and t . This is done through the following Jacobian relations:

$$\begin{aligned} \frac{\partial}{\partial r} &= \frac{\partial}{\partial x} \frac{\partial x}{\partial r} + \frac{\partial}{\partial y} \frac{\partial y}{\partial r} + \frac{\partial}{\partial z} \frac{\partial z}{\partial r} \\ \frac{\partial}{\partial s} &= \frac{\partial}{\partial x} \frac{\partial x}{\partial s} + \frac{\partial}{\partial y} \frac{\partial y}{\partial s} + \frac{\partial}{\partial z} \frac{\partial z}{\partial s} \\ \frac{\partial}{\partial t} &= \frac{\partial}{\partial x} \frac{\partial x}{\partial t} + \frac{\partial}{\partial y} \frac{\partial y}{\partial t} + \frac{\partial}{\partial z} \frac{\partial z}{\partial t} \end{aligned} \quad \text{or} \quad \begin{Bmatrix} \frac{\partial}{\partial r} \\ \frac{\partial}{\partial s} \\ \frac{\partial}{\partial t} \end{Bmatrix} = \begin{bmatrix} \frac{\partial x}{\partial r} & \frac{\partial y}{\partial r} & \frac{\partial z}{\partial r} \\ \frac{\partial x}{\partial s} & \frac{\partial y}{\partial s} & \frac{\partial z}{\partial s} \\ \frac{\partial x}{\partial t} & \frac{\partial y}{\partial t} & \frac{\partial z}{\partial t} \end{bmatrix} \begin{Bmatrix} \frac{\partial}{\partial x} \\ \frac{\partial}{\partial y} \\ \frac{\partial}{\partial z} \end{Bmatrix} = [J] \begin{Bmatrix} \frac{\partial}{\partial x} \\ \frac{\partial}{\partial y} \\ \frac{\partial}{\partial z} \end{Bmatrix}$$

This gives

$$\begin{Bmatrix} \frac{\partial}{\partial x} \\ \frac{\partial}{\partial y} \\ \frac{\partial}{\partial z} \end{Bmatrix} = [J]^{-1} \begin{Bmatrix} \frac{\partial}{\partial r} \\ \frac{\partial}{\partial s} \\ \frac{\partial}{\partial t} \end{Bmatrix} = [\Gamma] \begin{Bmatrix} \frac{\partial}{\partial r} \\ \frac{\partial}{\partial s} \\ \frac{\partial}{\partial t} \end{Bmatrix} \quad (\text{B.21})$$

The Jacobian matrix $[J]$ or the Inverse Jacobian matrix $[\Gamma]$ can be easily evaluated for an element using the position approximation [Eq. B.17]. Using the Inverse Jacobian matrix $[\Gamma]$, the spatial derivatives of u, v and w in the physical and analysis planes can be related as

$$\begin{Bmatrix} \frac{\partial u}{\partial x} \\ \frac{\partial u}{\partial y} \\ \frac{\partial u}{\partial z} \\ \frac{\partial v}{\partial x} \\ \frac{\partial v}{\partial y} \\ \frac{\partial v}{\partial z} \\ \frac{\partial w}{\partial x} \\ \frac{\partial w}{\partial y} \\ \frac{\partial w}{\partial z} \end{Bmatrix} = \begin{bmatrix} [\Gamma] & [0] & [0] \\ [0] & [\Gamma] & [0] \\ [0] & [0] & [\Gamma] \end{bmatrix} \begin{Bmatrix} \frac{\partial u}{\partial r} \\ \frac{\partial u}{\partial s} \\ \frac{\partial u}{\partial t} \\ \frac{\partial v}{\partial r} \\ \frac{\partial v}{\partial s} \\ \frac{\partial v}{\partial t} \\ \frac{\partial w}{\partial r} \\ \frac{\partial w}{\partial s} \\ \frac{\partial w}{\partial t} \end{Bmatrix} = [\Gamma_u] \begin{Bmatrix} \frac{\partial u}{\partial r} \\ \frac{\partial u}{\partial s} \\ \frac{\partial u}{\partial t} \\ \frac{\partial v}{\partial r} \\ \frac{\partial v}{\partial s} \\ \frac{\partial v}{\partial t} \\ \frac{\partial w}{\partial r} \\ \frac{\partial w}{\partial s} \\ \frac{\partial w}{\partial t} \end{Bmatrix} \quad (\text{B.22})$$

Applying the approximation for displacements [Eq. B.18] we get

$$\begin{Bmatrix} \frac{\partial u}{\partial r} \\ \frac{\partial u}{\partial s} \\ \frac{\partial u}{\partial t} \\ \frac{\partial v}{\partial r} \\ \frac{\partial v}{\partial s} \\ \frac{\partial v}{\partial t} \\ \frac{\partial w}{\partial r} \\ \frac{\partial w}{\partial s} \\ \frac{\partial w}{\partial t} \end{Bmatrix} = \begin{bmatrix} \frac{\partial N_1}{\partial r} & 0 & 0 & \frac{\partial N_2}{\partial r} & 0 & 0 & \dots & \frac{\partial N_8}{\partial r} & 0 & 0 \\ \frac{\partial N_1}{\partial s} & 0 & 0 & \frac{\partial N_2}{\partial s} & 0 & 0 & \dots & \frac{\partial N_8}{\partial s} & 0 & 0 \\ \frac{\partial N_1}{\partial t} & 0 & 0 & \frac{\partial N_2}{\partial t} & 0 & 0 & \dots & \frac{\partial N_8}{\partial t} & 0 & 0 \\ 0 & \frac{\partial N_1}{\partial r} & 0 & 0 & \frac{\partial N_2}{\partial r} & 0 & \dots & 0 & \frac{\partial N_8}{\partial r} & 0 \\ 0 & \frac{\partial N_1}{\partial s} & 0 & 0 & \frac{\partial N_2}{\partial s} & 0 & \dots & 0 & \frac{\partial N_8}{\partial s} & 0 \\ 0 & \frac{\partial N_1}{\partial t} & 0 & 0 & \frac{\partial N_2}{\partial t} & 0 & \dots & 0 & \frac{\partial N_8}{\partial t} & 0 \\ 0 & 0 & \frac{\partial N_1}{\partial r} & 0 & 0 & \frac{\partial N_2}{\partial r} & \dots & 0 & 0 & \frac{\partial N_8}{\partial r} \\ 0 & 0 & \frac{\partial N_1}{\partial s} & 0 & 0 & \frac{\partial N_2}{\partial s} & \dots & 0 & 0 & \frac{\partial N_8}{\partial s} \\ 0 & 0 & \frac{\partial N_1}{\partial t} & 0 & 0 & \frac{\partial N_2}{\partial t} & \dots & 0 & 0 & \frac{\partial N_8}{\partial t} \end{bmatrix} \begin{Bmatrix} u_1 \\ v_1 \\ w_1 \\ u_2 \\ v_2 \\ w_2 \\ \dots \\ u_8 \\ v_8 \\ w_8 \end{Bmatrix} = [\Lambda_u] \begin{Bmatrix} u_1 \\ v_1 \\ w_1 \\ u_2 \\ v_2 \\ w_2 \\ \dots \\ u_8 \\ v_8 \\ w_8 \end{Bmatrix} \quad (\text{B.23})$$

The definitions of strain [Eq. B.20a, B.22, and B.23] and mechanical *B-matrix* [Eq. B.11] give

$$\epsilon = [H_u] [\Gamma_u] [\Lambda_u] \begin{Bmatrix} u_1 \\ v_1 \\ w_1 \\ u_2 \\ v_2 \\ w_2 \\ \dots \\ u_8 \\ v_8 \\ w_8 \end{Bmatrix} = [B_u] \begin{Bmatrix} u_1 \\ v_1 \\ w_1 \\ u_2 \\ v_2 \\ w_2 \\ \dots \\ u_8 \\ v_8 \\ w_8 \end{Bmatrix} \quad (\text{B.24a})$$

Therefore, the mechanical *B-matrix* is given by

$$[B_u] = [H_u] [\Gamma_u] [\Lambda_u] \quad (\text{B.24b})$$

The electrical and thermal B -matrices can be obtained using a similar procedure to give

$$E = \begin{Bmatrix} E_x \\ E_y \\ E_z \end{Bmatrix} = - \begin{Bmatrix} \frac{\partial V}{\partial x} \\ \frac{\partial V}{\partial y} \\ \frac{\partial V}{\partial z} \end{Bmatrix} = -[\Gamma] \begin{Bmatrix} \frac{\partial V}{\partial r} \\ \frac{\partial V}{\partial s} \\ \frac{\partial V}{\partial t} \end{Bmatrix} = -[\Gamma] \begin{bmatrix} \frac{\partial N_1}{\partial r} & \frac{\partial N_2}{\partial r} & \dots & \frac{\partial N_8}{\partial r} \\ \frac{\partial N_1}{\partial s} & \frac{\partial N_2}{\partial s} & \dots & \frac{\partial N_8}{\partial s} \\ \frac{\partial N_1}{\partial t} & \frac{\partial N_2}{\partial t} & \dots & \frac{\partial N_8}{\partial t} \end{bmatrix} \begin{Bmatrix} V_1 \\ V_2 \\ V_3 \\ \dots \\ V_8 \end{Bmatrix} = -[\Gamma][\Lambda_V] \begin{Bmatrix} V_1 \\ V_2 \\ V_3 \\ \dots \\ V_8 \end{Bmatrix} = -[B_V] \begin{Bmatrix} V_1 \\ V_2 \\ V_3 \\ \dots \\ V_8 \end{Bmatrix} \quad (\text{B.25a})$$

$$[B_V] = [\Gamma] [\Lambda_V] \quad (\text{B.25b})$$

$$T_{,i} = \begin{Bmatrix} T_{,x} \\ T_{,y} \\ T_{,z} \end{Bmatrix} = \begin{Bmatrix} \frac{\partial T}{\partial x} \\ \frac{\partial T}{\partial y} \\ \frac{\partial T}{\partial z} \end{Bmatrix} = [\Gamma] \begin{Bmatrix} \frac{\partial T}{\partial r} \\ \frac{\partial T}{\partial s} \\ \frac{\partial T}{\partial t} \end{Bmatrix} = [\Gamma] \begin{bmatrix} \frac{\partial N_1}{\partial r} & \frac{\partial N_2}{\partial r} & \dots & \frac{\partial N_8}{\partial r} \\ \frac{\partial N_1}{\partial s} & \frac{\partial N_2}{\partial s} & \dots & \frac{\partial N_8}{\partial s} \\ \frac{\partial N_1}{\partial t} & \frac{\partial N_2}{\partial t} & \dots & \frac{\partial N_8}{\partial t} \end{bmatrix} \begin{Bmatrix} T_1 \\ T_2 \\ T_3 \\ \dots \\ T_8 \end{Bmatrix} = [\Gamma][\Lambda_T] \begin{Bmatrix} T_1 \\ T_2 \\ T_3 \\ \dots \\ T_8 \end{Bmatrix} = [B_T] \begin{Bmatrix} T_1 \\ T_2 \\ T_3 \\ \dots \\ T_8 \end{Bmatrix} \quad (\text{B.26a})$$

$$[B_T] = [\Gamma][\Lambda_T] \quad (\text{B.26b})$$

Note: In this problem, $[B_V] = [B_T]$